

# Bend-Twist Coupled Carbon-Fiber Laminate Beams: Fundamental Behavior and Applications

Pavel Babuska

A thesis  
submitted in partial fulfillment of:  
requirements for the degree of

Master of Science in Civil Engineering

University of Washington

2017

Committee:

Richard Wiebe, Ph.D

Michael Motley, Ph.D

Laura Lowes, Ph.D

Program Authorized to Offer Degree:  
Civil and Environmental Engineering

©Copyright 2017  
Pavel Babuska

University of Washington

**Abstract**

Bend-Twist Coupled Carbon-Fiber Laminate Beams: Fundamental Behavior and  
Applications

Pavel Babuska

Chair of the Supervisory Committee:

Assistant Professor Richard Wiebe

Civil and Environmental Engineering

Material-induced bend-twist coupling in laminated composite beams has seen applications in engineered structures for decades, ranging from airplane wings to turbine blades. Symmetric, unbalanced, carbon fiber laminates which exhibit bend-twist coupling can be difficult to characterize and exhibit unintuitive deformation states which may pose challenges to the engineer. In this thesis, bend-twist coupled beams are investigated comprehensively, by experimentation, numerical modeling, and analytical methods. Beams of varying fiber angle and amount of coupling were manufactured and physically tested in both linear and nonlinear static and dynamic settings. Analytical mass and stiffness matrices were derived for the development of a beam element to use in the stiffness matrix analysis method. Additionally, an ABAQUS finite element model was used in conjunction with the analytical methods to predict and further characterize the behavior of the beams. The three regimes, experimental, analytical, and numerical, represent a full-field characterization of bend-twist coupling in composite beams.

A notable application of bend-twist coupled composites is for passively adaptive turbine blades whereby the deformation coupling can be built into the blade structure to simultane-

ously bend and twist, thus pitching the blade into or away from the fluid flow, changing the blade angle of attack. Passive pitch adaptation has been implemented successfully in wind turbine blades, however, for marine turbine blades, the technology is still in the development phase. Bend-twist coupling has been shown numerically to be beneficial to the tidal turbine performance, however little validation has been conducted in the experimental regime. In this thesis, passively adaptive experiment scale tidal turbine blades were designed, analyzed, manufactured, and physically tested, validating the foundational numerical work. It was shown that blade forces and root moments as well as turbine thrust and power coefficients can be manipulated by inclusion of passive pitch adaptation by bend-twist coupling.

**Keywords:** carbon fiber, composite, bend-twist coupling, composite turbine blades, stiffness matrix

# Acknowledgments

I would like to express my gratitude to the many individuals who have contributed to my successful completion of this thesis. First and foremost, I must thank my graduate advisor and committee chair, Dr. Richard Wiebe, for his unwavering support and encouragement throughout the entirety of my education at The University of Washington. Thank you for the constant stream of curious discussion, always-available help, and expert understanding of all things elasticity and mechanics. I am certain that I would not be the engineer I am today without your guidance.

I would like to thank Dr. Michael Motley for providing me with the opportunity that changed the course of my master's degree experience for the better, the offer to contribute to the tidal turbine blade research. Not only did you take a chance on hiring me, but you made me feel comfortable and welcome throughout. Your "where the rubber meets the road" approach to research always kept me grounded and moving in the right direction.

I would like to thank Dr. Ramona Barber for all her effort in collaboration on the marine turbine work, as well as constant friendship and mentorship throughout our time together. My gratitude would not be complete without the mention of our sailing excursion and my learning from you and your crew.

I would like to thank my colleague, office-mate, and friend, Tyler van Iderstein for the countless questions he entertained, solutions he provided, thought experiments he engaged in, and his shared excitement for all things space and science. In software engineering, "rubber

ducking” refers to a process by which the engineer would solve problems or debug his code by explaining it line-by-line to a rubber duck to aid in his own understanding. Tyler, you were the rubber duck to this work and I thank you for it.

My gratitude cannot be complete without mention of my family, who have stood by me in complete support of my decisions in selfless fashion. I dedicate this work to my mother, father, and brother, who are truly the hallmark of encouragement, and provided me with an incredible foundation on which to allow myself to grow and develop personally and professionally. I am forever grateful. Finally, thank you to all my friends, colleagues, and coffees (thanks Reboot Cafe!) who have supported me throughout this journey.

# Contents

- 1 Introduction** **1**
- 1.1 Motivation . . . . . 1
- 1.2 Background . . . . . 3
- 1.3 Outline . . . . . 6
  
- 2 Fundamental Mechanics of Bend-Twist Coupled Beams** **9**
- 2.1 Overview . . . . . 9
- 2.2 Beam Specimen Manufacture . . . . . 9
- 2.3 Experimental Methods . . . . . 13
- 2.3.1 Quasi-Static Force-Deflection . . . . . 14
- 2.3.2 Free Vibration . . . . . 16
- 2.3.3 Small Amplitude Frequency Sweep . . . . . 18
- 2.3.4 Large Amplitude Frequency Sweep . . . . . 20
- 2.4 ABAQUS Finite Element Modeling . . . . . 20
- 2.4.1 Structure Properties . . . . . 20
- 2.4.2 Model Steps . . . . . 21
- 2.4.3 Element Details . . . . . 23
- 2.5 Analytical Formulations . . . . . 24
- 2.5.1 Stiffness Matrix Method . . . . . 24

2.5.2	Exact Solution to Coupled Equations of Motion . . . . .	47
<b>3</b>	<b>Material Property Testing</b>	<b>53</b>
3.1	Overview . . . . .	53
3.2	Tension Testing . . . . .	54
3.3	3-Point Bending . . . . .	56
3.4	Cantilever Bending . . . . .	57
3.5	Steel Beam Modulus Testing . . . . .	59
3.6	Results and Discussion . . . . .	60
<b>4</b>	<b>Comparison of Results</b>	<b>63</b>
4.1	Static Force-Deflection . . . . .	63
4.2	Linear Vibration . . . . .	65
4.3	Large Amplitude Vibration . . . . .	69
4.4	Discussion of Results . . . . .	71
<b>5</b>	<b>Applications of Bend-Twist Coupled Composites</b>	<b>73</b>
5.1	General Applications . . . . .	73
5.1.1	Aircraft Wings . . . . .	73
5.1.2	Wind Turbine Blades . . . . .	74
5.1.3	Marine/Tidal Turbine Blades . . . . .	75
5.2	Bend-Twist Coupling for Passively Adaptive Tidal Turbine Blades . . . . .	76
5.2.1	Motivation . . . . .	76
5.2.2	Design of Flume-Scale Turbine Blades . . . . .	77
5.2.3	Analysis of Composite Spars . . . . .	79
5.2.4	Manufacture of Experimental Blades . . . . .	81
5.2.5	Load-Deflection Experiment and Structural Qualification . . . . .	82



5.2.6	Flume Experiment Results . . . . .	87
<b>6</b>	<b>Conclusions and Future work</b>	<b>93</b>
6.1	Conclusions . . . . .	93
6.1.1	Fundamentals . . . . .	93
6.1.2	Material Testing . . . . .	94
6.1.3	Comparison of Results . . . . .	95
6.1.4	Applications of Bend-Twist Coupled Composites . . . . .	96
6.2	Future Work . . . . .	98
6.2.1	Material Characterization . . . . .	98
6.2.2	Co-rotational Adaptation of Stiffness Matrix Method Model . . . . .	98
6.2.3	Larger Scale Experimentation of Passively Adaptive Marine Turbine Blades . . . . .	98
<b>A</b>	<b>Supplementary Information</b>	<b>104</b>
A.1	Hexcel IM7/8552 Curing Details . . . . .	104
A.1.1	Cure Profile . . . . .	104
A.1.2	Autoclave Bagging Process . . . . .	106
A.2	Model Scripts . . . . .	107
A.2.1	ABD Matrix Script . . . . .	107
A.2.2	Stiffness Matrix Method Model Scripts . . . . .	109

# List of Figures

1.1	Schematic of an off-angle unidirectional laminate with fiber angle, $\alpha$ . . . . .	4
1.2	NASA photograph of the Grumman X-29 in banked flight . . . . .	4
2.1	Cured laminate and cut template . . . . .	10
2.2	Through-thickness strain and stress distributions of laminate in bending . . .	13
2.3	Schematic showing laser sensor measurement at each edge and the relation to beam twist . . . . .	15
2.4	Deflection of varied fiber angle (10°, 20°, 30°) beams under identical loading .	15
2.5	Experimental setup for free vibration . . . . .	17
2.6	Free vibration ringdown for beams of varying fiber angles showing decreasing frequency of vibration for increasing fiber angle. Y-axis values are distance from laser sensor to beam in millimeters. . . . .	17
2.7	Experimental setup for frequency sweep . . . . .	18
2.8	Time domain response of 1G frequency sweep on beams of varying fiber angles. Y-axis values are distance from laser sensor to beam in millimeters . . . . .	19
2.9	Frequency domain response of 1G frequency sweep on beams of varying fiber angles. Y-axis values are power. . . . .	19
2.10	Fiber angle offset and coordinate system for unidirectional laminate . . . . .	25
2.11	Beam end constraints as a single point in finite element model . . . . .	38
2.12	$K_1$ , translational stiffness for an imposed transverse nodal displacement . . .	39

2.13	$K_2$ , translational stiffness for an imposed nodal rotation . . . . .	39
2.14	$K_4$ , rotational stiffness for an imposed nodal rotation . . . . .	40
2.15	$\frac{GJ}{L}$ , torsional stiffness for an imposed nodal twist . . . . .	40
2.16	$\frac{K}{L}$ , rotational stiffness for an imposed nodal twist . . . . .	41
2.17	Sensitivity of laminate fiber angle to the difference between coupled and uncoupled stiffness matrix terms . . . . .	42
3.1	8-ply and 16-ply autoclave plate specimen templates. Note that the specimens are labeled ‘1’-‘5’ from left to right. . . . .	54
3.2	Tension test material characterization results . . . . .	55
3.3	3-point bending experimental setup . . . . .	56
3.4	3-point bending test material characterization results . . . . .	57
3.5	Cantilever bending test material characterization results . . . . .	58
4.1	Comparison of analytical, FEM, and experimental results for load-deformation characterization. Solid lines represent the ABAQUS numerical simulations, while dashed lines illustrate experimental results, and the triangular markers correspond to the SMM results for the first two load cases. . . . .	64
4.2	Comparison of first bending natural frequencies for various experimental and predictive methods . . . . .	67
4.3	Comparison of second bending natural frequencies for experimental and predictive methods . . . . .	68
4.4	Comparison of first twisting natural frequencies for predictive methods . . . . .	68
4.5	Time history of frequency sweep experiment with varying excitation accelerations . . . . .	70
4.6	Comparison of first bending natural frequencies for increasing excitation accelerations . . . . .	71

5.1	Experimental fighter jets which used bend-twist coupling in their wing skins from [23] and [24] . . . . .	74
5.2	Marine/tidal turbine examples . . . . .	76
5.3	Machined aluminum mold of flume-scale blade geometry . . . . .	78
5.4	Machined aluminum tooling of twisted chord line for spar manufacture . . . . .	78
5.5	Cured laminate vs. finished spar shape . . . . .	81
5.6	Close-up of machined aluminum insert being epoxied to spar . . . . .	81
5.7	Finished blades with flexible urethane poured over the spars . . . . .	82
5.8	Schematic of the blade ( $BF_{xyz}, BM_{xyz}$ ) and hub ( $HF_{xyz}, HM_{xyz}$ ) load cell co- ordinate systems. . . . .	83
5.9	Placement of laser sensors on turbine blade for load-deformation tests. . . . .	84
5.10	Load-dependent elastic deformation responses of each blade type . . . . .	85
5.11	Deflection-twist relationship, with linear regression plotted . . . . .	87
5.12	Blade load cell measurements with increasing $\lambda$ at $U_{hub} = 0.50$ m/s . . . . .	91
5.13	System performance characteristics with increasing $\lambda$ at $U_{hub} = 0.50$ m/s . . . . .	92
A.1	Cure profile from Hexcel for IM7/8552 . . . . .	105
A.2	Vacuum bagging diagram for autoclave-cured composite laminates, schematic sourced from [29] . . . . .	106

# List of Tables

2.1	Specimen geometry for hot-press-cured beams . . . . .	11
2.2	Specimen geometry for autoclave-cured beams . . . . .	11
2.3	Shape functions table . . . . .	33
3.1	Elastic modulus averages between experiments for steel beams . . . . .	60
3.2	Elastic modulus averages between experiments for composite beams . . . . .	61
3.3	Material properties for finite element models of experiments . . . . .	62
5.1	Blade material properties . . . . .	80

# Chapter 1

## Introduction

### 1.1 Motivation

Carbon fiber composites have seen increased use in structural applications in the last half century due to their high specific strength and stiffness as compared to alloys, plastics, or other common structural materials. Many high-performance structures benefit from the use of composite laminates where high stiffness, light weight, and reduced part count is required such as in racecars, motorcycles, spacecraft, aircraft, and turbine blades. Composite fiber laminates are a set of materials comprised of long stretches of fiber coated with an epoxy resin “matrix,” laid up together in layers to form the finished laminate. Usually, the fibers are made from carbon or glass and are strung together in bundles called tows and woven or laid out directionally in sheets. The lamina are inherently orthotropic and can be combined in virtually endless configurations, the combinations of which each resulting in a laminate with potentially different structural characteristics. Most lamina configurations result in some degree of laminate anisotropy. Designing with composite fiber laminates requires the engineer to possess an understanding of Classical Laminated Plate Theory (CLPT) [1] to appropriately engineer a laminate with the lamina in the correct orientations to satisfy design

objectives. A particular subset of configurations can conveniently result in quasi-isotropic laminates. Quasi-isotropic laminates are extremely commonly used in aerospace, automotive and recreational fiber reinforced polymer (FRP) applications and are colloquially known as “black aluminum” for their ease of design and analysis. Other configurations, however, can be better suited for component design as their anisotropy can result in coupled structural response, where the deformations of the laminate can be coupled between extension and bending, extension and twisting, or bending and twisting. Furthermore, the degree of coupling between these responses can vary based on the fiber angles of each lamina that comprise the laminate. To this end, FRPs can be used outside of a quasi-isotropic structural design state as a tailorable structural material that provide the engineer with features to craft a particular structural response to a given loading. This is highly unusual structural behavior but can be exploited in specific engineering applications that might require such a response. The engineer can now design parts to be stiffer along the load path, reducing excess material, thus producing a more efficient design.

A particularly common use case where composite fiber laminates are advantageous comes in the form of cantilevered structural members. Obvious and observable applications of cantilever beams as structural members are airplane wings, helicopter blades, wind and marine turbine blades, solar sails, and satellite antennae. Of particular importance with beams are their ability to handle transverse loads due to gravity, lift, or thrust as well as stability under dynamic loading to reduce flutter, divergence, and localized failure. A certain subset of composite laminates have characteristics that couple the transverse bending response with the torsional twisting response. These laminates are appropriately called bend-twist coupled laminates. Bend-twist coupled beams have application in flutter control for forward-swept wings on experimental aircraft [2] as well as passively adaptive wind [3,4] and marine turbine blades [5–7]. Understanding the structural response of bend-twist coupled laminates is important to proper engineering and design. The goal of this work is to develop

a comprehensive understanding of the structural behavior of bend-twist coupled cantilever beams through experimentation, analytical formulations, and finite element analyses to aid the engineer in applying the knowledge to the development of novel, applications such as bend-twist coupled marine turbine blades.

## 1.2 Background

Bend-twist coupling can occur a number of ways in structures. For homogeneous, isotropic, structures with axis-symmetric cross-sections such as a metallic I-beam, the beam exhibits a combined flexural and torsional response when it is loaded eccentrically from its shear center, such as on a corner or edge of the beam. This is essentially a mechanical coupling and is mitigated by ensuring the load path travels through the shear center of the beam. Similarly, flexural-torsional coupling occurs in open-cross-section structures such as C-channel beams or slit tubes due to the shear center and the mass center of the cross section being non-coincident. Even when loaded at the mass center, the beam will still exhibit a twisting response due to the non-symmetrical cross section about the bending axis. These instances of bend-twist coupling, however, are fundamentally different from coupling that occurs due to the composite layup schedule. With composite laminates, the orientation of each ply within the laminate contributes to the global structural response based on its orientation. Arbitrarily oriented lamina within a laminate can induce multiple couplings if the laminate is asymmetric and unbalanced about the laminate mid-line. Bend-twist coupling occurs specifically when the laminate is ply-symmetric about the mid-line, but unbalanced, meaning that the laminate doesn't contain a  $-\alpha$  angle ply for each  $\alpha$  ply, where  $\alpha$  is the ply's fiber angle, as in Figure 1.1. For these laminates, the cross section is symmetric and the mass and shear axes are coincident but the coupling still remains due to the global material anisotropy.



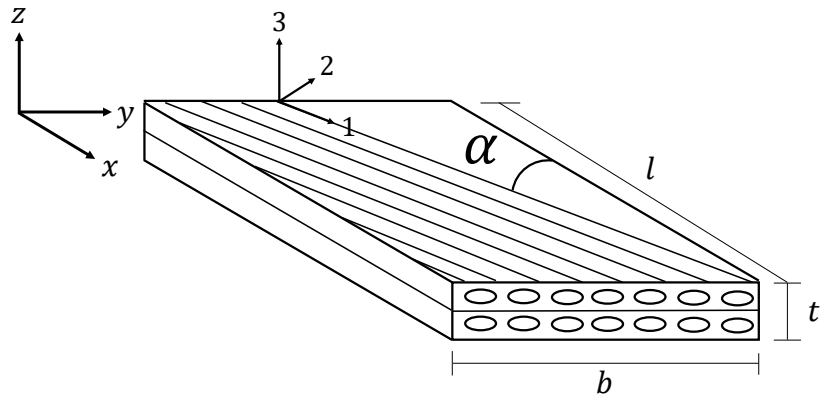


Figure 1.1: Schematic of an off-angle unidirectional laminate with fiber angle,  $\alpha$

Bend-twist coupling was perhaps most famously introduced in the Grumman X-29, an experimental aircraft with forward-swept wings that had tip divergence issues which were mitigated by introducing bend-twist coupling to keep the angle of attack of the wings in check. Research has also been conducted on incorporating bend-twist coupling in commercial aircraft wings to passively alleviate gust loadings in [8]. In [8], it was also found that the inclusion of bend-twist coupling could strongly reduce (between 20% and 45%) the wing's



Figure 1.2: NASA photograph of the Grumman X-29 in banked flight

root spanwise bending moment on Boeing 737's and 777's by mitigating the angle of attack under the gust loading scenario. The work in [8] has not been implemented in application to date, however. Alternatively, industry, military, and the U.S. government have long been interested in bend-twist coupled propeller blades as the coupled deformation response can alleviate effects of cavitation in marine propellers and improve energy efficiency. A fairly comprehensive review can be found in [9]. Bend-twist coupling has also been researched and implemented for years in the wind energy community, both by government institutions such as Sandia National Labs as in [3,4] as well as industry as a means for improved performance and load reduction on the blade structure.

Newer to the bend-twist coupling research community are the applications in marine tidal turbines. Tidal turbines are typically placed in energy dense regions of water where the loading environment can vary drastically in a short period of time. Bend-twist coupling was proposed as a mechanism by which the blades could passively articulate pitch and angle of attack in real time, adapting to the fluid flow without having to be mechanically actuated. Until recently, analysis on tidal turbines assumed the blades to be rigid. Some studies have investigated the effects of flexible blades on turbine level performance [10] while a number of researchers [6, 7] are modeling flexible, adaptive marine turbine blades. Work in [11] reviews the current state of adaptive composites for marine applications, and emphasizes the advantages associated with passive adaptation on blade and turbine performance. In [11], current challenges and future research directions are also discussed, citing physical testing as an element of the research that is lacking as little investigation has occurred in the experimental regime until very recently in [5].

Furthermore, numerical analyses of composite marine structures that incorporate bend-twist coupling are often computationally demanding, requiring fluid-structure interaction, the joining of boundary element models and finite element models to characterize their behavior. The analyses can become increasingly complicated in turbulent or highly dynamic

loading conditions. Even the characterization of the static structural response of a bend-twist coupled laminate is complicated enough to warrant finite element modeling, as CLPT does not apply to transverse load cases or curved laminates, and no stiffness matrix method approach to analysis is regularly available for anisotropic structures that result in deformation coupling. The structural coupling that arises from the material anisotropy makes it difficult for the engineer to immediately intuit the structural behavior of loaded bend-twist coupled laminates and thus is an important subject of investigation as an aid in the understanding and intuition of such structures.

### 1.3 Outline

The research presented herein includes experimental, analytical, and numerical investigations to better understand the nuances of the structural response of bend-twist coupled laminate beams and how they can be applied to a marine turbine blade development to increase the performance characteristics of tidal turbines. The objectives of the study are to: (1) experimentally evaluate the relationship between laminate fiber angle, degree of bend-twist coupling, and overall structural response to static and dynamic loading conditions, (2) compare experimental results to existing analytical methods for analysis, (3) generate finite element models of the test articles to compare with the experimental results, (4) and apply the findings to the design, analysis, testing, and manufacture of a flume-scale bend-twist coupled marine turbine blade. An additional key objective includes an effort to develop an analytical stiffness method approach to analysis of bend-twist coupled laminates as a design tool to circumvent the requirement of a finite element model for every analysis.

The research presented herein is significant for its contribution towards developing a greater understanding of bend-twist coupling in composite laminates in order for the engineer to intuitively apply their use in a structural setting. The motivation for this work comes

from the inclusion of bend-twist coupling in marine turbine blades, but can be extended to any surface which needs to pitch as well as deflect. Furthermore, the basis for development of the element stiffness matrix for a bend-twist coupled laminate can be extended in theory to any combination of coupling, should the engineer choose to investigate laminates with bend-extensional coupling or extensional-twist coupling.

This thesis is organized as follows: Chapter 2 investigates the manufacture and fundamental mechanics of bend-twist cantilevers through experimentation, finite element modeling, and development and use of static and dynamic analytical models. Details of four experiments conducted on beams with varying degrees of bend-twist coupling are presented. The development of an appropriate finite element model in ABAQUS is presented along with the respective steps included and all noteworthy parameters. A new analytical stiffness matrix method for formulating a bend-twist coupled beam element is developed and presented in detail. Eigen-solutions for the natural frequencies of bend-twist coupled beams are also presented by solving the equations of motion for the continuous system. Chapter 3 covers material property testing that was conducted on the manufactured composite beams. The elastic modulus and corresponding bending rigidity of carbon fiber composites are notoriously difficult to characterize, therefore a comprehensive set of experiments was required to most accurately quantify the material properties of the laminates. Several experimental methods for establishing elastic modulus were tested and the results are presented. Chapter 4 presents a comparison of experimental results with predictions by analytical and numerical models, including a discussion of the results and their respective shortcomings. Chapter 5 transitions into the application of bend-twist coupling to a structural design setting. General historical applications are briefly covered but then focused into the application for passively adaptive marine turbine blades. A literature review and the status of current work with bend-twist coupled turbine blades is presented as well as a novel flume-scale experiment in which passively adaptive blades are compared to standard, non-twisting blades. Project

objectives for the blade design and experimentation are established. The design, analysis, manufacture, structural characterization testing, and experimental results of flume-scale tidal turbine blades are discussed in detail. The results from the turbine-level experiment are discussed briefly as well. Chapter 6 summarizes the conclusions of the research presented herein, discusses the existing limitations in analysis and the analytical models, and includes recommendations for future investigations.

# Chapter 2

## Fundamental Mechanics of Bend-Twist Coupled Beams

### 2.1 Overview

This section establishes multiple methods by which bend-twist coupled laminate beams can be characterized statically and dynamically. The ultimate goal of this section is to characterize beam behavior to allow for the development of accurate models. Four experiments were conducted to provide data for model validation. Additionally, a beam element for use in the stiffness method is proposed and developed as a complimentary analysis tool to ABAQUS finite element modeling (FEM).

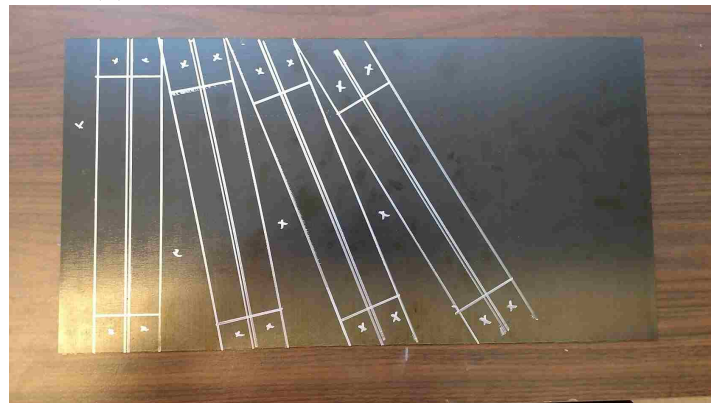
### 2.2 Beam Specimen Manufacture

The material used in this research all originated from a roll of Hexply IM7/8552 that was donated by the Air Force Research Labs Space Vehicles Directorate (AFRL/RV) for use in the University of Washington's (UW) Civil and Environmental Engineering (CEE) department.

Over the course of the conducted research, several laminated plates were manufactured for experimentation on an as-needed basis. The laminates were manufactured such that they were large enough that various beams of varying fiber angle could be cut from them. An example of this can be seen in Figure 2.1. For each laminate, eight individual lamina were cut from the roll using an Autometrix CNC fabric cutting machine and laid up as a large rectangular plate ( $[0]_8$ ). One laminate was cured via hot press while the others were cured in an autoclave, both using a 2-stage curing cycle provided by the manufacturer of this material, Hexcel. Details regarding the autoclave bagging process and cure profile stages are presented in the Appendix (A.1).



(a) Finished cured laminate from hot press



(b) Template for cutting beams of varying fiber angles

Figure 2.1: Cured laminate and cut template

Hot Press Cured Beams				
Beam	Width (mm)	Length (mm)	Thickness (mm)	Thickness Loss
0 degree (1)	24.6	254	0.85	18.8%
0 degree (2)	25.1	254	0.85	18.8%
10 degree (1)	24.4	254	0.86	17.6%
10 degree (2)	24.6	254	0.85	18.8%
20 degree (1)	24.9	254	0.86	17.6%
20 degree (2)	23.6	254	0.86	17.6%
30 degree (1)	24.9	254	0.86	17.6%
30 degree (2)	24.9	254	0.86	17.6%

Table 2.1: Specimen geometry for hot-press-cured beams

11

Autoclave Cured Beams				
Beam	Width (mm)	Length (mm)	Thickness (mm)	Thickness Loss
0 degree (1)	24.4	250	0.77	26.5%
0 degree (2)	24.4	250	0.81	22.7%
10 degree (1)	24.2	250	0.79	24.6%
10 degree (2)	24.8	250	0.79	24.6%
20 degree (1)	23.5	250	0.81	22.7%
20 degree (2)	24.5	250	0.80	23.7%
30 degree (1)	24.6	210	0.81	22.7%
30 degree (2)	24.3	250	0.80	23.7%

Table 2.2: Specimen geometry for autoclave-cured beams



Laminates comprised of all lamina laid up at a constant fiber angle are called “unidirectional (uni) laminates.” Unidirectional laminates exhibit highest levels of bend-twist coupling but can suffer from a “ply consolidation” phenomena, where the fibers from one lamina get pushed into and combined with the fibers from another lamina. The resulting laminate will be thinner than the product of the lamina thickness and number of plies. Thickness reductions of such laminates vary based on the curing method, therefore must be examined on a case by case basis. Autoclave-cured laminates might exhibit larger reductions in thickness due to some resin content being vacuumed out during the cure process. Alternatively, hot-press-cured laminates may not have constant thickness across the plate due to the flatness limitations on the hot press platens. Furthermore, the thickness of the plate could vary along its geometry simply due to the resin distribution during curing. Significant differences in thickness reductions were apparent between the two laminates as depicted by Tables 2.1 and 2.2. For laminates manufactured in this work, the hot-press cures exhibited an average thickness reduction of about 18% while the autoclave-cures exhibited an average thickness reduction of about 24%. Despite this, unidirectional laminates serve as a useful baseline for exploring bend-twist coupling mechanics.

In non-unidirectional layups such as cross-ply or quasi-isotropic layups, the adjacent lamina are at different fiber angles and do not allow for the fibers to push into each other and compress. Bend-twist coupling can still be achieved without “consolidation” by designing an unbalanced laminate as long as the fiber angles vary between layers above and below the midline. It was shown in [12] that the global load-deformation behavior of any laminate layup can be characterized by a unidirectional equivalent. However, for the research presented here, the highest possible amounts of bend-twist coupling were desired, which required the laminates to be off-angle ( $\alpha \neq 0$ ) unidirectional layups. Each material possesses a unique relationship between amount of bend-twist coupling and lamina fiber angle. Laminates with the highest degrees of coupling will contain all lamina at the same prescribed fiber angle

which explains the motivation for the laminate design used in this research. It is to be noted, though, that this is not typical in industry use of composites.

### 2.3 Experimental Methods

Composite laminates typically exhibit discontinuous stress distribution between layers. An example of the through-thickness stress and strain distribution for three quasi-isotropic laminates in bending is provided by Figure 2.2 (taken from [13]). Because the through-thickness stress distributions within a laminate can vary so drastically, design criteria are often strain or displacement based.

For the special case of unidirectional layups such as those used in this research, the stress variation is linearly distributed, but the displacement-based design criteria remains intact. For this reason, it is a sensible starting point of any investigation into composite laminate beams to establish the load-deflection relationship under the appropriate loading conditions.

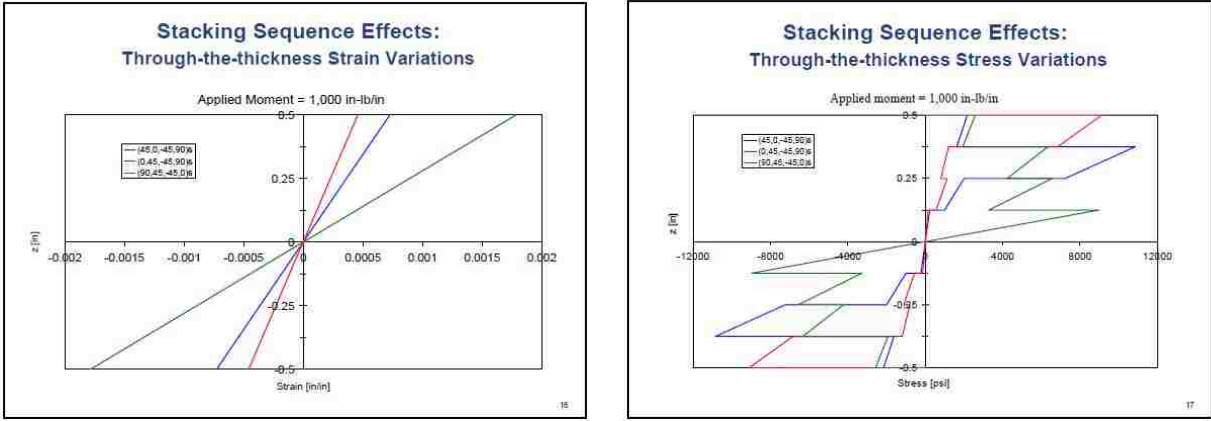


Figure 2.2: Through-the-thickness strain and stress distributions of laminate in bending

### 2.3.1 Quasi-Static Force-Deflection

Most cantilever applications of composite beams experience some kind of distributed load such as self-weight, lift, drag, wind pressure, etc. Under static loading and for large deflections, however, it can be hard to induce such a load case. Due to this, a single point end load was used as a simplification for loading in this experiment to characterize behavior. The force-deflection response of bend-twist beams of varying fiber angle was investigated when subjected to this load case as an opening step in characterizing their structural response.

For this experiment, each beam had a small hole drilled into its end, and was loaded incrementally with masses from 50g to 250g. Of interest were the beams' vertical deflections of each edge. The mid-line vertical deflections were averaged from the deflections of the edges, while the beam twist could be approximated with the following equation

$$\theta_x = \sin^{-1} \left( \frac{u_L - u_R}{b} \right), \quad (2.1)$$

where  $\theta_x$  is beam twist,  $u_L$  and  $u_R$  are vertical displacements of left and right edges, respectively, and  $b$  is beam width. Beam displacements were measured at each edge 150 mm from the boundary after each load increment. The edges were measured at the start under self-weight but no applied loading to provide a baseline for the displacements. Loads were applied incrementally with the beam deflections were measured via a MicroEpsilon optoN-CDT 1700-500 laser sensor and data recorded manually once the beams came to equilibrium after each incremental step. A schematic explaining Equation (2.1) is shown in Figure 2.3.

The laminate fiber angle dictates the degree of bend-twist coupling but comes at the expense of bending stiffness. This tradeoff between bending stiffness and twist coupling is shown experimentally in Figure 2.4. The beams with fiber angles that deviate more from  $0^\circ$  deflect more but also twist more. This will be the case up until the fiber angle that maximizes bending-torsional coupling, at which point increasing the fiber angle will reduce the bending

stiffness as well as reduce beam twist until  $90^\circ$  where bending stiffness is minimized and no bend-twist coupling occurs.

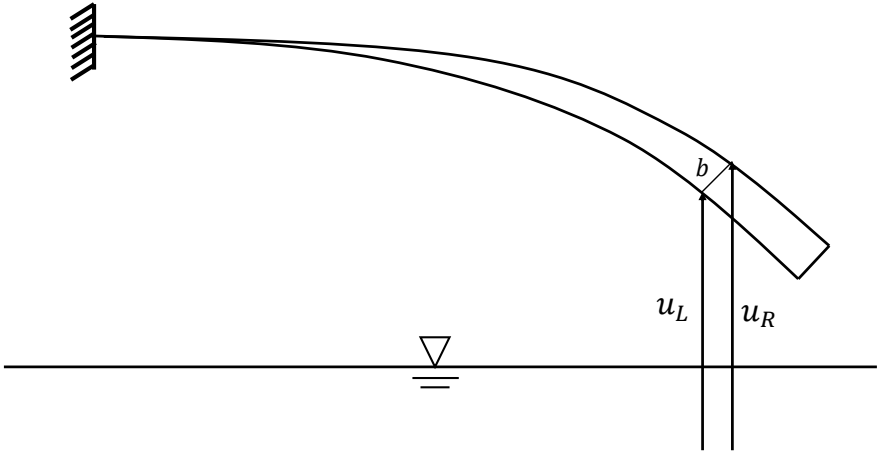


Figure 2.3: Schematic showing laser sensor measurement at each edge and the relation to beam twist



Figure 2.4: Deflection of varied fiber angle ( $10^\circ$ ,  $20^\circ$ ,  $30^\circ$ ) beams under identical loading

### 2.3.2 Free Vibration

Of critical importance to all structural evaluations is an eigenparameter analysis to identify fundamental frequencies and mode shapes in order to design appropriately for the loading environment. Arguably the simplest investigation into the fundamental frequency of a cantilevered structure is imparting an impulse and measuring the free vibration response. Beams of varying fiber angles were plucked in an approximate first mode shape and left to ring down. The same MicroEpsilon optoNCDT 1700-500 laser sensor was used in measuring the beam response. The laser sensor captured beam vibration at a sampling rate of 2.5 kHz. The time history data was processed via Fast Fourier Transform (FFT) in MATLAB to obtain the beam response in the frequency domain. The frequency index of the maximum value of Fourier transformed data corresponds to the beam's natural frequency. Experimental setup can be seen in Figure 2.5. Time history data for the impulse and ringdown are shown in Figure 2.6 with the top subfigure corresponding to the ringdown of the  $0^\circ$  beam, increasing in fiber angle until the bottom subfigure for the  $30^\circ$  beam. Because it is difficult to excite higher mode shapes, however, only the first natural frequencies were of interest.



Figure 2.5: Experimental setup for free vibration

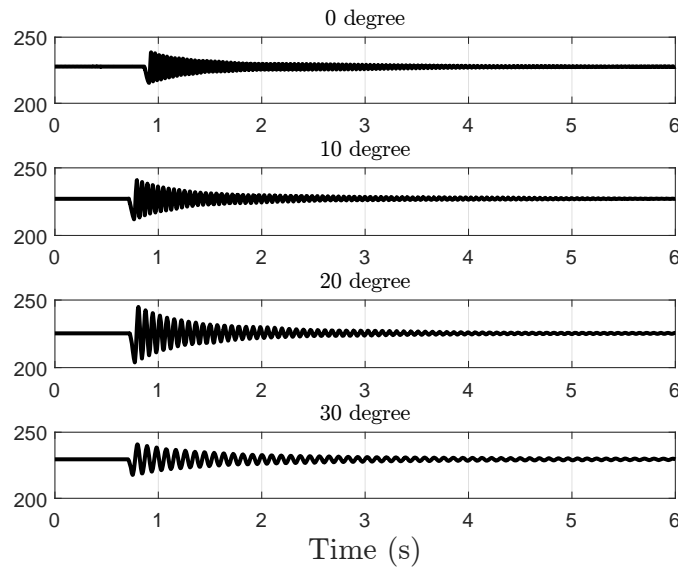


Figure 2.6: Free vibration ringdown for beams of varying fiber angles showing decreasing frequency of vibration for increasing fiber angle. Y-axis values are distance from laser sensor to beam in millimeters.

### 2.3.3 Small Amplitude Frequency Sweep

A separate evaluation of beam natural frequencies was conducted via forced vibration frequency sweeps. This experiment utilized an electrodynamic shaker table for the structural excitation. The beams were each mounted to a fixture on the shaker and the displacement response of the beam captured via laser sensor as seen in Figure 2.7. Controlling the shaker was a LabView VI P-controller that moderated shake table accelerations to keep acceleration constant throughout the sweep. Maintaining constant acceleration or forcing is important in order to generate a relationship only between displacement amplitude and excitation frequency. The particular controller worked most effectively in a small range of frequencies, therefore the shake table excited the beams in a 10 Hz range around the estimated fundamental frequencies from the free vibration experiment. Once again, the beam displacement was recorded by the MicroEpsilon optoNCDT 1700-500 laser sensor and the time history of the response was converted to the frequency domain via FFT in MATLAB. An example of the time history response for a frequency sweep under 1G accelerations can be seen in Figure 2.8 while the frequency domain response is shown in Figure 2.9.

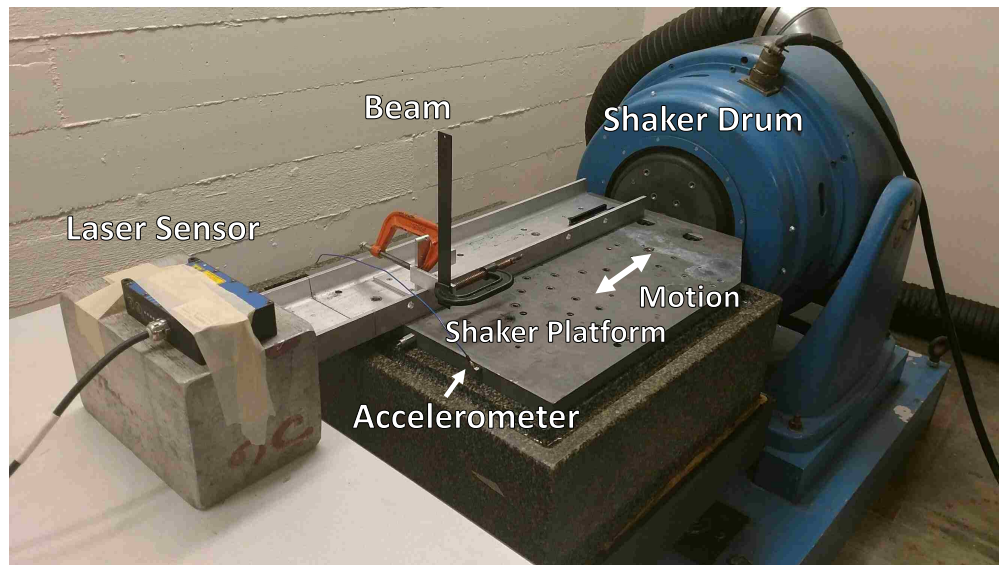


Figure 2.7: Experimental setup for frequency sweep

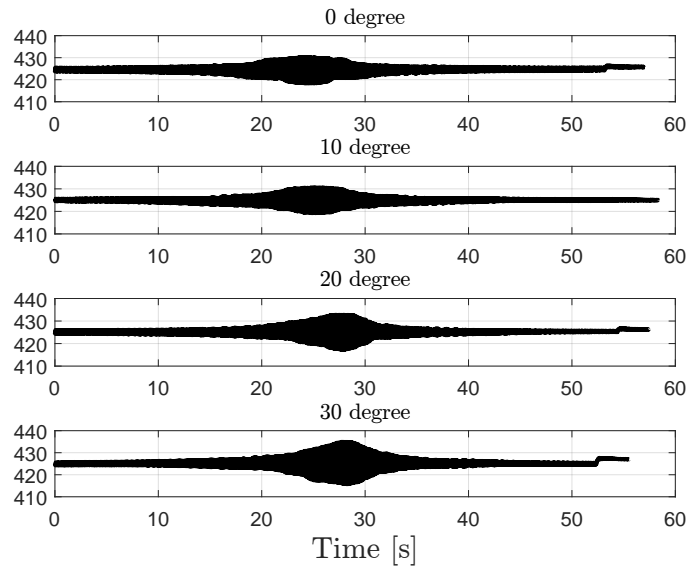


Figure 2.8: Time domain response of 1G frequency sweep on beams of varying fiber angles. Y-axis values are distance from laser sensor to beam in millimeters

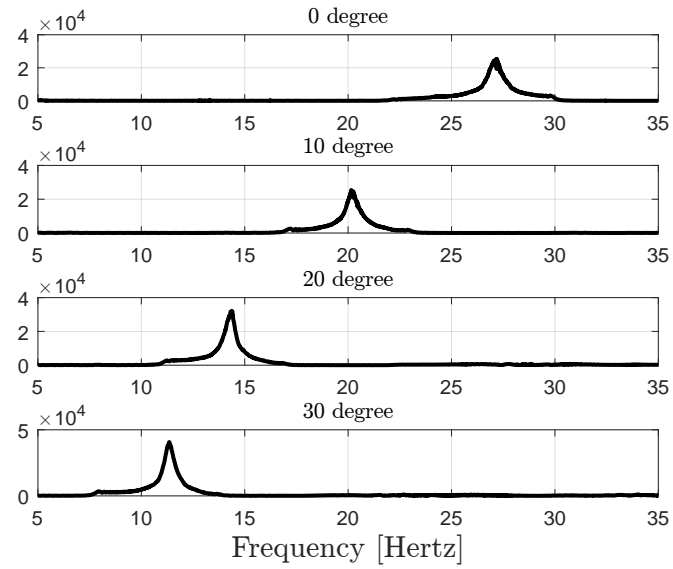


Figure 2.9: Frequency domain response of 1G frequency sweep on beams of varying fiber angles. Y-axis values are power.



### **2.3.4 Large Amplitude Frequency Sweep**

Finally, a large amplitude dynamics experiment was conducted to investigate the potential for any frequency stiffening or softening effects of the beams under large amplitude vibration. With structures that undergo large enough deflections, there is potential for the natural frequencies to increase (stiffen) or decrease (soften) based on the geometric nonlinearity associated with catenary tensions or out-of-plane displacements. Frequency sweeps of accelerations ranging from 1G to 20G were conducted on each beam in the autoclave-cured batch. Conducting frequency sweeps at varying amplitudes could indicate whether or not the natural frequency varies with forcing amplitude. Frequency stiffening effects would result in increasing natural frequencies with the increased forcing amplitude, while frequency softening would result in decreasing natural frequencies with the forcing amplitude increase. The experimental setup for this experiment was identical to that in Figure 2.7. The only variable was the shaker acceleration programmed in the controller and the number of tests conducted on each beam. Results, and comparison to theoretical results, will be presented in detail in Chapter 4.3.

## **2.4 ABAQUS Finite Element Modeling**

### **2.4.1 Structure Properties**

Commercial finite element software, ABAQUS [14], by Dassault systems was used for all numerical modeling in this research. Four finite element models (FEMs) were developed, one for each corresponding beam's fiber angle based on average geometric properties associated with each respective beam. The material properties and their development are covered in detail in Chapter 3.6. Geometric properties in the models were averaged values for each set of beams from Tables 2.1 and 2.2, respectively. Material properties for the IM7 used in the

models are as follows:  $E_1 = 141$  GPa,  $E_2 = 8.96$  GPa,  $G_{12} = 4.93$  GPa, and  $\nu_{12} = 0.316$ , which were established from testing conducted in Chapter 3.6. Material properties were initially taken from a comprehensive report conducted on the material by the National Institute for Aviation Research and can be referenced in [15]. The values presented in the report differ slightly from those presented by the material manufacturer, Hexcel, but were assumed to be more accurate as the data comes from a comprehensive set of tests conducted on laminates similar to those used in this research. Upon initial comparison of the model results to experimental results, the researcher was also prompted to experimentally evaluate material properties so as to develop better agreement between them. Details of the experiments yielding the most accurate material properties are discussed in depth in Chapter 3.6.

The layup and fiber angles were introduced into the models' properties via the composite layup creator tool. The material properties were applied to the entire beam section, given a thickness corresponding to the appropriate thickness from the measured values in the specimen properties Tables (2.1,2.2), and given a fiber offset angle corresponding to whichever beam is being modeled. The model uses three Simpson integration points through the thickness and conducts the section integration during the analysis.

## 2.4.2 Model Steps

Each model has a general, static step for the quasi-static load-deflection experiment, a step for a linear perturbation frequency analysis, and a dynamic implicit step where dynamic forcing can be applied to the model.

In the static step, the load was gradually stepped up to 250g to correspond to the loading steps imposed in the cantilever force-deflection experiment. In that experiment, the beams were end-loaded with masses ranging from 50g to 250g in 20g increments. This step included geometric nonlinearity in order to account for the large displacements experienced by such

thin beams under load. Geometric nonlinearity is expected based on the very apparent deformation visible in Figure 2.4.

For the linear perturbation step, the model generated the first 10 eigenvalues and eigenvectors corresponding to the first 10 natural frequencies and mode shapes of the respective beams. This step allowed for comparison to the linear dynamics experiments of free vibration and small amplitude frequency sweeps. In the frequency sweep experiment, the first and second mode shapes are most dominant due to experimental constraints on the excitation frequency and measurable displacement amplitude. This rendered the higher modes from the linear perturbation analysis interesting but they were not validated against experiments.

The dynamic implicit step was used to input a forcing function into the model to simulate the effects of large amplitude base excitation present in the large amplitude frequency sweep experiment. In this step, a forcing function was generated to match the experimental forcing frequency and acceleration and then input into the model as a time-variant distributed load on the beam's surface. The distributed load was meant to simulate the inertial effects due to the beam's accelerations on the shaker. The forcing function was required to have constant acceleration over a range of increasing frequencies. The function is depicted by Equation 2.2

$$F = A \sin \left[ \omega_1 + \left( \frac{\omega_2 - \omega_1}{b} \right) t \right] t, \quad (2.2)$$

where  $F$  is the force at time increment,  $t$ ,  $A$  is the forcing amplitude in Gs,  $\omega_1$  is the starting frequency,  $\omega_2$  is the ending frequency, and  $b$  is the frequency increment.

Mass-proportional Rayleigh damping was included in the models for the dynamic implicit step. The damping coefficient was calculated via the log-decrement method from the free vibration experiment results using the following Equation 2.3,

$$\delta = \frac{1}{n} \ln \frac{x(t)}{x(t + nT)}, \quad (2.3)$$

where  $x(t)$  is amplitude at time,  $t$ , and  $x(t + nT)$  is amplitude at a peak  $n$  periods away where  $n$  is any integer of successive, positive peaks. The damping ratio can be calculated by

$$\zeta = \frac{1}{\sqrt{1 + \left(\frac{2\pi}{\delta}\right)^2}}, \quad (2.4)$$

which was 0.1% based on data in Figure 2.6. The Rayleigh constant,  $\alpha$ , can be equal to  $2\zeta\omega$  where  $\zeta$  is calculated from above and  $\omega$  is the measured natural circular frequency from the free vibration experiment. The model uses only mass-proportionate damping as the  $\alpha$  damps primarily low frequencies such as those observed in the experiments conducted in this work.

### 2.4.3 Element Details

Four-node, reduced-integration, shell elements (S4R) were chosen for all models. Reduced-integration elements were chosen to mitigate the effects of shear locking and artificial stiffening due to the finite element method of analysis. Four-node elements were employed because a linear stress distribution was thought to provide a sufficient level of gradation across the elements, as well as for speed in analysis. The resulting mesh density contained elements no larger than 12.5% of the beam's width, or 8 elements across the width of the beam. Because the models are approximating deflections and dynamics rather than material stresses or any sort of failure or fracture, the mesh density requirement is not as stringent.

## 2.5 Analytical Formulations

### 2.5.1 Stiffness Matrix Method

The classical stiffness matrix method is a formulation of the equilibrium equations of ‘stick-type’ structures (e.g. beams, frame, trusses). While it may be formulated using variational principles with the finite element method, the resulting equations require no reference to general FEM theory. For beam-type elements, the deformations between nodes can usually be solved exactly, allowing for the formulation of the stiffness matrix directly (usually called the direct stiffness method) without reliance on more typical variational approaches of FEM. The application of the stiffness method to the analysis of laminated composite structures has been limited, however, as the anisotropic laminate response is often more complex than that of an isotropic, homogeneous material. The structural response of steel beam elements, for instance, can be solved using the Euler-Bernoulli beam equation, whereas this is not a practical approach for anisotropic composite beam elements.

The following section details the development of mass and stiffness matrices for a bend-twist coupled beam element for using in a stiffness matrix method approach of analysis. For the remainder of this work, “SMM” shall refer to “stiffness matrix method,” which is derived henceforth.

#### 2.5.1.1 Constitutive Law

For thin, flat, composite laminated beams that have coincident shear, flexural, and elastic centers and are loaded at the midline, the bend-twist coupling is a result of the laminate layup schedule. A weak-form approach with assumptions from classical laminated plate theory (CLPT) can be taken to develop an element stiffness matrix for these coupled laminates if the shape functions are appropriately defined for the coupled structural response. Consider a laminated beam with the coordinate system shown in Figure 2.10, where  $\alpha$  corresponds to

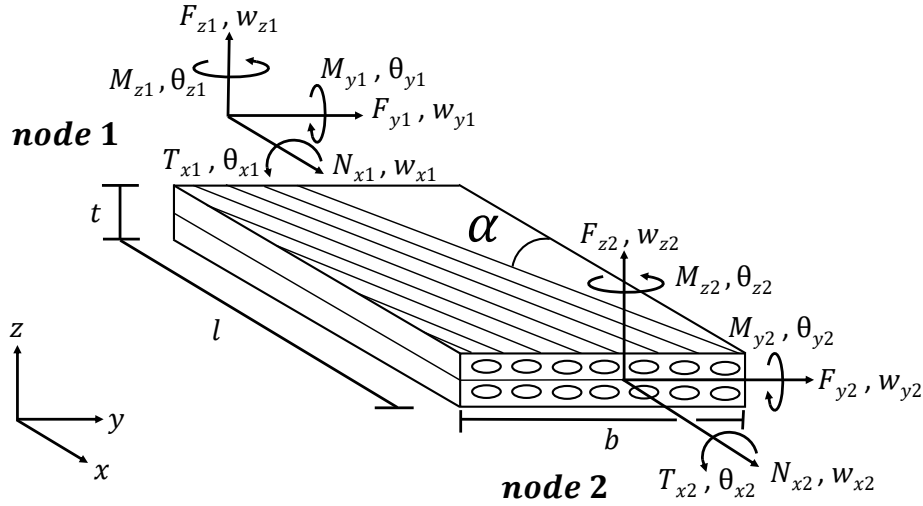


Figure 2.10: Fiber angle offset and coordinate system for unidirectional laminate

the fiber angle of each ply. Nodal coordinate notation follows the right-hand rule, consistent with the approach presented in [16]. This paper will focus on stacked single-orientation laminates where the fiber angle remains the same for each ply as shown schematically in Figure 2.10. This type of laminate results in the highest degree of bend-twist coupling and serves as a useful baseline for exploring the development of this method. However, the formulation presented herein is easily applicable to all symmetric laminates with any amount of bend-twist coupling, including quasi-isotropic and general unbalanced laminates. The properties of composite laminate plates are conventionally expressed in terms of an  $ABD$  matrix which relates three in-plane forces and three bending moments with three mid-plane, in-plane strains and three curvatures. The  $A$ ,  $B$ , and  $D$  terms refer to the corresponding 3x3 submatrices that make up the 6x6  $ABD$  matrix. Any laminate which has a non-zero  $D_{16}$  term in its  $ABD$  matrix can benefit from the formulation presented in this work (see [1] for composite mechanics,  $ABD$  derivation, and CLPT).

Because this work focuses on beam elements rather than plates, the derivation instead begins with a general three-dimensional beam theory approach which simplifies the results as in [17]. Equilibrium and kinematics are established in [17] which result in the load-strain

relation of

$$\mathbf{F} = \mathbf{C} \epsilon, \quad (2.5)$$

where  $\mathbf{C}$  is the constitutive relation matrix,  $\mathbf{F}$  is a vector containing the in-plane forces, and  $\epsilon$  is a vector containing mid-plane strains. For a bend-twist coupled beam, the previous equation can be written as

$$\begin{bmatrix} N_x \\ T_x \\ M_y \\ M_z \end{bmatrix} = \begin{bmatrix} E_x A & 0 & 0 & 0 \\ 0 & GJ & K & 0 \\ 0 & K & E_x I_y & 0 \\ 0 & 0 & 0 & E_x I_z \end{bmatrix} \begin{bmatrix} w'_x \\ \theta'_x \\ \theta'_y \\ \theta'_z \end{bmatrix}, \quad (2.6)$$

where  $E_x A$  represents the axial rigidity,  $GJ$  represents the St. Venant torsional rigidity,  $E_x I_y$  represents the weak axis bending rigidity,  $E_x I_z$  represents the strong axis bending rigidity and  $K$  represents the bending-torsion coupling rigidity. The derivatives in the strain-vector,  $\epsilon$ , are with respect to the element length, or 'x', direction (as per Figure 2.10). This constitutive relation differs from that of an uncoupled structural element whose  $\mathbf{C}$  matrix has zero-valued off-diagonal elements. The constitutive rigidities can be represented by the following expressions per [18] or [19]:

$$\begin{aligned} E_x A &= E_x b t, \\ GJ &= 4b \left( D_{66} - \frac{D_{26}^2}{D_{22}} \right), \\ K &= 2b \left( D_{16} - \frac{D_{12} D_{26}}{D_{22}} \right), \\ E_x I_y &= b \left( D_{11} - \frac{D_{12}^2}{D_{22}} \right), \\ E_x I_z &= E_x \frac{b^3 t}{12}, \end{aligned}$$

where  $E_x$  is the approximate x-direction elastic modulus, the  $D_{ij}$  terms are components of the laminate  $ABD$  matrix, and  $b$  is the beam or plate width (Figure 2.10). The  $D_{ij}$  terms relate bending moments and plate curvature. The dominant coupling parameter in  $K$  is  $D_{16}$ , which relates  $M_y$  and  $\theta'_x$ , or the relationship between beam bending moment and corresponding twisting rate. For uncoupled laminates, this value is zero; it also tends to be close to zero for laminates with small amounts of bend-twist coupling.

### 2.5.1.2 Weak-Form Formulation

A 3D beam element can now be defined with 2 nodes and 6 degrees of freedom per node. The displacement vector takes the form

$$\mathbf{d} = \left[ w_{x1}, w_{y1}, w_{z1}, \theta_{x1}, \theta_{y1}, \theta_{z1}, w_{x2}, w_{y2}, w_{z2}, \theta_{x2}, \theta_{y2}, \theta_{z2} \right]^T, \quad (2.7)$$

where  $w$  and  $\theta$  correspond to the nodal displacements and rotations for the directions denoted in the subscript. Strains from Equation (2.5) can be expressed via the strain-displacement relation as

$$\epsilon = \mathbf{B} \mathbf{d}, \quad (2.8)$$

where  $\mathbf{B}$  is a matrix which contains functions relating strains and nodal displacements; these relations will be discussed in the following subsection. The conventional weak-form derivation based on potential energy minimization results in the following expression relating loads and displacements via an element stiffness matrix. This can be expressed as

$$\mathbf{P} = \left( \int_0^L \mathbf{B}^T \mathbf{C} \mathbf{B} dx \right) \mathbf{d}, \quad (2.9)$$

or more simply

$$\mathbf{P} = \mathbf{K} \mathbf{d}, \quad (2.10)$$



where  $\mathbf{P}$  is the vector of nodal forces and  $\mathbf{K}$  is the resulting element stiffness matrix.

### 2.5.1.3 Strain-Displacement Matrix Derivation

To this point, this method is consistent with the derivation of an uncoupled beam element. For a bend-twist coupled beam element, however, the strain-displacement relation matrix,  $\mathbf{B}$ , is more complicated. Uncoupled beam relations denote twisting strains only due to applied torques at the nodes. As a point of comparison, in [20], while bend-twist coupling is included in the constitutive law (i.e. the  $K$  term is present as in (2.6)), the strain-displacement relationships are derived from classic isotropic beam elements. This approach leads to inaccuracy for strongly coupled laminates where twisting strain is strongly influenced by transverse displacements and beam rotations, the importance of which cannot be ignored in the strain-displacement matrix. The effects of out-of-plane nodal beam displacements and nodal beam rotations,  $w_z$  and  $\theta_y$ , respectively, on beam twist must also be accounted for to completely establish strain-displacement relations.

In order to fully populate the strain-displacement matrix for this type of laminate, the shape functions corresponding to unit element displacements and rotations must be known. Equations (2.11-2.16) are the assumed forms of the six deformation fields (three translations, and three rotations). Using the standard discretization approach, each deformation field is approximated using the nodal degrees of freedom and their respective shape functions. Outside of the standard linear shape functions for axial deformations ( $N_A$ ) and the four cubic bending ( $N_B$ ) and rotation ( $N_R$ ) shape functions well-known to beam theory, shape functions for beam twist due to transverse nodal displacements and beam twist due to nodal rotations must be derived. Mid-span twist induced by transverse displacements and bending rotations at the nodes can be observed in experiments and FEM simulations, indicating that new shape functions must be added. The requirement for new shape functions can be understood by examining the displacement equations for each degree of freedom, noting that

the  $\theta_x$  equation contains additional expressions to fully quantify the twisting response.

$$w_x = N_{A1} w_{x1} + N_{A2} w_{x2} \quad (2.11)$$

$$w_y = N_{B1} w_{y1} + N_{R1} \theta_{z1} + N_{B2} w_{y2} + N_{R2} \theta_{z2} \quad (2.12)$$

$$w_z = N_{B1} w_{z1} + N_{R1} \theta_{y1} + N_{B2} w_{z2} + N_{R2} \theta_{y2} \quad (2.13)$$

$$\begin{aligned} \theta_x = N_{T1} \theta_{x1} + \boxed{N_{\theta_x z_1} w_{z1}} + \boxed{N_{\theta_x \theta_{y1}} \theta_{y1}} + \\ N_{T2} \theta_{x2} + \boxed{N_{\theta_x z_2} w_{z2}} + \boxed{N_{\theta_x \theta_{y2}} \theta_{y2}} \end{aligned} \quad (2.14)$$

$$\theta_y = N_{\theta_y \theta_{y1}} \theta_{y1} + N_{\theta_y z_1} w_{z1} + N_{\theta_y \theta_{y2}} \theta_{y2} + N_{\theta_y z_2} w_{z2} \quad (2.15)$$

$$\theta_z = N_{\theta_z \theta_{z1}} \theta_{z1} + N_{\theta_z y_1} w_{y1} + N_{\theta_z \theta_{z2}} \theta_{z2} + N_{\theta_z y_2} w_{y2} \quad (2.16)$$

The boxed expressions in Equation (2.14) identify the additional shape functions and nodal displacements that contribute to the  $\theta_x$  twist equation. The naming convention on the shape functions is as follows.  $N_{\theta_x z_1}$  refers to the contribution to  $\theta_x$  (twist) by a unit displacement,  $w_z$ , at node 1. Following suit,  $N_{\theta_x \theta_{y2}}$  indicates the contribution to  $\theta_x$  (twist) by a unit rotation,  $\theta_y$ , at node 2. All shape functions are functions of  $x$  through the element length, yet will be denoted simply by  $N$  for brevity.

These additional shape functions can be solved for explicitly in the following fashion. To solve for the  $\theta_x$  relationship due to an imposed nodal displacement,  $w_z$ , we have (from equilibrium or Equation (2.6)),

$$T_x = GJ \theta'_x + K \theta'_y, \quad (2.17)$$

$$M_y = K \theta'_x + E_x I_y \theta'_y. \quad (2.18)$$

With Euler-Bernoulli kinematics,  $w'_z = -\theta_y$ , Equations (2.17) and (2.18) become

$$T_x = GJ \theta'_x - K w''_z, \quad (2.19)$$

$$M_y = K \theta'_x - E_x I_y w''_z. \quad (2.20)$$

As there are no applied loads in-span,  $M_y$  is a linear function of position and thus  $M''_y = 0$ .

Equation (2.20) can be differentiated twice to give

$$0 = K \theta'''_x - E_x I_y w''''_z. \quad (2.21)$$

Likewise, the torque is constant within the element, meaning that the derivative of Equation (2.17) is also equal to zero. Combining this and Equation (2.21) yields two uncoupled differential equations,

$$\left( E_x I_y - \frac{K^2}{GJ} \right) w''''_z = 0, \quad (2.22)$$

$$\left( E_x I_y - \frac{K^2}{GJ} \right) \theta'''_y = 0, \quad (2.23)$$

which reduce to the standard governing beam equations

$$w''''_z = 0, \quad (2.24)$$

$$\theta'''_y = 0. \quad (2.25)$$

The solution form for transverse displacement,  $w_z$ , with the nodal deformations representing the boundary conditions yields

$$w_z(x) = w_{z1} N_1(x) + \theta_{y1} N_2(x) + w_{z2} N_3(x) + \theta_{y2} N_4(x). \quad (2.26)$$

In this example derivation, imposing only a displacement at node 1 results in a simplified displacement equation,

$$w_z(x) = w_{z1} N_1(x), \quad (2.27)$$

with  $N_1(x)$ , in this case, equal to the standard beam bending shape function,  $N_1(x) = 1 - 3(\frac{x}{L})^2 + 2(\frac{x}{L})^3$ . Equation (2.27) can be combined with the derivative of Equation (2.17) (because  $T'_x = 0$ ) to give

$$GJ \theta''_x - K w_{z1} N_1'''(x) = 0. \quad (2.28)$$

Evaluating  $N_1'''(x)$ , twice-integrating  $\theta''_x$ , and applying zero  $\theta_x$  boundary conditions gives the resulting shape function for  $\theta_x$  due to a displacement of  $w_{z1}$

$$\theta_x = \frac{6K}{GJL^3} (x^2 - Lx) w_{z1} = N_{\theta_x z_1} w_{z1}. \quad (2.29)$$

A similar approach can be taken to yield the shape function for  $\theta_x$  due to a rotation,  $\theta_y$  (noting that the boundary conditions must be altered accordingly), of

$$\theta_x = \frac{3K}{GJL^2} (Lx - x^2) \theta_{y1} = N_{\theta_x \theta_{y1}} \theta_{y1}. \quad (2.30)$$

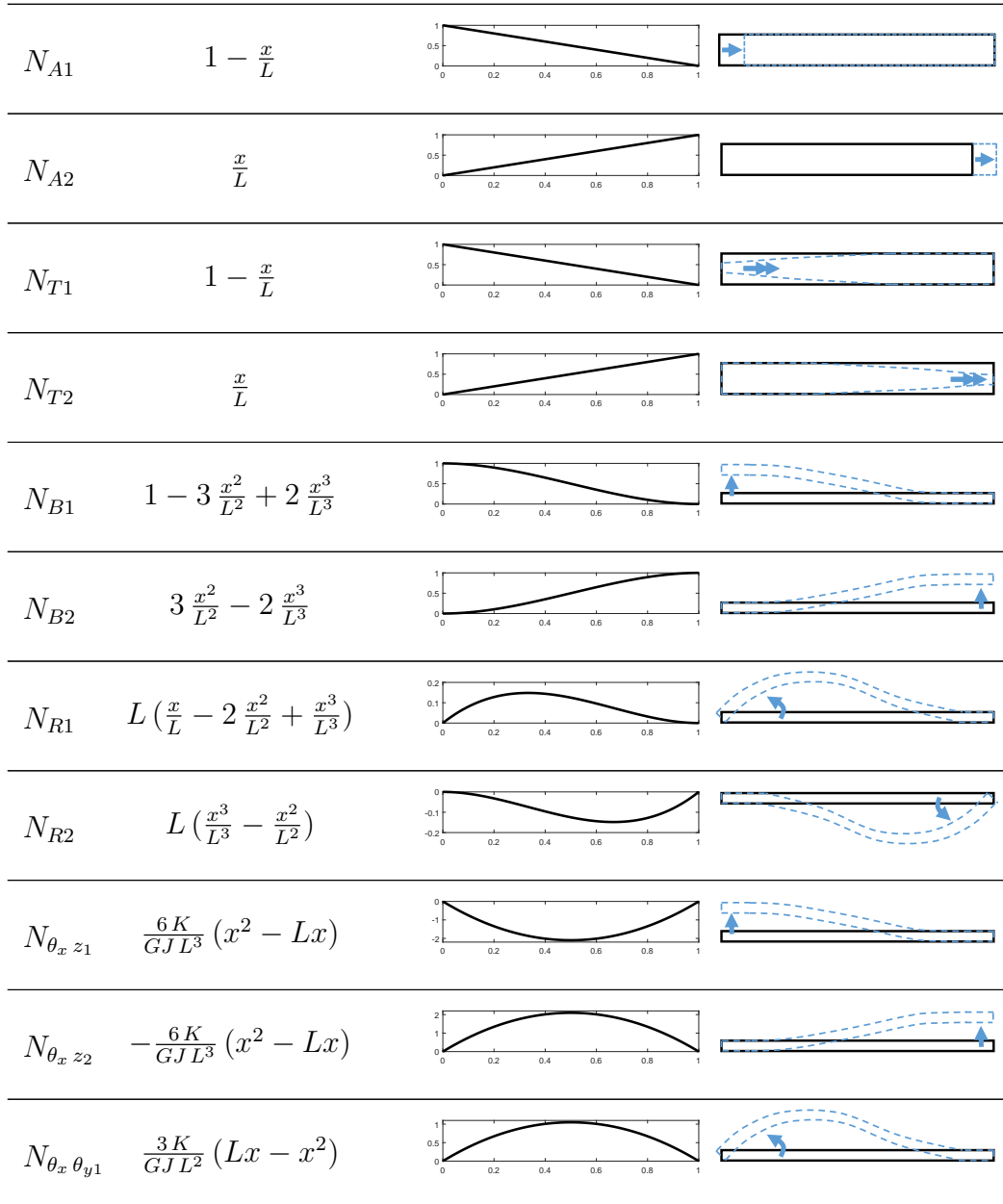
The additional bend-twist shape functions come directly from the governing differential equations in the same way as the traditional isotropic Euler-Bernoulli shape functions. One difference, however, is that they include material properties and thus are not purely kinematic relationships. The magnitude of the deformation in the extra relations is conditional on the relationship between coupling and torsional rigidities, not on kinematics alone.

The shape functions,  $N$ , representing the element displacement field for each degree of freedom are listed in Table 2.3. Having established the appropriate shape function relations for coupled laminated beams, the complete strain-displacement matrix,  $\mathbf{B}$ , can now be written using the first derivatives with respect to  $x$  of the appropriate shape functions, and the

strains can now be more completely expressed as

$$\epsilon_i = B_{ij}(x) d_j = \frac{d N_{ij}(x)}{dx} d_j, \quad (2.31)$$

where



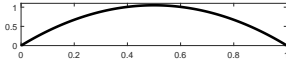
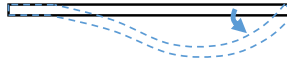
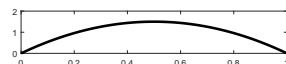
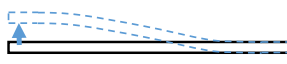
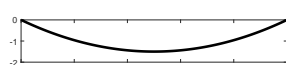
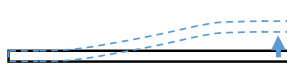
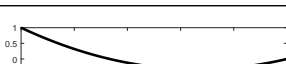
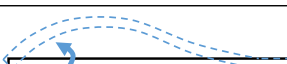
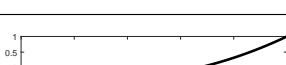
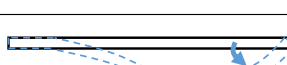
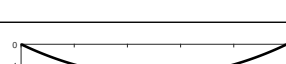
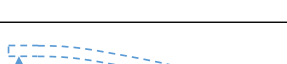
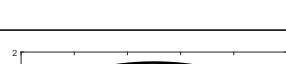

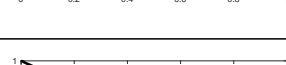
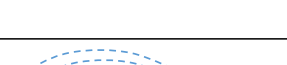
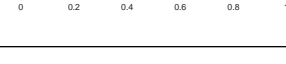

$N_{\theta_x \theta_{y2}}$	$-\frac{3K}{GJL^2} (Lx - x^2)$		
$N_{\theta_y z_1}$	$6 \frac{x}{L^2} - 6 \frac{x^2}{L^3}$		
$N_{\theta_y z_2}$	$-6 \frac{x}{L^2} + 6 \frac{x^2}{L^3}$		
$N_{\theta_y \theta_{y1}}$	$1 - 4 \frac{x}{L} + 3 \frac{x^2}{L^2}$		
$N_{\theta_y \theta_{y2}}$	$3 \frac{x^2}{L^2} - 2 \frac{x}{L}$		
$N_{\theta_z y_1}$	$-6 \frac{x}{L^2} + 6 \frac{x^2}{L^3}$		
$N_{\theta_z y_2}$	$6 \frac{x}{L^2} - 6 \frac{x^2}{L^3}$		
$N_{\theta_z \theta_{z1}}$	$1 - 4 \frac{x}{L} + 3 \frac{x^2}{L^2}$		
$N_{\theta_z \theta_{z2}}$	$3 \frac{x^2}{L^2} - 2 \frac{x}{L}$		

Table 2.3: Shape functions table

The complete, coupled  $\mathbf{B}$  matrix that is used in the analysis presented here is expressed as the following:

$$\mathbf{B} = \begin{bmatrix} N'_{A1} & 0 & 0 & 0 & 0 & 0 & N'_{A2} & 0 & 0 & 0 & 0 & 0 \\ 0 & 0 & \boxed{N'_{\theta_x z_1}} & N'_{T1} & \boxed{N'_{\theta_x \theta_y 1}} & 0 & 0 & 0 & \boxed{N'_{\theta_x z_2}} & N'_{T2} & \boxed{N'_{\theta_x \theta_y 2}} & 0 \\ 0 & 0 & N'_{\theta_y z_1} & 0 & N'_{\theta_y \theta_y 1} & 0 & 0 & 0 & N'_{\theta_y z_2} & 0 & N_{\theta_y \theta_y 2} & 0 \\ 0 & N'_{\theta_z y_1} & 0 & 0 & 0 & N'_{\theta_z \theta_z 1} & 0 & N'_{\theta_z y_2} & 0 & 0 & 0 & N'_{\theta_z \theta_z 2} \end{bmatrix},$$

where the boxed terms are the strain-displacement relations that arise due to the newly-derived shape functions. In a conventional, uncoupled, approach, these boxed terms would be zero. Note that Equation (2.6) only requires the four strains,  $w'_x, \theta'_x, \theta'_y, \theta'_z$ , which are represented by the respective rows in  $\mathbf{B}$ .

#### 2.5.1.4 Element Stiffness Matrix Calculation

The integration from Equation (2.9) can now be performed with the constitutive relation from Equation (2.5) to yield the 12x12 element stiffness matrix for the coupled beam. The boxed  $K_x$  expressions in the stiffness matrix are expressed in Equations (2.32-2.35) and are a result of the inclusion of the extra strain-displacement relations in **B**. Without the extra relations, the integration would simply yield the standard uncoupled stiffness matrix expressions of the form  $\frac{12 E_x I_y}{L^3}$ ,  $\frac{6 E_x I_y}{L^2}$ ,  $\frac{4 E_x I_y}{L}$ , and  $\frac{2 E_x I_y}{L}$ . The new stiffness expressions are the following:

$$K_1 = \frac{12 (-K^2 + GJ E_x I_y)}{GJ L^3}, \quad (2.32)$$

$$K_2 = \frac{6 (K^2 - GJ E_x I_y)}{GJ L^2}, \quad (2.33)$$

$$K_3 = \frac{-3 K^2 + 4 GJ E_x I_y}{GJ L}, \quad (2.34)$$

$$K_4 = \frac{-3 K^2 + 2 GJ E_x I_y}{GJ L}. \quad (2.35)$$



The fully coupled element stiffness matrix,  $\mathbf{K}$ , used in the analysis presented here is expressed as the following:

$$\mathbf{K} = \begin{bmatrix} \frac{E_x A}{L} & 0 & 0 & 0 & 0 & 0 & -\frac{E_x A}{L} & 0 & 0 & 0 & 0 & 0 \\ 0 & \frac{12 E_x I_z}{L^3} & 0 & 0 & 0 & \frac{6 E_x I_z}{L^2} & 0 & -\frac{12 E_x I_z}{L^3} & 0 & 0 & 0 & \frac{6 E_x I_z}{L^2} \\ 0 & 0 & \boxed{K_1} & 0 & \boxed{K_2} & 0 & 0 & 0 & \boxed{-K_1} & 0 & \boxed{K_2} & 0 \\ 0 & 0 & 0 & \frac{GJ}{L} & \frac{K}{L} & 0 & 0 & 0 & 0 & -\frac{GJ}{L} & -\frac{K}{L} & 0 \\ 0 & 0 & \boxed{K_2} & \frac{K}{L} & \boxed{K_3} & 0 & 0 & 0 & \boxed{-K_2} & -\frac{K}{L} & \boxed{K_4} & 0 \\ 0 & \frac{6 E_x I_z}{L^2} & 0 & 0 & 0 & \frac{4 E_x I_z}{L} & 0 & -\frac{6 E_x I_z}{L^2} & 0 & 0 & 0 & \frac{2 E_x I_z}{L} \\ -\frac{E_x A}{L} & 0 & 0 & 0 & 0 & 0 & \frac{E_x A}{L} & 0 & 0 & 0 & 0 & 0 \\ 0 & -\frac{12 E_x I_z}{L^3} & 0 & 0 & 0 & -\frac{6 E_x I_z}{L^2} & 0 & \frac{12 E_x I_z}{L^3} & 0 & 0 & 0 & -\frac{6 E_x I_z}{L^2} \\ 0 & 0 & \boxed{-K_1} & 0 & \boxed{-K_2} & 0 & 0 & 0 & \boxed{K_1} & 0 & \boxed{-K_2} & 0 \\ 0 & 0 & 0 & -\frac{GJ}{L} & -\frac{K}{L} & 0 & 0 & 0 & 0 & \frac{GJ}{L} & \frac{K}{L} & 0 \\ 0 & 0 & \boxed{K_2} & -\frac{K}{L} & \boxed{K_4} & 0 & 0 & 0 & \boxed{-K_2} & \frac{K}{L} & \boxed{K_3} & 0 \\ 0 & \frac{6 E_x I_z}{L^2} & 0 & 0 & 0 & \frac{2 E_x I_z}{L} & 0 & -\frac{6 E_x I_z}{L^2} & 0 & 0 & 0 & \frac{4 E_x I_z}{L} \end{bmatrix}.$$

### 2.5.1.5 Idealized Beam Comparison

The performance of this stiffness method approach to the analysis of bending-torsion coupled beams was evaluated by comparison to a linear elastic ABAQUS/Standard [14] FEM of an idealized test beam. The idealized beam is 2.54 meters long, 0.0254 meters wide, and 0.001048 meters thick. The beam has high length-to-width and width-to-thickness ratios to ensure that the Euler-Bernoulli assumptions are valid as well as to minimize the effects of localized through-width or through-thickness deformation concentrations that arise due to the imposition of displacements at individual nodes.

The lamina properties of the FEM were defined using the composite laminate creator tool. The material used in the analyses was Hexcel IM7/8552 unidirectional carbon fiber composite prepreg. Material properties for the IM7 are as follows:  $E_1 = 164$  GPa,  $E_2 = 8.96$  GPa,  $G_{12} = 4.93$  GPa, and  $\nu_{12} = 0.316$ . It needs to be noted that, in the development and validation of this stiffness method approach, material properties for the IM7/8552 were taken directly from reported values in [15], as opposed to the abridged values established in Chapter 3.6, which are utilized when comparing to the experimental results later in this work.

A total of 1696 four-node, reduced integration shell elements (S4R) were used in the FEM mesh. The beam ends were kinematically constrained to a single point to represent the respective nodes on which boundary conditions could be applied as depicted in Figure 2.11. A unit displacement at node 2 was imposed in each degree of freedom and the respective reaction forces at node 1 were recorded by the ABAQUS model. Evaluation of the stiffness matrix was done by direct comparison of the top-right quadrant to the finite element model reaction forces. Because unit magnitude boundary condition displacements were imposed on node 2 in the FE model, the top-right quadrant represents the reaction forces at node 1 to displacements at node 2.

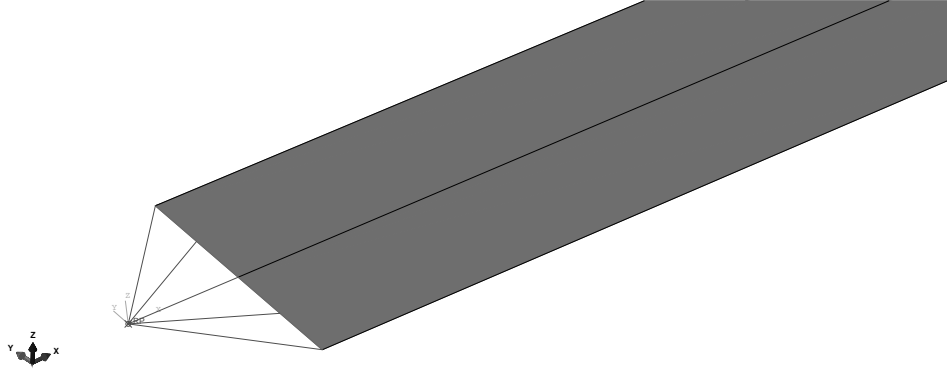


Figure 2.11: Beam end constraints as a single point in finite element model

### 2.5.1.6 ABAQUS vs Stiffness Matrix Values Comparison

The ABAQUS simulations were conducted for fiber angles ranging from  $0^\circ$  to  $90^\circ$  and each set of reaction forces was recorded. In the top-right quadrant, the five terms that govern the beam bending and torsional response are the following:  $-K_1$ ,  $K_2$ ,  $K_4$ ,  $-\frac{GJ}{L}$ , and  $-\frac{K}{L}$ . Both coupled and uncoupled analytical stiffness matrix expressions are plotted for all fiber angles and compared to values obtained from ABAQUS. The comparisons can be seen in Figures 2.12 - 2.16. It should be noted that the  $-\frac{GJ}{L}$  and  $-\frac{K}{L}$  terms are identical for the coupled and uncoupled cases. This is because the additional shape functions for the fully-coupled element do not contribute to those respective stiffnesses.

Note that the uncoupled analytical solution greatly over-predicts stiffness for fiber angles ranging from near  $0^\circ$  to near  $50^\circ$ . This is because it doesn't allow for the element twisting, which leads to artificial stiffening through constraint. The coupled solution is in fact exact as all the shape functions are solved explicitly from the governing equations. The deviation from the FEM solutions is possibly a result of how the displacements were applied or how the reaction force was recovered in the finite element model.

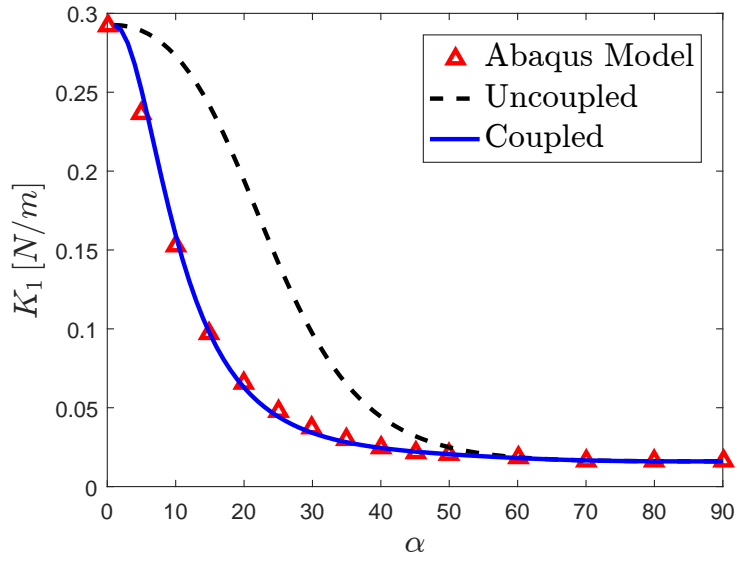


Figure 2.12:  $K_1$ , translational stiffness for an imposed transverse nodal displacement

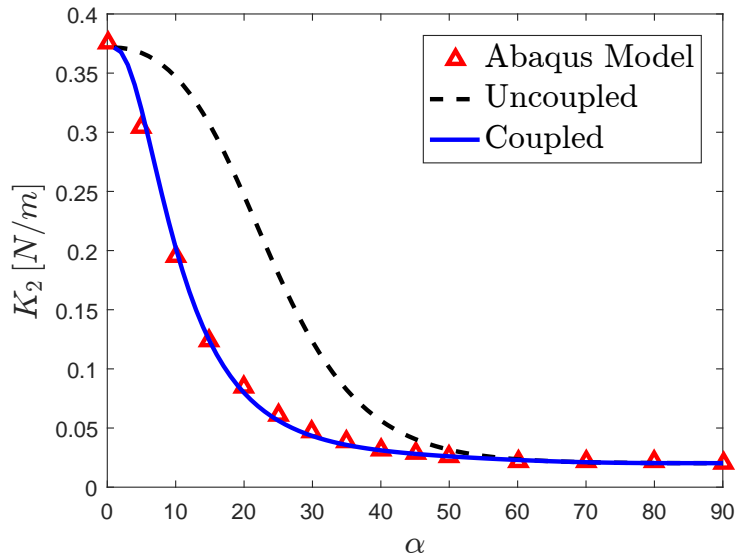


Figure 2.13:  $K_2$ , translational stiffness for an imposed nodal rotation

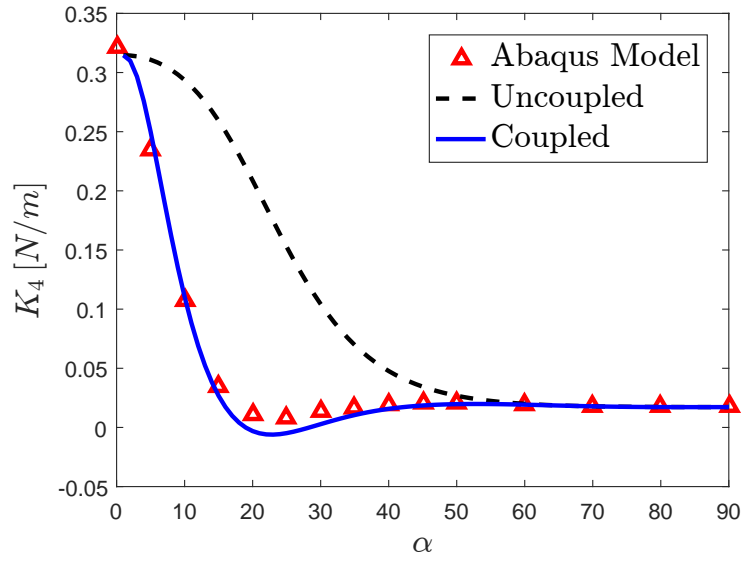


Figure 2.14:  $K_4$ , rotational stiffness for an imposed nodal rotation

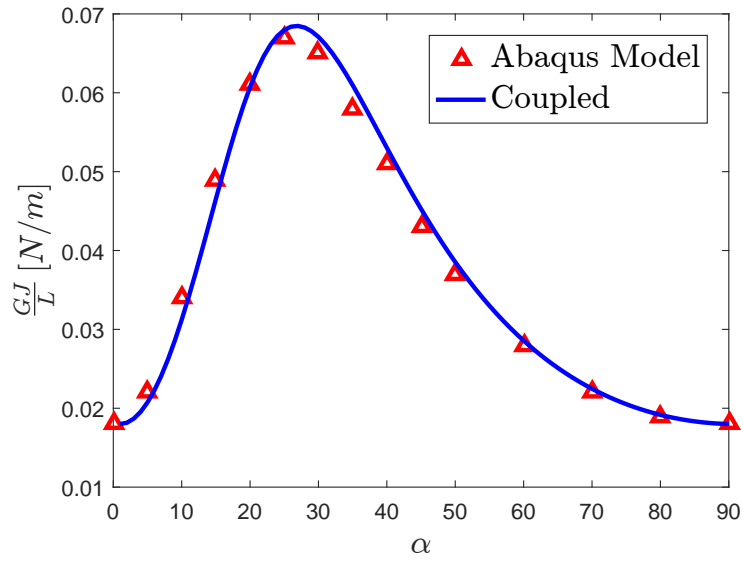


Figure 2.15:  $\frac{G_t J}{L}$ , torsional stiffness for an imposed nodal twist

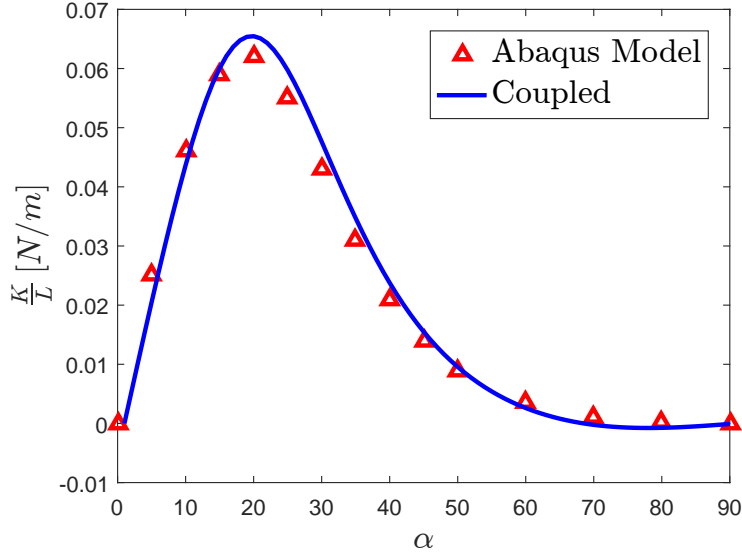


Figure 2.16:  $\frac{K}{L}$ , rotational stiffness for an imposed nodal twist

### 2.5.1.7 Sensitivity to the Coupling Parameter, $\Lambda$

It is important to the engineer to understand the role that bend-twist coupling plays in the structure and when the inclusion of the coupled relations are necessary to the analysis. Observing how the uncoupled and coupled stiffness terms vary in Equations (2.32-2.35), the difference is seen to be conditional on the ratio of  $\frac{K^2}{E_x I_y GJ}$ . The sensitivity ratio can be calculated directly from CLPT as all of the parameters are functions of  $D$  terms from the  $ABD$  matrix as the following:

$$\Lambda = \frac{\left(D_{16} - \frac{D_{12}D_{26}}{D_{22}}\right)^2}{\left(D_{11} - \frac{D_{12}^2}{D_{22}}\right) \left(D_{66} - \frac{D_{26}^2}{D_{22}}\right)}. \quad (2.36)$$

This ratio,  $\Lambda$ , serves as a nondimensional parameter that dictates how sensitive the laminate is to the coupling terms in the stiffness matrix. As shown in Figure 2.17, the ratio is conditional only on fiber angle and is significant for a large suite of unidirectional laminate

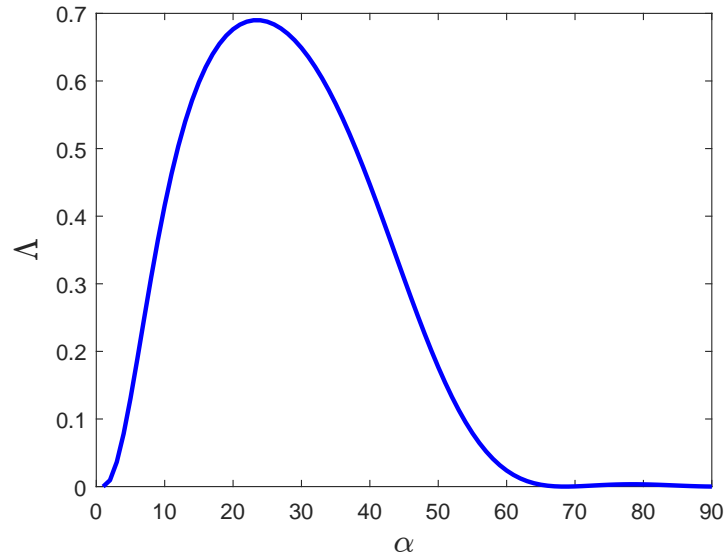


Figure 2.17: Sensitivity of laminate fiber angle to the difference between coupled and uncoupled stiffness matrix terms

fiber angles. For quasi-isotropic laminates or generally arbitrary layups, the sensitivity ratio can be calculated as a metric to aid in the design and analysis of coupled laminates. A ratio near zero suggests that uncoupled strain-displacement relations should be sufficiently accurate in analysis. However, the simplicity of the exact formulation leaves little need to avoid the completely coupled stiffness matrix.

### 2.5.1.8 Element Mass Matrix

One application already investigated is the use of the method for static analyses. The structural engineering community is very familiar with stiffness matrix assembly, making this method immediately available for their use. By utilizing discretization, the method is readily extendible for use with in-span loads. Additionally, through the use of rotation matrices, it is suitable for 3D frame analysis. The analysis could also be adapted into many existing nonlinear co-rotational methods for large deformations. This section will focus instead on dynamic analysis, as the stiffness matrix is immediately suitable for this application. The usefulness of the element stiffness matrix can be extended into the structural dynamics regime by formulating an element mass matrix.

Mass distribution for use in the stiffness matrix method can be established in a number of ways, including direct mass lumping or variational mass lumping. Following the variational mass lumping approach establishes the kinetic energy as,

$$T = \frac{1}{2} \rho \left[ A \left( \dot{w}_x^2 + \dot{w}_y^2 + \dot{w}_z^2 \right) + I_0 \dot{\theta}_x^2 \right], \quad (2.37)$$

where the dotted terms are the respective degree of freedom velocities,  $\rho$  is the material density,  $A$  is the cross-sectional area, and  $I_0 = I_y + I_z$  is the polar moment of inertia for the twisting body by the perpendicular axis theorem. The mass matrix can then be represented by the following integral,

$$\begin{aligned} \mathbf{M} = & \rho A \int_0^L (\mathbf{N}_A)^T \mathbf{N}_A dx \\ & + \rho A \int_0^L (\mathbf{N}_B)^T \mathbf{N}_B dx \\ & + \rho I_0 \int_0^L (\mathbf{N}_T)^T \mathbf{N}_T dx, \end{aligned} \quad (2.38)$$

where  $\mathbf{N}_A$ ,  $\mathbf{N}_B$ , and  $\mathbf{N}_T$  are shape function matrices containing the relevant shape functions for axial, bending, and torsion terms, respectively. For a consistent mass matrix, shape



functions for the mass matrix are the same as those for the stiffness matrix. However, only the shape functions corresponding to displacement equations for  $w_x, w_y, w_z$ , and  $\theta_x$  in Equations (2.11-2.14) are needed due to negligible  $\theta_y$  and  $\theta_z$  rotational inertia. Thus,  $\mathbf{N}_\mathbf{A}$  would contain the shape functions present in the first row of the shape function matrix in (2.39). Similarly,  $\mathbf{N}_\mathbf{B}$  corresponds to the shape functions included in the second and third rows of (2.39), while  $\mathbf{N}_\mathbf{T}$  contains shape functions present in the fourth row of (2.39). The resulting shape function matrix is 4x12 in dimension and results in a 12x12 consistent mass matrix.

The shape function matrix,  $\mathbf{N}$ , used to derive the consistent mass matrix,  $\mathbf{M}$ , is expressed as the following:

$$\mathbf{N} = \begin{bmatrix} N_{A1} & 0 & 0 & 0 & 0 & 0 & N_{A2} & 0 & 0 & 0 & 0 & 0 \\ 0 & N_{B1} & 0 & 0 & 0 & N_{R1} & 0 & N_{B2} & 0 & 0 & 0 & N_{R2} \\ 0 & 0 & N_{B1} & 0 & N_{R1} & 0 & 0 & 0 & N_{B2} & 0 & N_{R2} & 0 \\ 0 & 0 & \boxed{N_{\theta_x z_1}} & N_{T1} & \boxed{N_{\theta_x \theta_{y1}}} & 0 & 0 & 0 & \boxed{N_{\theta_x z_2}} & N_{T2} & \boxed{N_{\theta_x \theta_{y2}}} & 0 \end{bmatrix}, \quad (2.39)$$

where the boxed terms are the newly-derived shape functions. In a conventional, uncoupled, mass matrix derivation, these positions in the matrix would be zero.

The new expressions for coupled mass terms are as follows:

$$M_1 = \frac{13 A L \rho}{35} + \frac{6 I_0 K^2 \rho}{5 G J^2 L}, \quad (2.40)$$

$$M_2 = \frac{11 A L^2 \rho}{210} + \frac{3 I_0 K^2 \rho}{5 G J^2}, \quad (2.41)$$

$$M_3 = -\frac{11 A L^2 \rho}{210} + \frac{3 I_0 K^2 \rho}{5 G J^2}, \quad (2.42)$$

$$M_4 = \frac{A L^3 \rho}{105} + \frac{3 I_0 K^2 L \rho}{10 G J^2}, \quad (2.43)$$

$$M_5 = \frac{9 A L \rho}{70} - \frac{6 I_0 K^2 \rho}{5 G J^2 L}, \quad (2.44)$$

$$M_6 = -\frac{13 A L^2 \rho}{420} - \frac{3 I_0 K^2 \rho}{5 G J^2}, \quad (2.45)$$

$$M_7 = \frac{13 A L^2 \rho}{420} - \frac{3 I_0 K^2 \rho}{5 G J^2}, \quad (2.46)$$

$$M_8 = -\frac{A L^3 \rho}{140} - \frac{3 I_0 K^2 L \rho}{10 G J^2}. \quad (2.47)$$

The entire mass matrix can be presented as the following, where the boxed terms represent the terms expressed by Equations (2.40-2.47).

46

$$\mathbf{M} = \begin{bmatrix} \frac{A L \rho}{3} & 0 & 0 & 0 & 0 & 0 & \frac{A L \rho}{6} & 0 & 0 & 0 & 0 & 0 \\ 0 & \frac{13 A L \rho}{35} & 0 & 0 & 0 & \frac{11 A L^2 \rho}{210} & 0 & \frac{9 A L \rho}{70} & 0 & 0 & 0 & -\frac{13 A L^2 \rho}{420} \\ 0 & 0 & \boxed{M_1} & -\frac{I_0 K \rho}{2 G J} & \boxed{M_2} & 0 & 0 & 0 & \boxed{M_5} & -\frac{I_0 K \rho}{2 G J} & \boxed{M_6} & 0 \\ 0 & 0 & -\frac{I_0 K \rho}{2 G J} & \frac{I_0 L \rho}{3} & -\frac{I_0 K L \rho}{4 G J} & 0 & 0 & 0 & \frac{I_0 K \rho}{2 G J} & \frac{I_0 L \rho}{6} & \frac{I_0 K L \rho}{4 G J} & 0 \\ 0 & 0 & \boxed{M_2} & -\frac{I_0 K L \rho}{4 G J} & \boxed{M_4} & 0 & 0 & 0 & \boxed{M_7} & \frac{I_0 K L \rho}{4 G J} & \boxed{M_8} & 0 \\ 0 & \frac{11 A L^2 \rho}{210} & 0 & 0 & 0 & \frac{A L^3 \rho}{105} & 0 & \frac{13 A L^2 \rho}{420} & 0 & 0 & 0 & -\frac{A L^3 \rho}{140} \\ \frac{A L \rho}{6} & 0 & 0 & 0 & 0 & 0 & \frac{A L \rho}{3} & 0 & 0 & 0 & 0 & 0 \\ 0 & \frac{9 A L \rho}{70} & 0 & 0 & 0 & \frac{13 A L^2 \rho}{420} & 0 & \frac{13 A L \rho}{35} & 0 & 0 & 0 & -\frac{11 A L^2 \rho}{210} \\ 0 & 0 & \boxed{M_5} & \frac{I_0 K \rho}{2 G J} & \boxed{M_7} & 0 & 0 & 0 & \boxed{M_1} & \frac{I_0 K \rho}{2 G J} & \boxed{M_3} & 0 \\ 0 & 0 & -\frac{I_0 K \rho}{2 G J} & \frac{I_0 L \rho}{6} & -\frac{I_0 K L \rho}{4 G J} & 0 & 0 & 0 & \frac{I_0 K \rho}{2 G J} & \frac{I_0 L \rho}{3} & \frac{I_0 K L \rho}{4 G J} & 0 \\ 0 & 0 & \boxed{M_6} & \frac{I_0 K L \rho}{4 G J} & \boxed{M_8} & 0 & 0 & 0 & \boxed{M_3} & \frac{I_0 K L \rho}{4 G J} & \boxed{M_4} & 0 \\ 0 & -\frac{13 A L^2 \rho}{420} & 0 & 0 & 0 & -\frac{A L^3 \rho}{140} & 0 & -\frac{11 A L^2 \rho}{210} & 0 & 0 & 0 & \frac{A L^3 \rho}{105} \end{bmatrix}$$

### 2.5.1.9 Natural Frequency Calculation

Having established element mass and stiffness matrices, the system natural frequencies can be solved as a multiple degree of freedom linear dynamics eigenvalue problem. Solving the eigenvalue problem in Equation (2.48) yields the structural circular frequencies,  $\omega_n$ .

$$|\mathbf{K}_{\text{el}} - \omega_n^2 \mathbf{M}_{\text{el}}| = 0 \quad (2.48)$$

$$[\mathbf{K}_{\text{el}} - \omega_n^2 \mathbf{M}_{\text{el}}] \phi_{\mathbf{n}} = 0 \quad (2.49)$$

The mode shapes are the corresponding eigenvectors,  $\phi_{\mathbf{n}}$ , that satisfy Equation (2.49).

## 2.5.2 Exact Solution to Coupled Equations of Motion

The analytical solution for natural frequencies of bend-twist coupled cantilevers has been previously solved and given by many researchers but first notably by Banerjee in [21]. The work presented here most closely follows after Kramer's work on bend-twist coupling of composite laminates as in [19] which is also based off [21] but applied to composite laminates with the help of flexural, torsional, and coupling rigidities presented in [18]. This method will be denoted as the "coupled analytical solution" for the remainder of this thesis. The governing partial differential equations for a structural system under free vibration, ignoring structural damping, can be expressed as:

$$E_x I_y \frac{\partial^4 h}{\partial x^4} - K \frac{\partial^3 \phi}{\partial x^3} + m \frac{\partial^2 h}{\partial t^2} = 0, \quad (2.50)$$

$$GJ \frac{\partial^2 \phi}{\partial x^2} - K \frac{\partial^3 h}{\partial x^3} - I_x \frac{\partial^2 \phi}{\partial t^2} = 0, \quad (2.51)$$

where  $h = h(x, t)$  and  $\phi = \phi(x, t)$  are both functions of the longitudinal location of the beam as well as time. In these equations,  $E_x I_y$  is the bending stiffness parameter,  $GJ$  is the

torsional stiffness parameter,  $K$  is the bend-twist coupling parameter,  $m$  is the total mass per unit length, and  $I_x$  is the total polar mass moment of inertia per unit length about the x-axis.  $m$  and  $I_x$  can be expressed as:

$$m = \rho_s b t, \quad (2.52)$$

$$I_x = \rho_s \frac{b t (b^2 + t^2)}{12}, \quad (2.53)$$

where  $\rho_s$  is the solid density and  $b$  and  $t$  are the corresponding width and thickness of the beam.

The stiffness parameters  $E_x I_y$ ,  $GJ$ , and  $K$ , can be calculated following the work of [18] as:

$$E_x I_y = b \left( D_{11} - \frac{D_{12}^2}{D_{22}} \right), \quad (2.54)$$

$$GJ = 4b \left( D_{66} - \frac{D_{26}^2}{D_{22}} \right), \quad (2.55)$$

$$K = 2b \left( D_{16} - \frac{D_{12} D_{26}}{D_{22}} \right), \quad (2.56)$$

where the expressions for bending stiffness terms,  $D_{11}$ ,  $D_{12}$ ,  $D_{16}$ ,  $D_{22}$ ,  $D_{26}$ , and  $D_{66}$  are components of the laminate's  $ABD$  matrix. The  $ABD$  matrix values are dependent on material properties and lamina orientation as defined by CLPT.

Using separation of variables such that  $h(x, t) = H(x) e^{i\omega t}$  and  $\phi(x, t) = \Phi(x) e^{i\omega t}$  where  $\omega$  is the eigenfrequency, equations (2.50) and (2.51) can be rewritten in eigenformat as:

$$E_x I_y H^{(4)} - K \Phi^{(3)} - m \omega^2 H = 0, \quad (2.57)$$

$$GJ \Phi^{(2)} - K H^{(3)} + I_x \omega^2 \Phi = 0, \quad (2.58)$$

where  $f^{(n)} = \frac{d^n f}{dx^n}$  represents the  $n$ th spatial derivative of the function,  $f$ . Eliminating either

$H$  or  $\Phi$  from equations (2.57) and (2.58) yields a sixth-order differential equation:

$$W^{(6)} + \frac{I_x E_x I_y \omega^2}{E_x I_y GJ - K^2} W^{(4)} - \frac{m GJ \omega^2}{E_x I_y GJ - K^2} W^{(2)} - \frac{m I_x \omega^4}{E_x I_y GJ - K^2} W = 0, \quad (2.59)$$

where  $W = H$  or  $\Phi$ . A non-dimensional length  $\xi = x/L$  can be introduced as well as letting  $D = \frac{d(\cdot)}{d\xi}$ , such that (2.59) can be re-written as:

$$(D^6 + \bar{a} D^4 - \bar{b} D^2 - \bar{a} \bar{b} \bar{c}) W = 0, \quad (2.60)$$

where

$$\bar{a} = \frac{I_x E_x I_y \omega^2 L^2}{E_x I_y GJ - K^2}, \quad (2.61)$$

$$\bar{b} = \frac{m GJ \omega^2 L^4}{E_x I_y GJ - K^2}, \quad (2.62)$$

$$\bar{c} = 1 - \frac{K^2}{E_x I_y GJ}. \quad (2.63)$$

The general solutions of Equation (2.60) take the form:

$$\begin{aligned} H(\xi) = & A_1 \cosh(\alpha \xi) + A_2 \sinh(\alpha \xi) + A_3 \cos(\beta \xi) + A_4 \sin(\beta \xi) \\ & + A_5 \cos(\gamma \xi) + A_6 \sin(\gamma \xi), \end{aligned} \quad (2.64)$$

$$\begin{aligned} \Phi(\xi) = & B_1 \cosh(\alpha \xi) + B_2 \sinh(\alpha \xi) + B_3 \cos(\beta \xi) + B_4 \sin(\beta \xi) \\ & + B_5 \cos(\gamma \xi) + B_6 \sin(\gamma \xi), \end{aligned} \quad (2.65)$$

where

$$\alpha = \sqrt{2 \sqrt{\frac{q}{3}} \cos\left(\frac{\varphi}{3}\right) - \frac{\bar{a}}{3}}, \quad (2.66)$$

$$\beta = \sqrt{2 \sqrt{\frac{q}{3}} \cos\left(\frac{\pi - \varphi}{3}\right) + \frac{\bar{a}}{3}}, \quad (2.67)$$

$$\gamma = \sqrt{2 \sqrt{\frac{q}{3}} \cos\left(\frac{\pi + \varphi}{3}\right) + \frac{\bar{a}}{3}}, \quad (2.68)$$

$$q = \bar{b} + \frac{\bar{a}^2}{3}, \quad (2.69)$$

$$\varphi = \cos^{-1}\left[\frac{27\bar{a}\bar{b}\bar{c} - 9\bar{a}\bar{b} - 2\bar{a}^3}{2(\bar{a}^2 + 3\bar{b})^{3/2}}\right]. \quad (2.70)$$

The coefficients  $A_{1-6}$  and  $B_{1-6}$  are related by the relationship obtained by substituting Equations (2.64) and (2.65) into Equation (2.57), yielding:

$$B_1 = \frac{k_\alpha A_2}{L}, \quad (2.71)$$

$$B_2 = \frac{k_\alpha A_1}{L}, \quad (2.72)$$

$$B_3 = \frac{k_\beta A_4}{L}, \quad (2.73)$$

$$B_4 = -\frac{k_\beta A_3}{L}, \quad (2.74)$$

$$B_5 = \frac{k_\gamma A_6}{L}, \quad (2.75)$$

$$B_6 = -\frac{k_\gamma A_5}{L}, \quad (2.76)$$

where

$$k_\alpha = \frac{E_x I_y \alpha^4 - m \omega^2 L^4}{K \alpha^3}, \quad (2.77)$$

$$k_\beta = \frac{E_x I_y \beta^4 - m \omega^2 L^4}{K \beta^3}, \quad (2.78)$$

$$k_\gamma = \frac{E_x I_y \gamma^4 - m \omega^2 L^4}{K \gamma^3}. \quad (2.79)$$

Bending rotation  $\Theta(\xi)$ , bending moment  $M(\xi)$ , shear force  $S(\xi)$ , and torsional moment

$T(\xi)$  may be obtained from Equations (2.64) and (2.65) as:

$$\Theta(\xi) = \frac{1}{L} \frac{dH(\xi)}{d\xi} = \frac{1}{L} (A_1 \alpha \sinh \alpha \xi + A_2 \alpha \cosh \alpha \xi - A_3 \beta \sin \beta \xi + A_4 \beta \cos \beta \xi - A_5 \gamma \sin \gamma \xi + A_6 \gamma \cos \gamma \xi), \quad (2.80)$$

$$M(\xi) = -\frac{E_x I_y}{L^2} \frac{d^2 H(\xi)}{d\xi^2} = -\frac{E_x I_y}{L^2} (A_1 \alpha^2 \cosh \alpha \xi + A_2 \alpha^2 \sinh \alpha \xi - A_3 \beta^2 \cos \beta \xi - A_4 \beta^2 \sin \beta \xi - A_5 \gamma^2 \cos \gamma \xi - A_6 \gamma^2 \sin \gamma \xi), \quad (2.81)$$

$$S(\xi) = -\frac{1}{L} \frac{dM(\xi)}{d\xi} = \frac{E_x I_y}{L^3} (A_1 \alpha^3 \sinh \alpha \xi + A_2 \alpha^3 \cosh \alpha \xi + A_3 \beta^3 \sin \beta \xi - A_4 \beta^3 \cos \beta \xi + A_5 \gamma^3 \sin \gamma \xi - A_6 \gamma^3 \cos \gamma \xi), \quad (2.82)$$

$$T(\xi) = \frac{GJ}{L} \frac{d\Phi(\xi)}{d\xi} = \frac{GJ}{L^2} (A_1 \alpha k_\alpha \cosh \alpha \xi + A_2 \alpha k_\alpha \sinh \alpha \xi - A_3 \beta k_\beta \cos \beta \xi - A_4 \beta k_\beta \sin \beta \xi - A_5 \gamma k_\gamma \cos \gamma \xi - A_6 \gamma k_\gamma \sin \gamma \xi). \quad (2.83)$$

To derive the frequency equation, boundary conditions must be applied for the appropriate setting. In this case, cantilever setup results in the following boundary conditions:

$$H(0) = \Theta(0) = \Phi(0) = 0, \quad (2.84)$$

$$M(1) = S(1) = T(1) = 0. \quad (2.85)$$

By substituting Equations (2.64),(2.65),(2.80) - (2.83) into Equations (2.84) and (2.85), the following linear systems of equations is obtained:

$$\mathbf{BA} = \mathbf{0}, \quad (2.86)$$

where  $\mathbf{A} = [A_1, A_2, A_3, A_4, A_5, A_6]^T$  and  $\mathbf{B}$  takes the following form:



$$\begin{bmatrix} 1 & 0 & 1 & 0 & 1 & 0 \\ 0 & \alpha & 0 & \beta & 0 & \gamma \\ 0 & k_\alpha & 0 & k_\beta & 0 & k_\gamma \\ \alpha^2 C_{h\alpha} & \alpha^2 S_{h\alpha} & -\beta^2 C_\beta & -\beta^2 S_\beta & -\gamma^2 C_\gamma & -\gamma^2 S_\gamma \\ \alpha^3 S_{h\alpha} & \alpha^3 C_{h\alpha} & \beta^3 S_\beta & -\beta^3 C_\beta & \gamma^3 S_\gamma & -\gamma^3 C_\gamma \\ \alpha k_\alpha C_{h\alpha} & \alpha k_\alpha S_{h\alpha} & -\beta k_\beta C_\beta & -\beta k_\beta S_\beta & -\gamma k_\gamma C_\gamma & -\gamma k_\gamma S_\gamma \end{bmatrix},$$

where

$$\begin{aligned} C_{h\alpha} &= \cosh \alpha, & C_\beta &= \cos \beta, & C_\gamma &= \cos \gamma, \\ S_{h\alpha} &= \sinh \alpha, & S_\beta &= \sin \beta, & S_\gamma &= \sin \gamma. \end{aligned} \tag{2.87}$$

The necessary and sufficient condition for a non-zero solution to Equation (2.86) is  $\Delta = \det[\mathbf{B}] = 0$ , which yields the natural frequencies of the composite beam.

# Chapter 3

## Material Property Testing

### 3.1 Overview

When results from the finite element models were first compared with experimental results, the numerical models significantly over-predicted the stiffness of the beams, especially for the lower fiber angles of  $0^\circ$  and  $10^\circ$ . This suggested that the fiber-direction modulus, or  $E_1$  may not be accurate. For this reason, several experiments (tension testing, 3-point bending, cantilever bending) were conducted to characterize the elastic fiber-direction modulus of the material used in this research in order to have reasonable numbers to put in the model.

Unidirectional composite laminates with fibers oriented in the one principle laminate direction are inherently orthotropic. The transverse and out-of-plane elastic moduli are identical, however, and only conditional on the resin properties. Lamina and unidirectional laminates are typically characterized by four material properties, fiber-direction elastic modulus,  $E_1$ , resin-direction elastic modulus,  $E_2$ , in-plane shear modulus,  $G_{12}$ , and Poisson's ratio,  $\nu_{12}$ . For the tests conducted in this section, only  $E_1$  was of interest, as  $E_1$  contributes the most to the bending rigidity of the laminated beams.

Test specimens for these experiments came from existing beams as well as specimens

cured specifically for elastic modulus characterization. The newly-cured specimens included an 8-ply hot press cured plate, an 8-ply autoclave cured plate, and a 16-ply autoclave cured plate. Five beams were cut from each plate at varying locations from within the plate. The cut-templates for the autoclave beams can be seen from Figure 3.1 below. The motivation for choosing these specimens, specifically, were to investigate whether there were noticeable effects due to the following: cure methodology, thickness effects, location of beam cut from the plate. For each of the figures in the following sections, the bars represent individual beams, while the horizontal lines represent the mean measured value for all beams in the respective test.

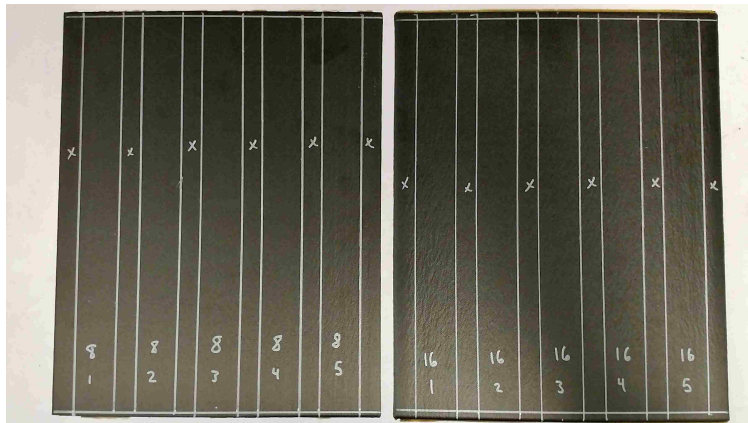


Figure 3.1: 8-ply and 16-ply autoclave plate specimen templates. Note that the specimens are labeled ‘1’-‘5’ from left to right.

## 3.2 Tension Testing

Tension tests were conducted on each beam in the UW CEE Construction Materials Lab on an Instron 600DX machine, with an Instron 2-inch gauge length extensometer measuring specimen displacements. Load-displacement data were processed in MATLAB to generate the stress-strain relation from which the effective modulus of elasticity could be calculated. Results for each beam are depicted in Figure 3.2. A note to the reader: the location ‘5’ 16-ply

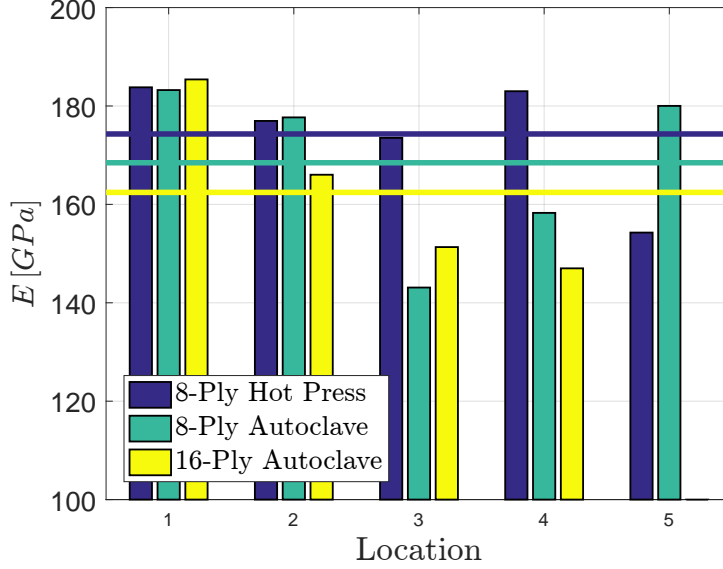


Figure 3.2: Tension test material characterization results

autoclave beam was broken before this test and could not be tested, hence the missing data point. It can be seen from Figure 3.2 that the 8-ply hot press specimens exhibit higher tested moduli than either the 8-ply autoclave beams or the 16-ply autoclave beams. The 8-ply hot press beam measured an average modulus of 174.31 GPa, while the 8-ply autoclave beams measured 168.46 GPa and the 16-ply autoclave beams averaged 162.44 GPa. Coefficients of variation for the tests were 6.9%, 10.2%, and 10.7%, respectively. The mean values are in the realm of expected values, however. Elastic modulus values obtained by the report in [15] averaged 162.1 GPa for 0 degree unidirectional beam specimens.

The difference in measured modulus across the width of the plate is significant, however. For the 16-ply autoclave specimens, the location ‘1’ beam measured nearly 40 GPa ( $\approx 25\%$ ) higher than the beam in the location ‘4’ position. While the difference between moduli for beams across the plate is significant, it is not immediately obvious whether there is an identifiable relationship between plate location and elastic modulus. It appears that beams



Figure 3.3: 3-point bending experimental setup

cut from the middle of the plate exhibit lower moduli, though the 16-ply autoclave ‘4’ location beam is even further decreased from the ‘3’ location. Similarly, the ‘5’ location 8-ply beam is lower than the ‘3’ location beam. This is left for future investigation.

### 3.3 3-Point Bending

A 3-point bending experiment was conducted in the UW Mechanical Engineering Building Instron 5585H machine. The test setup can be seen in Figure 3.3 below. Load and displacement values were recorded throughout the experiment and provided the data from which the effective modulus of elasticity could be calculated via a mechanics-of-materials approach where effective modulus,  $E$ , can be represented by the following expression,

$$E = \frac{P L^3}{48 \delta I}, \quad (3.1)$$

where  $P$  is applied load,  $L$  is beam length,  $\delta$  is mid-span deflection, and  $I$  is beam area moment of inertia. Results for each of the beams are depicted in Figure 3.4. The results of the 3-point bending experiment to characterize modulus of elasticity differ significantly from

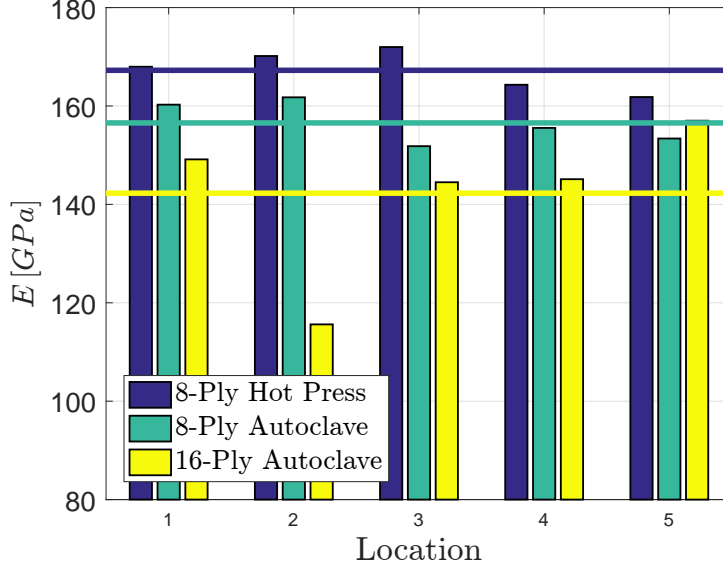


Figure 3.4: 3-point bending test material characterization results

those in the tension testing experiment. In general, the results are 10-20 GPa ( $\approx 4\% - 14\%$ ) lower across all specimens. The 8-ply hot press beams still have highest values, measuring an average of 167.25 GPa, while the 8-ply autoclave beams are lower, averaging 156.56 GPa, and the 16-ply autoclave specimens are again lowest at 142.28 GPa. Coefficients of variation were 2.5%, 2.8% and 3.4%, respectively. The largest variance again came from the 16-ply autoclave beams, but in a completely different order than captured by the tension tests. For instance, the difference in measured modulus between the tension test and the 3-point bending test for the location ‘2’ 16-ply beam is nearly 50 GPa ( $\approx 40\%$ ). As noted above, there is no obvious explanation for these variations and this is left for future investigation.

### 3.4 Cantilever Bending

A cantilever bending experiment was also conducted in the UW CEE Structural Dynamics lab following the same experimental setup as described in Chapter 2.3.1. The beams were

end-loaded with the same masses and had displacements recorded by the same microEpsilon laser sensor used in the Chapter 2.3.1 experiments. This provided the data from which the effective modulus of elasticity could be calculated via a mechanics-of-materials approach where effective modulus,  $E$ , can be represented by the following expression,

$$E = \frac{P L^3}{3 \delta I}, \quad (3.2)$$

where  $P$  is applied load,  $L$  is beam length,  $\delta$  is mid-span deflection, and  $I$  is beam area moment of inertia. Results for each beam are depicted in Figure 3.5. A note to the reader: by the time this test was conducted, the location ‘5’ 8-ply autoclave beam had broken as well as the location ‘4’ and ‘5’ 16-ply autoclave beams, hence the missing data points from this experiment. In this experiment, the average modulus for all beams were lower than averages for both the 3-point bending and the tension tests. The 8-ply autoclave beams showed highest modulus at 143.82 GPa, followed closely by the 8-ply hot pressed beams with 142.15

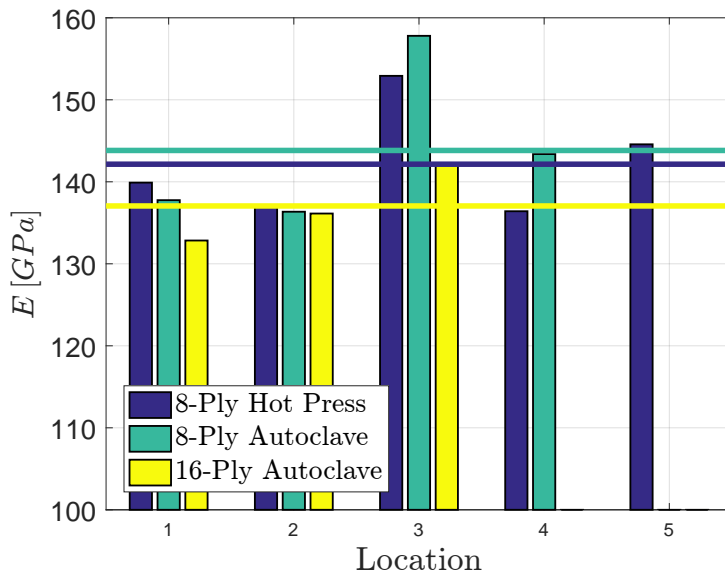


Figure 3.5: Cantilever bending test material characterization results

GPa, and lowest again were the 16-ply autoclave beams with an average modulus of 137.05 GPa. The coefficients of variation were 4.8%, 6.8%, and 3.3%, respectively. The variation in moduli with respect to beam specimen location differs yet again from the previous tests, though the maximum measured difference between tests isn't as drastic as in the 3-point bending experiment. The test is missing data from the broken beams, though. Despite the missing beams, no obvious trend between specimen location and modulus is apparent.

### 3.5 Steel Beam Modulus Testing

Due to the varying nature of the results both in beam specimen location and between experiments, it was questionable whether the nature of the experiment and calculation method would affect the resulting effective elastic modulus of a homogeneous, isotropic material such as steel. In order to test the effects of testing method on the resulting elastic modulus, three steel beams were cut from a thin steel plate. Each beam had two experiments conducted on it, a cantilevered free vibration ring-down, and a cantilever bending test, as a means to experimentally establish the elastic modulus for the material. The beams were identically sized to the composite beams in the previous sections and set up identically for the cantilever and free vibration tests. The free vibration was imposed in the same way as in Chapter 2.3.2, where an impulse was imparted on the free end, and the structure was left to ring-down, with the time-history displacement being recorded via laser sensor. With the response data, the natural frequency could be obtained. With the beam's natural frequencies, the bending stiffness can be backed out after solving the beam equation of motion which results in the following expression for natural frequency,

$$\omega_{nf} = \alpha_n^2 \sqrt{\frac{E_x I_y}{m L^4}}, \quad (3.3)$$



where  $\omega_{nf}$  refers to the natural circular frequency of the beam,  $\alpha_n$  corresponds to the vibrational mode constants, 1.875, in the case of the first mode,  $m$  is the linear mass density, and  $L$  is the beam length. The cross section is known, and thus the elastic modulus can be solved for. For the case of cantilever bending, the elastic modulus is solved identically to the previous section detailing the process for the composite beams.

The results for each steel beam and for each method can be seen in Table 3.1. The free vibration experiment yields an average elastic modulus of only 0.3 GPa ( $< 0.5\%$ ) higher than the cantilever bending experiment. The variance between specimens is higher than expected, however all values are within a reasonable range for the material and are very close when averaged. Listed values for structural steel elastic modulus range from 180 – 200 GPa. This experiment was conducted as a check to ensure that, for a well-characterized material, such as structural steel, the experimental results for elastic modulus do not vary drastically.

Beam	$E_{freevib}$ [GPa]	$E_{CL}$ [GPa]
1	182.8	178.9
2	176.9	189.9
3	190.1	180.1
<b>Mean</b>	<b>183.3</b>	<b>183.0</b>

Table 3.1: Elastic modulus averages between experiments for steel beams

## 3.6 Results and Discussion

Overall, there is drastic difference in elastic moduli between cure methods, specimen thicknesses, and specimen location in the laminate. The general trend for them is that the hot-pressed beams were stiffer than either of the autoclaved beams. The thicker 16-ply specimens always averaged lower values than either of the 8-ply specimens in each test. Tension tests yielded highest values for the effective modulus, while 3-point bending provided intermediate values, and cantilever bending tests resulted in the lowest measured values. The

values from the tension tests aligned most closely with values presented in [15], but the test in that reference was also a tension coupon test, which is then sensible. It is not clear, however, why the different experiments such different values. Comparing the experimentally characterized values for the structural steel, it can be seen that the averages are very close between the two methods. However, both free vibration and cantilever bending had cantilever boundary conditions, while the three experiments conducted on the composites each had unique boundary conditions.

Looking at the averages for each composite beam set for each test in Table 3.2, the differences between experimental method results are clearly visible. The mean values for each set of experiments are presented in the bottom row, averaging out the effects of cure method and laminate thickness. The table shows that moduli calculated by cantilever bending method result in values nearly 17 GPa less ( $\approx 12\%$ ) than by 3-point bending, and 27 GPa ( $\approx 19\%$ ) less than by tensile testing.

A colleague at the University of New Mexico also worked with the same material donated by the Air Force Research Labs in some of her experimental structural mechanics of carbon fiber laminates research. In her thesis [22],  $E_1$  for the IM7/8552 material was measured to be 122.2 GPa with a Poisson’s ratio of 0.27, measured by strain gauge. This test was conducted as a tensile test and it is curious why the results are 46 GPa ( $\approx 38\%$ ) lower than the measured values conducted in this work.

At this stage, the inherent variability of the material suggested to the researcher to move forward with the  $E_1$  value associated with the boundary condition most representative of

Beam	$E_{tension}$ [GPa]	$E_{3Pt}$ [GPa]	$E_{cantilever}$ [GPa]
Hot press 8-ply	174.3	167.2	142.2
Autoclave 8-ply	168.5	156.6	143.8
Autoclave 16-ply	162.4	149.5	137.1
<b>Mean</b>	<b>168.4</b>	<b>157.8</b>	<b>141.0</b>

Table 3.2: Elastic modulus averages between experiments for composite beams

applications of bend-twist composite beams, the cantilever. This was deemed an appropriate “effective” material property for the boundary conditions in the experiments. The material properties which were decidedly used in the finite element models of the experiments can be seen in Table 3.3. The remaining properties came from reported values in [15].

$E_1$ [GPa]	$E_2$ [GPa]	$\nu_{12}$	$G_{12}$ [GPa]	$G_{13}$ [GPa]	$G_{23}$ [GPa]
141.0	8.96	0.316	4.69	4.69	3.09

Table 3.3: Material properties for finite element models of experiments

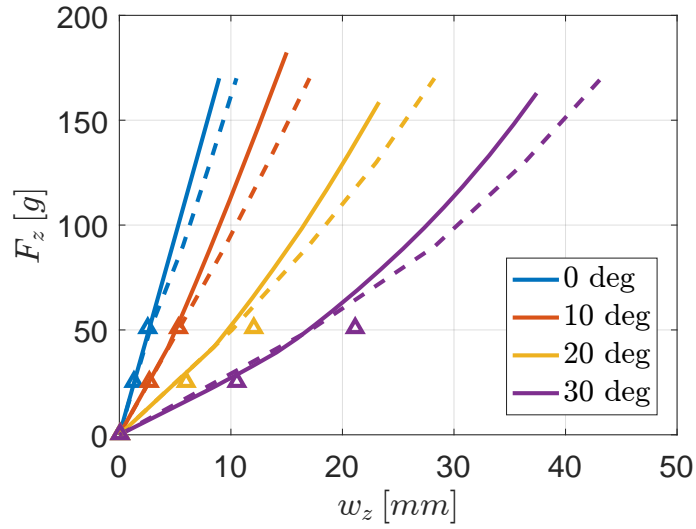
# Chapter 4

## Comparison of Results

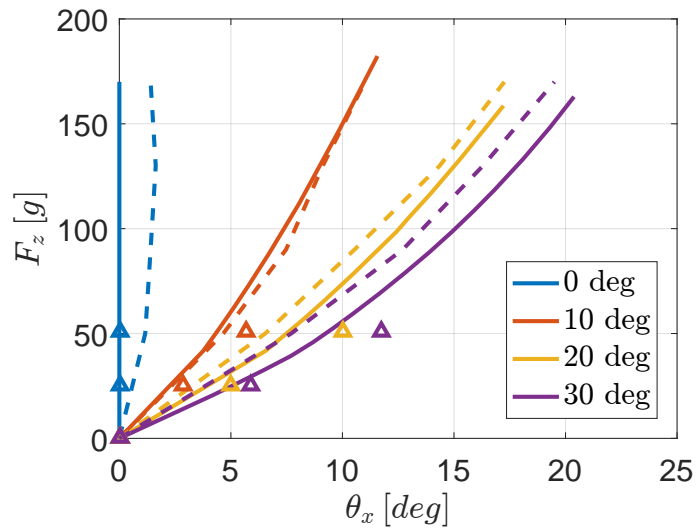
### 4.1 Static Force-Deflection

The force-deflection and force-twist responses of bend-twist coupled cantilever beams can be characterized experimentally, analytically via stiffness matrix method, and by ABAQUS finite element analysis. The results from the analyses are compared in Figure 4.1. The solid lines represent the ABAQUS numerical simulations, while the dashed lines illustrate the experimental results. The triangular markers correspond to the SMM results for the first two load cases. The SMM analysis was not conducted for the whole suite of loadings due to the high degree of geometric nonlinearity achieved in the experiments as the validity of the SMM is limited to the geometrically linear domain.

Despite efforts to appropriately characterize the fiber-direction modulus of the composite, it is still evident in the results that the material properties are not completely correct. For every beam, the experimental results are more flexible and exhibit larger deflections than the ABAQUS numerical models in the force-deflection relationship. The difference in deflection magnitude between experiment data and numerical simulation increases as the deflections increase. The opposite can be observed in the force-twist relationship. The numerical models



(a) Force-deflection



(b) Force-twist

Figure 4.1: Comparison of analytical, FEM, and experimental results for load-deformation characterization. Solid lines represent the ABAQUS numerical simulations, while dashed lines illustrate experimental results, and the triangular markers correspond to the SMM results for the first two load cases.

over-estimate the beam twist compared to the measured values in the experiment, specifically for the 20° and 30° beams. In characterizing force-deflection and force-twist relationships, the SMM model approximates well for the smallest load cases. Beyond about 30 grams of loading, the beam experiences enough bending to be significantly geometrically nonlinear. The geometric nonlinearity is easily observed in the stiffening force-deflection and force-twist curves for the numerical and experimental cases.

Additionally, imperfections can be observed in the experimental data for the 0° beam force-twist relationship. The dashed curve should remain vertical, indicating no twist, however, there is a slight deviation, suggesting that the loading was not coincident with the shear center, or that the fiber angle was not, indeed, 0°. Nonetheless, both the numerical model and the SMM model provide a reasonable rough approximation of the deflection state for all beams.

## 4.2 Linear Vibration

Small amplitude dynamics were investigated robustly for the suite of beams. Both free vibration and frequency sweep experiments were conducted, which exposed first natural bending frequencies for each beam. The frequency sweep was conducted at higher frequencies as well to experimentally establish second natural bending frequencies. The second bending mode and first twisting mode were not able to be recovered from the free vibration experiment due to the beams' preference to vibrate in the first mode when plucked manually and left to ring down. The vibrations did not contain enough second bending mode or first twisting mode content to meaningfully show up in the frequency spectrum after performing the Fast Fourier Transform. Each experiment and set of analyses was conducted on beams manufactured both by autoclave and by hot-press. Because the results are nominally identical and for the sake of brevity, only the results for the hot-pressed beams are presented in this work.

For linear dynamics, multiple methods are available for analysis and characterization. Both analytical formulations as well as the ABAQUS FEM presented in Chapter 2.4-2.5 can be utilized to evaluate the structure's dynamic response. In this section and the following figures, "CAS" refers to "coupled analytical solution," or the exact solution to the coupled equations of motion presented in Chapter 2.5.2. "SMM" again refers to the "stiffness matrix method" also presented in Chapter 2.5.1. In this case, the "SMM" is a 20-element mesh in order to be sufficiently accurate. The convergence of the model due to mesh refinement is also covered in Chapter 2.5.1.

In Figure 4.2, the results for the first bending natural frequency are presented. There is a slight difference between the experimentally characterized values with the free vibration natural frequency being consistently higher than those corresponding to the frequency sweep. Similarly, the ABAQUS numerical predictions are consistently higher than predictions by either analytical method. The predictions between the two analytical methods are consistently close. All of the predictive methods approximate the first bending frequency within several Hertz, but none are consistently very close across all beams of multiple fiber angles.

Figure 4.3 depicts the results for the 2nd bending natural frequency established by the frequency sweep experiment and the predictive methods. Once again, the predictive methods approximate the natural frequency within a reasonable range of frequencies, however none of them are consistently very close to the experimentally characterized frequency. The ABAQUS approximations are consistently higher than the analytical methods, while the results seem to converge towards a common value as the fiber angle of the beams increases. This is to be expected due to the reduction in coupling intensity at fiber angles beyond about  $10^\circ$ .

First twisting natural frequencies are compared and presented in Figure 4.4. There was no experiment that could capture any twisting frequencies, hence only the predictive methods are presented. Results are consistent with other modes, with the ABAQUS approximation

being consistently higher than the analytical methods, but converging towards a common value at the higher fiber angles.

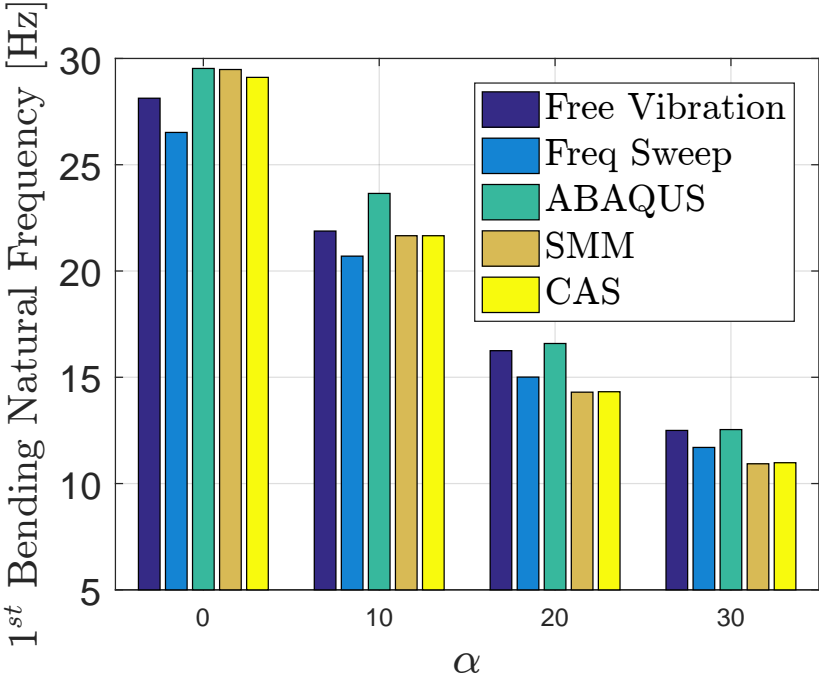


Figure 4.2: Comparison of first bending natural frequencies for various experimental and predictive methods



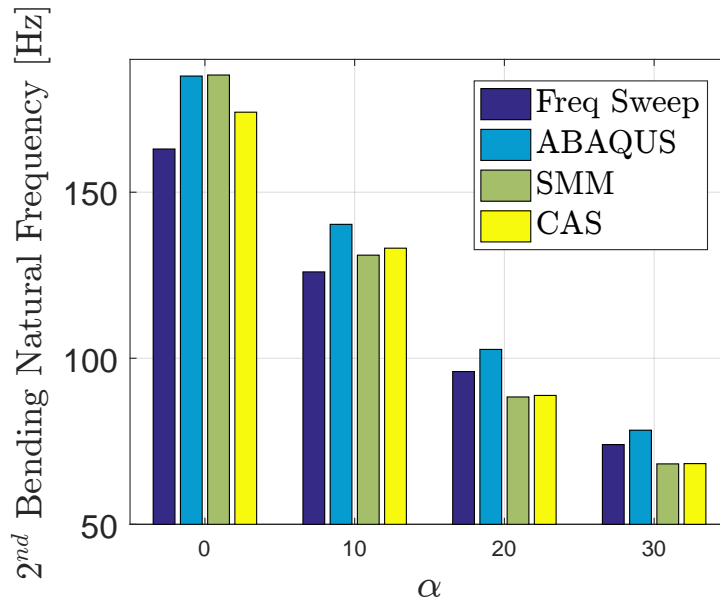


Figure 4.3: Comparison of second bending natural frequencies for experimental and predictive methods

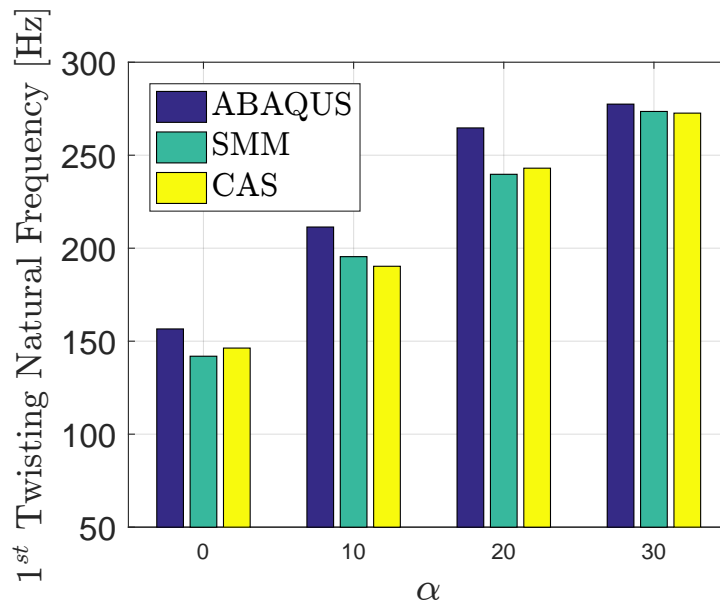


Figure 4.4: Comparison of first twisting natural frequencies for predictive methods

### 4.3 Large Amplitude Vibration

Large amplitude vibration was investigated in order to determine whether or not geometric nonlinearity would affect the structure's natural frequencies. In order to determine whether or not a composite cantilever is sensitive to frequency stiffening or frequency softening under large vibrations, the specimens were subjected to base excitation accelerations of 1G, 5G, 10G, and, for the 0° beam, 20G. As the excitation acceleration increased, the beam displacements increased significantly, well into the geometrically nonlinear realm. Figure 4.5 shows the difference in displacements for each beam when subjected to 1G and 10G accelerations. The top subfigure refers to the 0° beam, with increasing fiber angle (10° and 20°) for each successive subfigure until the 30° beam at the bottom. An order of magnitude increase in forcing essentially doubles the beam displacements.

It can be seen from Figure 4.6, however, that the respective natural frequencies for each beam under the increasing loading remains essentially unchanged. The beams were simply too light to incite any frequency stiffening due to the catenary tensions associated with the geometric nonlinearity. Furthermore, cantilever boundary conditions may not be restrictive enough to induce any axial effects during vibration (unlike clamped-clamped systems).

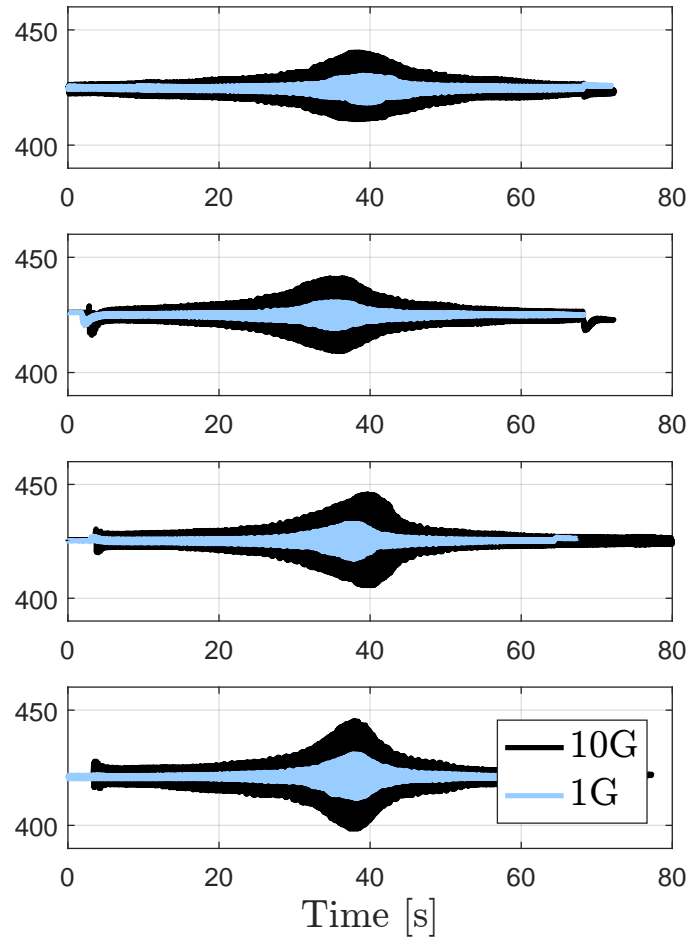


Figure 4.5: Time history of frequency sweep experiment with varying excitation accelerations

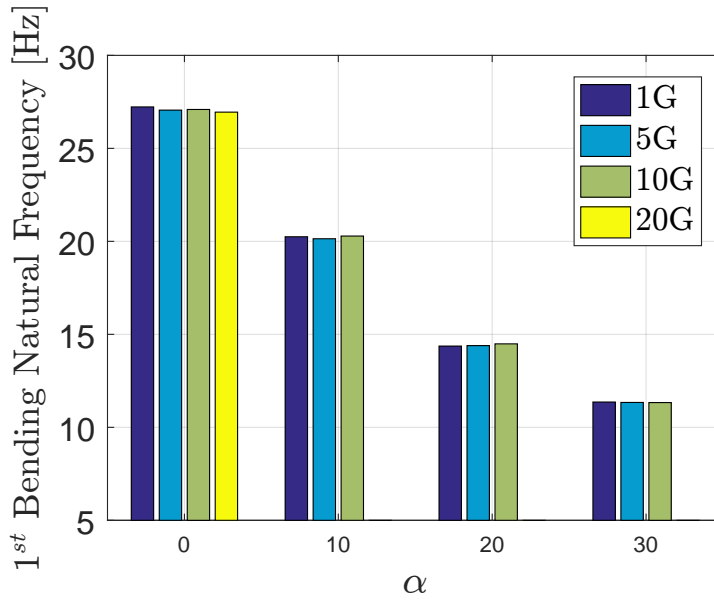


Figure 4.6: Comparison of first bending natural frequencies for increasing excitation accelerations

## 4.4 Discussion of Results

There are several notable takeaways when comparing the experimental results with predictive methods for the structural response of bend-twist coupled cantilever beams. First, the material properties have a very significant effect on beam response. Even after characterizing the fiber-direction modulus of the beams in Chapter 3.6, the experimental results still differed when compared to the model predictions. The material may require further testing to appropriately establish resin and shear moduli. Additionally, the material properties vary from beam to beam, even when cut from the same laminate, which makes the predictions even more difficult.

Secondly, the ABAQUS FEM consistently over-predicts stiffness of the beams in both the static and dynamic load cases, specifically when compared to the analytical methods. This may be due to how ABAQUS calculates effective laminate properties, conducts the

frequency analysis, or any number of other factors, inherent to the finite element method. Generally, though, all of the analysis methods provide reasonable estimates for predicting structural response of such beams, yet none of them match the experimental results exactly or consistently.

Lastly, natural frequencies established experimentally differ based on the method of experimentation. This is unusual behavior, especially when the frequencies differ by several Hertz. Boundary conditions and experimental setup could all contribute to the difference in observed natural frequencies. It is most important to ensure that material properties are established appropriately and that the laminate fiber angle is accurate. Material properties contribute greatly to the overall beam stiffness, and the coupling sensitivity is highly dependent on fiber angle for beams with significant coupling. Therefore, if the beams were cut from the laminate at an angle which differed slightly from the target fiber angle, the results could differ significantly.

# Chapter 5

## Applications of Bend-Twist Coupled Composites

### 5.1 General Applications

#### 5.1.1 Aircraft Wings

Bend-twist coupling made its aerospace debut in the Grumman X-29 experimental aircraft, an aircraft commissioned by NASA and the US Air Force to investigate the effects of forward swept wings, canard control surfaces, and other novel technologies on aircraft performance. The forward swept wings are problematic under strong lift conditions due to the ever-increasing angle-of-attack associated with such geometry. Lift created by the wing induces wing bending, accompanied by a pitching effect due to the forward sweeping. The wings pitch to stall under load, increasing the angle-of-attack, thus increasing the lift on the wing further, until the wing experiences either a stall condition or a total structural failure associated with the diverging wing deflections. Mitigating this would require a wing that is, torsionally, extremely rigid. However, increasing the rigidity of the wing so much would

increase mass and neglect the performance advantages associated with the design. The engineers decided to implement symmetric, unbalanced composite laminates in the skin of the wing to counteract the divergent pitch-to-stall characteristics with the inclusion of bend-twist coupling. The wings could deflect, but the bend-twist coupling of the composite skins would limit the twisting of the wing to maintain appropriate angles-of-attack. Similar technologies were incorporated by Russian engineers with the forward swept-wing aircraft, Sukhoi Su-47. Tip divergence in the Russian aircraft was mitigated with the same bend-twist coupled composite skins in the aircraft wings. These aircraft were successful in demonstrating the technology, however did not transition into production.



(a) Grumman X-29



(b) Sukhoi Su-47

Figure 5.1: Experimental fighter jets which used bend-twist coupling in their wing skins from [23] and [24]

Although bend-twist coupling has been investigated in experimental aircraft, limited progress has been made including the structural phenomena outside of the experimental regime. Recently, however, the inclusion of bend-twist coupling in commercial aircraft wings to mitigate effects of gust loading was investigated as by Perron in [8]. Perron showed that bend-twist coupling could help reduce the peak spanwise bending moments by up to 45% and aid in weight savings up to 4% on larger commercial aircraft such as the Boeing 777.

### 5.1.2 Wind Turbine Blades

Bend-twist coupling has been in the wind turbine research community for several decades. Aeroelastic tailoring has been viewed as a cost-effective, passive means to shape the power

curve and reduce loads. The functionality of the bend-twist mechanism is the same as in aircraft wings, where the composite is used to designate the angle-of-attack as the blade experiences load. In the context of wind turbine blades, the aeroelastic tailoring is typically included to regulate power or speed in high winds. It has long been a subject of investigation by the Department of Energy's, Sandia National Labs, which has produced extensive documentation on the subject, as in [4], [3], and [25]. Researchers in Denmark and Sweden have also investigated and modeled the bend-twist coupling effects in wind turbine blades in [26] and [20]. Within the existing research, the goal is primarily to accurately model the structural response of the blades and tailor their performance to a loading or design condition. The literature corresponding to modeling and designing bend-twist coupled wind turbine blades is fairly robust.

### **5.1.3 Marine/Tidal Turbine Blades**

Newer to the bend-twist coupling community is the adaptation of the coupling mechanism into tidal turbine blades. Tidal (or marine) turbines are analogous to wind turbines, however, they rely on the flow of water past the turbine for energy generation. Marine turbines are typically placed in energy-dense regions, such as inlets or harbors, where the tidal flows are significant.

The loading environments of marine turbine blades can be harsher and more variable than those corresponding to wind-turbine blades. Water is heavy, incompressible, corrosive, and difficult to work in. Theoretically, bend-twist coupling should be equally as useful in a marine environment to tailor the blade response to the loading condition. As far as application, however, nearly all marine turbine blades rely on active pitch control to vary the angle-of-attack of the turbine blades to shed loads under off-design flow conditions. Passive pitch adaptation using bend-twist coupling can allow for instant angle-of-attack adjustment to varying flow conditions without reliance on motors and mechanisms providing active





Figure 5.2: Marine/tidal turbine examples

control. Researchers have written about and modeled applications of bend-twist coupled blades for horizontal axis tidal turbines in [10], [6], [7], and [27], though it has not been implemented into full-scale application to date.

## 5.2 Bend-Twist Coupling for Passively Adaptive Tidal Turbine Blades

### 5.2.1 Motivation

While the use of adaptive marine turbine blades has been thoroughly explored numerically, little experimental work has been accomplished to date. In order to validate and support continuing numerical studies of the adaptive blades, it is necessary to provide baseline experimental data on these systems. The work in this section presents the design, analysis, manufacture, testing, and experimentation of three sets of flume-scale turbine blades. An experimental program was conducted to investigate the mechanics of adaptive pitch blades

and the impact these blades have on the performance of a marine turbine system. The performances of two sets of adaptive composite blades were compared to that of a neutral pitch blade design. One adaptive set was designed to pitch to stall, or twist such that the angle of attack increases with loading, while the other set was designed to pitch to feather, or decrease the angle of attack. Turbine level performance characteristics were predicted to differ based on which direction the blades pitched, therefore two sets of pitching blades were required.

### 5.2.2 Design of Flume-Scale Turbine Blades

All blades discussed in this work were designed to identical geometric parameters; the tailored bend-twist mechanism in the adaptive models was created solely by the coupling induced at the material level. The blade geometry was provided by corresponding researchers from the University of Washington's Marine Energy Group in the Mechanical Engineering Department. Blade geometry was determined using an optimization routine in HARP\_Opt (Horizontal Axis Rotor Performance Optimization) code developed by the National Renewable Energy Laboratory (NREL). Details concerning the exact blade geometry and its development can be found in [5]. Because the blades were designed for use in an experimental flume, they were significantly reduced in size from actual production marine turbine blades. Each blade was roughly 170 mm long, 30 mm wide, and 10 mm thick at the root. The general blade profile and female mold provided by the Marine Energy Group can be seen in Figure 5.3.

Due to the small scale of the blades required for flume-level testing, it was not feasible to lay up an adaptive composite laminate following the complex blade geometry with sufficient accuracy in either the geometry or the fiber orientation. To address this issue, the composite blades were composed of a flat carbon fiber spar, twisted to follow the chord line of the target blade geometry, and a semi-flexible urethane body cast around the spar to create the



Figure 5.3: Machined aluminum mold of flume-scale blade geometry

hydrodynamic blade shape. Tooling for the chord line down the blade was designed and machined as a surface on which to lay up the spars and can be seen in Figure 5.4. The urethane was chosen such that it had adequate hardness to maintain the blade geometry but would not impede the elastic bend-twist deformations. In this way, the adaptive tailoring of the composites could be explicitly controlled in the carbon fiber spar without sacrificing accuracy in the hydrodynamic profile. This fabrication process was used solely for the small-scale blades in this test sequence and experimentation; future work on larger blades will require the use of more traditional manufacturing processes.

Because the geometry was pre-established, design goals for the blades corresponded

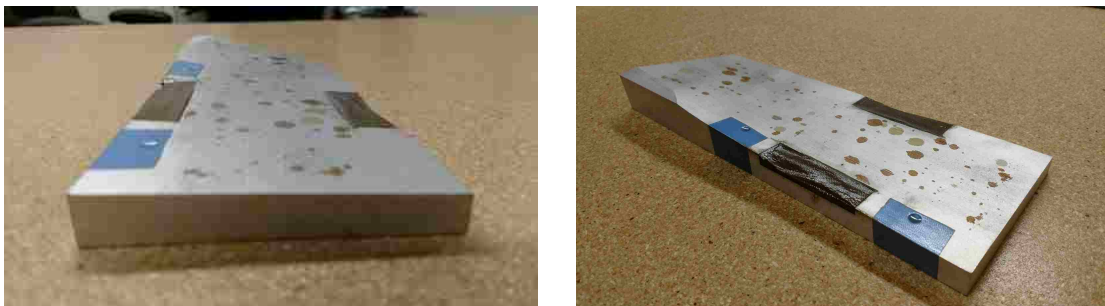


Figure 5.4: Machined aluminum tooling of twisted chord line for spar manufacture

mostly to the deflection targets thought to yield meaningful differences in turbine-level performance. A target pitch change ( $\pm 5^\circ$ ) and a limit on bending deflection (10% of the blade length, or  $\approx 17$  mm) at the design condition were imposed, along with constraints based on the predefined geometry.

### 5.2.3 Analysis of Composite Spars

The experimental flume has a fluid velocity range of 0.5 m/s - 1.2 m/s. The turbine was tuned for performance at a fluid velocity around 0.85 m/s. From the blade geometry, the coefficient of thrust could be estimated to be between 0.65 – 0.85 (information provided by UW Mechanical Engineering). With this information, the thrust per blade could be calculated via the following equation,

$$T = \frac{1}{2n} \rho V^2 A C_t, \quad (5.1)$$

where  $T$  is the blade thrust,  $\rho$  is the fluid density,  $V$  is the fluid velocity,  $C_t$  is the coefficient of thrust,  $n$  is the number of blades, and  $A$  is the swept area of the turbine. Using the upper and lower bounds on the coefficient of thrust and flow velocity estimates gave a range of expected blade thrusts. Given that the geometry of the blades was already provided, the thrusts could be divided by the blade area to give an estimated range of pressures that the blades would experience in the flume. This calculation set the basis for the analysis and design of the composite spars.

To design the appropriate composite laminate spars for the adaptive blades, a parametric study in ABAQUS/Standard was conducted. Each spar was designed to be cut from an off-angle unidirectional laminate plate. Designing for both twist and deflection gave a two-variable parameter space, where fiber angle, and number of plies could be varied to meet target twist and deflection goals stated earlier. The material to be used in manufacturing the spars was consistent with the experimental beams from Chapter 2, more specifically the

donated Hexcel IM7/8552 carbon fiber. At this stage, some of the experimentation from Chapters 2 and 3 had not yet been conducted, therefore the material properties used in analysis were consistent with those provided by the manufacturer rather than deduced by experimentation as in Chapter 3.6.

The resulting laminates each consisted of 14 plies, resulting in a final spar thickness of 1.43 mm. All plies for the adaptive blades were laid up with a  $7^\circ$  fiber angle offset from the blade axis:  $+7^\circ$  for the pitch to feather blades and  $-7^\circ$  for the pitch to stall blades. The neutral composite blades were also 14 ply, with the unidirectional fiber angles aligned with the blade longitudinal axis(i.e.  $0^\circ$ ). The fiber angle offset required for the creation of an adaptive mechanism will always result in a reduced stiffness compared to the neutral,  $0^\circ$ , orientation, however all deflections were within the acceptable range. Properties of all three materials used are shown in Table 5.1.

Aluminum	Compound: 6061-T6 $\rho = 2700 \text{ kg/m}^3$ $E = 68.9 \text{ GPa}$ $G = 26 \text{ GPa}$ $\nu = 0.33$
Carbon Fiber Laminate	Compound: Hexcel IM7/8552 $\rho = 1570 \text{ kg/m}^3$ $E_1 = 158 \text{ GPa}, E_2 = E_3 = 8.96 \text{ GPa}$ $G_{12} = G_{13} = 4.69 \text{ GPa}, G_{23} = 3.09 \text{ GPa}$ $\nu_{12} = \nu_{13} = 0.316, \nu_{23} = 0.451$
Urethane	Compound: Smooth-Cast 45D $\rho = 1100 \text{ kg/m}^3$ Shore Hardness: 45D Elongation at Break: 100%

Table 5.1: Blade material properties

## 5.2.4 Manufacture of Experimental Blades

Manufacturing the flume-scale turbine blades required construction over the course of several steps. First, all the spar laminates needed to be laid up and cured via autoclave. Details of the autoclave curing process can be found in Appendix A.1 of this work. Once cured, the spars could be cut from the laminates by Dremel and then tailored to the precise designed shape. An example of this can be seen in Figure 5.5. Next, a machined aluminum piece had to be epoxied to the base of each spar in order to interface with the turbine hub, as seen in Figure 5.6.



(a) Autoclave-cured laminates used for composite spar



(b) Spar cut by Dremel from cured laminates

Figure 5.5: Cured laminate vs. finished spar shape



Figure 5.6: Close-up of machined aluminum insert being epoxied to spar

The spar and interface piece could then be placed and clamped in the mold in order to have the urethane poured around it. Finally, the urethane was mixed and poured around the spar and let to cure before it could be removed from the mold to yield the finished, cured part. Once complete, the leading and trailing edges of the blade could be cleaned up manually and checked for defects. In total, 14 blades were produced for use in the experiment, as seen in Figure 5.7. The three sets only required 9 blades, however some extras were manufactured for redundancy and in case of breakage or fitment issues.



Figure 5.7: Finished blades with flexible urethane poured over the spars

### 5.2.5 Load-Deflection Experiment and Structural Qualification

Load-deformation testing on the turbine blades was performed in the structural vibrations laboratory at the University of Washington. The blades were mounted to the turbine hub while the entire turbine was affixed to one of the work benches. Each blade was then loaded quasi-statically in the streamwise direction (see Figure 5.8; negative  $BF_Y$  direction) using a displacement-controlled method in which a slowly incrementing displacement was applied to the blade tip at the neutral pitch axis. Two lasers, a Micro-Epsilon optoNCDT 2300-20 and a Micro-Epsilon optoNCDT 1700-500, were used to measure deflection of the blades under load. The lasers each captured “streamwise” deflection 163 mm from the blade root

at points separated by 14.7 mm along the chord of the blade, as depicted in Figure 5.9. Each individual blade was mounted on a load cell which was connected to the turbine for the test. The load cell was a six-axis ATI Industrial Automation Nano25, and was used to record forces and moments corresponding to the applied displacement. Measurements from the two lasers and the load cell were synchronized in order to calculate force-deflection, force-twist, and deflection-twist relationships.

Static load-deformation tests were conducted in order to quantify the force-deformation relationships of the three composite blade sets as well as one “rigid” aluminum blade set in response to a single point load. The aluminum blade set served as an effectively rigid control set for comparison to the flexible and adaptive composite blades in the flume experiment, the details of which are explained in the following section. Though, in practice, the loading

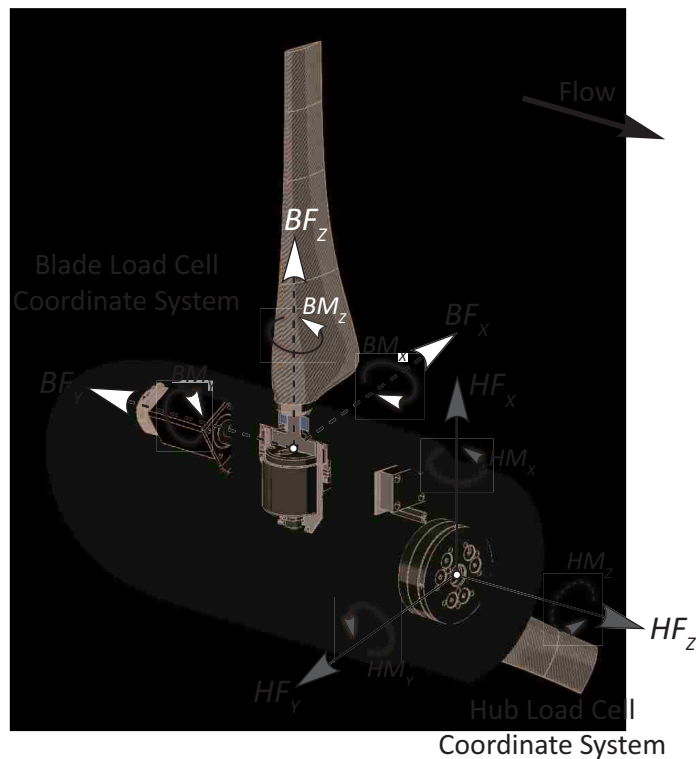


Figure 5.8: Schematic of the blade ( $BF_{xyz}, BM_{xyz}$ ) and hub ( $HF_{xyz}, HM_{xyz}$ ) load cell coordinate systems.



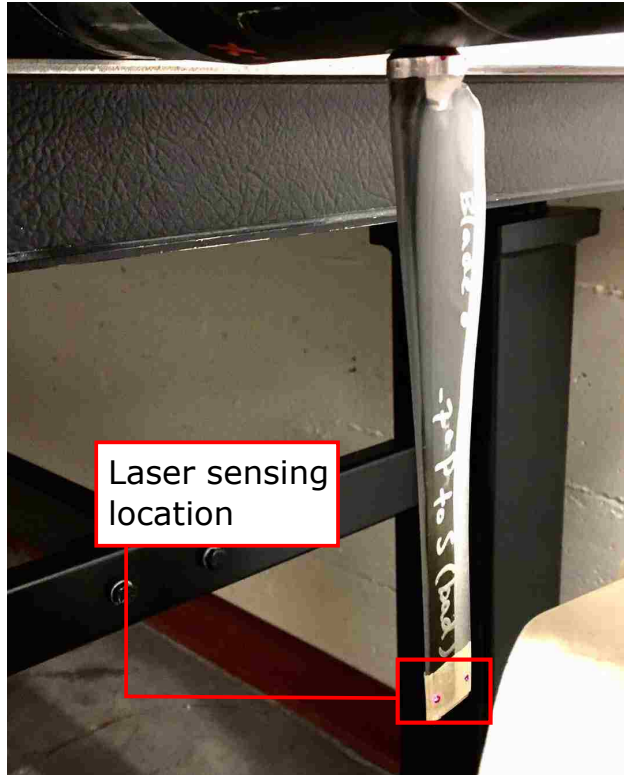


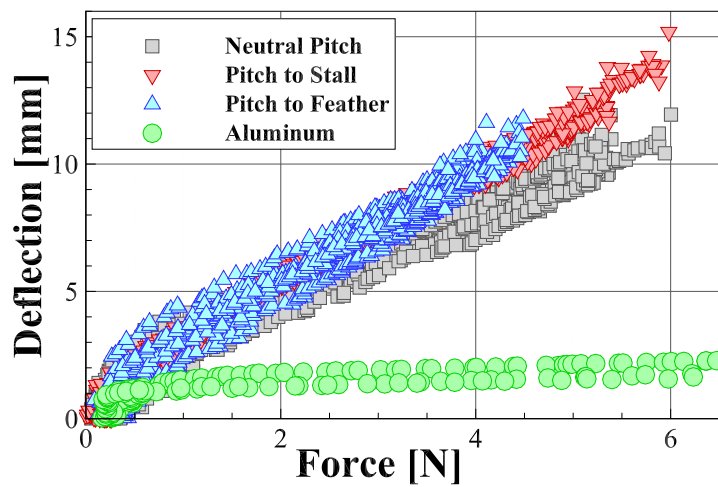
Figure 5.9: Placement of laser sensors on turbine blade for load-deformation tests.

profile on the turbine blade is highly complex, these tests provide a baseline performance survey to both confirm design behavior and calibrate future numerical models. Note that because the deformation in each test was applied at the blade tip and the deflections were measured slightly inside the maximum radius of the blade's sweep, simple beam theory was used to extrapolate the deflection and twisting responses to the tip. This was determined to be an acceptable approximation due to the small deflections and curvatures.

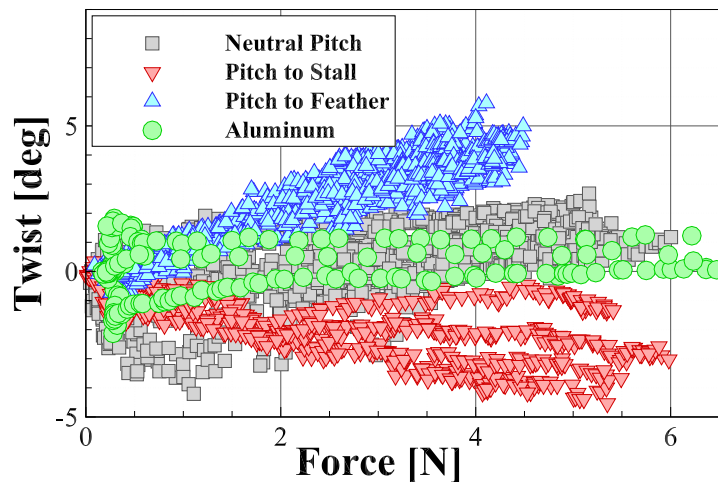
Figures 5.10a and 5.10b show the results of a suite of force-deformation tests. Point data from each of three tests conducted on every blade is reported. In Figure 5.10a, the strongly linear nature of the force-deflection response is clear. However, nonlinear behavior is apparent in deflections under 1 mm; this is likely due to a slight amount of play in the blade root-to-hub fitting. As expected, the aluminum blades display a nearly rigid behavior, showing maximum deflections on the order of 10% of those measured in the adaptive blades.

The adaptive composite blades behave similarly to the neutral design; however, the reduced stiffness that is a function of the adaptive mechanism can clearly be seen. The bending deformation of the pitch to feather and pitch to stall blades is effectively identical. This is to be expected, as the fiber angle offset, and thus stiffness reduction, is the same magnitude in the two blades designs.

The difference in the direction of the fiber angle offset can be seen in the force-twist response, shown in Figure 5.10b. Though the adaptive blades display very similar behavior



(a) Force-deflection response at blade tip



(b) Force-twist response at blade tip

Figure 5.10: Load-dependent elastic deformation responses of each blade type

in bending, the force-twist responses in the two designs are opposite. The pitch to feather blades show a positive pitch change, while the pitch to stall blades twist in a negative direction. Again, the aluminum blades display effectively rigid behavior, while the neutral composite shows a slight bias towards pitching to feather (increasing pitch). The trends in these results are also linear, though the correlation is less strong than in the force-deflection responses. The scatter in Figure 5.10b is due to the difficulty in imposing a displacement on the blade tip without influencing the twisting deformations. Though the blades were loaded at a point as close to the neutral pitch axis as possible, any small deviation from that point will have a significant impact on the twist response.

The deflection and pitch change responses are combined in Figure 5.11 to show empirical bend-twist relationships. A linear regression for each blade design is plotted for additional clarity. As expected, the bend-twist response of the pitch to feather blades is approximately equal in magnitude (as measured from the neutral pitch behavior) and opposite in direction to that of the pitch to stall blades. Though the aluminum blades displayed effectively rigid behavior by neither bending nor twisting to a significant extent, they show the same influence of the slight geometric bias to pitch to feather as the neutral composite blades, a behavior that agrees with previous numerical predictions [6]. However, the correlation of the aluminum bend-twist response especially is quite low, and additional tests are necessary for conclusive results.

In general, the results of the load-deformation tests showed good agreement with design goals and behavior predictions stated in the previous section. The pitch to feather blades displayed a bias to increase blade pitch under load, while the pitch to stall design tended to decrease blade pitch. Both adaptive designs were slightly more flexible than the neutral composite, and the assumption of rigidity for the aluminum blades was shown to be an acceptable approximation.

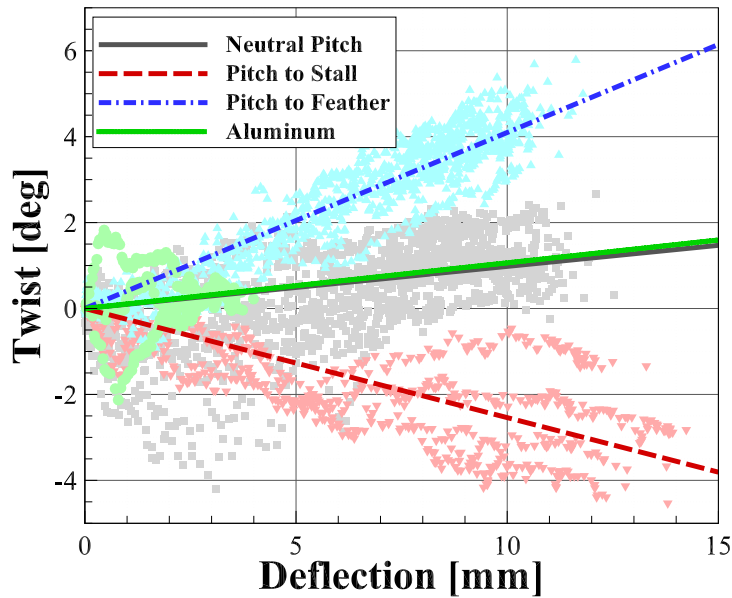


Figure 5.11: Deflection-twist relationship, with linear regression plotted

### 5.2.6 Flume Experiment Results

In addition to the static test program, dynamic experiments were conducted at the Bamfield Marine Sciences Center in Bamfield, BC, Canada. It must be noted that the flume experiments were conducted by a different, more senior researcher within the research group rather than the author of this thesis. Her research is more concerned with turbine performance characterization and turbine-level differences due to the adaptive blade mechanism, rather than the development of the blades themselves, which was the focus of this Chapter. The results of the flume experiment, however, are equally important to this work, thus are included here.

The Bamfield facility includes a recirculating rectangular open channel flume ( $b = 0.98$  m,  $L = 13$  m). Fluid velocity in the flume is controlled by a series of four pumps, allowing for speeds of up to 1.0 m/s. The dynamic water depth and temperature were held constant at  $h_d = 0.73$  m and  $T = 16^\circ$  C, respectively, for all tests. The level of turbulence in the flume was around 7-8%, consistent with field measurements in Puget Sound and previous

flume experiments in the literature ([28]). The turbine was placed near the center of the flume longitudinally, with the hub height,  $h_{hub} = 0.375$  m, set to approximately half of the static water depth in the flume. Performance curves were generated by holding the fluid velocity constant and increasing turbine rotational speed, in order to measure loads over a range of tip speed ratios. Measurements at each point on the performance curve were sampled at  $\approx 16$  Hz for 2-5 minutes to ensure steady state operation. Due to the load-dependent nature of the adaptive blades, however, performance is dependent on both velocity and tip speed ratio. Therefore, curves were collected for the adaptive pitch blades at three inflow velocities:  $U_{hub} = 0.5$  m/s,  $0.65$  m/s, and  $0.85$  m/s, resulting in a range of Reynolds numbers  $Re_D = 2.0e5 - 3.4e5$  ( $Re_c \approx 0.7e5 - 1.1e5$ ). For comparison with the composite blades and to investigate effects of Reynolds number dependence, performance curves for the rigid aluminum blades were collected at  $U_{hub} = 0.5$  m/s,  $0.85$  m/s, and  $1.0$  m/s.

To investigate the performance behavior of the adaptive blades as compared to the non-adaptive and rigid designs, forces and moments on the key blade of each turbine system were recorded during dynamic testing. In the blade load cell, the  $x$ -direction points from the leading to the trailing edge of the blade at the  $0^\circ$  pitch line, the  $y$ -direction points upstream, and the  $z$ -direction points out radially along the blade. The coordinate systems for both load cells can also be found in Fig. 5.8. During flume testing, a Nortek Vector acoustic Doppler velocimeter (ADV) was positioned approximately  $1.1$  m ( $\approx 2.5 d_T$ ) upstream of the turbine. The ADV sampled instantaneous three-dimensional inflow velocities. The  $x$ -direction of the ADV is oriented upstream and the  $y$ - and  $z$ -directions reflect horizontal and vertical velocities, respectively.

Using data from the blade load cell and ADV, it is possible to calculate the mean forces and moments on the key blade as a function of tip speed ratio ( $\lambda = R\omega/U_{avg}$ ) for each inflow velocity. These trends for all four blade designs are shown in Figure 5.12 for the tests run

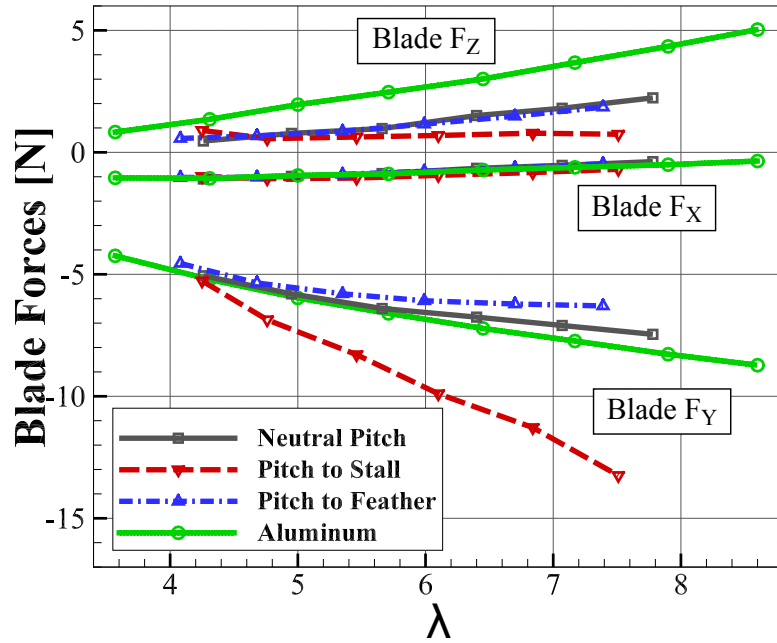
at  $U_{hub} = 0.50$  m/s. The first item to notice in these figures is that the neutral pitch (non-adaptive) composite blade and the aluminum blade perform similarly in nearly all respects. The only significant difference between the two is in the z-direction force, shown in Figure 5.12a. This is the centripetal force, which is larger in magnitude for the aluminum blades due to their higher total mass; the general increase in this force corresponds to the increase in rotational velocity. Beyond  $BF_Z$ , all four blade designs trend together in the x-direction forces and moments and the y-direction moments. It is worth noting that the blade pitching moment ( $BM_Z$ ) is essentially zero for all blades. This indicates that any twist the blades experience will likely be due to the bend-twist mechanism, rather than any outside forcing.

The largest difference by far between designs can be seen in the y-direction, or stream-wise, forces (Figure 5.12a) and the x-direction, or bending, moments (Figure 5.12b). These streamwise forces and the associated bending moments are the main driver for the load-dependent adaptive pitch mechanism. Thus, at low tip speed ratios the blades experience similar loading conditions, but as the forces on the system increase the performance of the different blade designs begin to diverge. As noted above, the neutral and aluminum blades behave in a similar manner, providing a baseline model for comparison. The difference in forces and moments on the adaptive blade designs is attributable to the predicted twist deformations. Under increased load, the pitch to stall blade will twist to decrease the pitch angle, effectively increasing the angle of attack. This was shown statically in Figure 5.10b as well as predicted numerically in [6]. The increase in angle of attack in turn causes the higher forces and moments seen in Figure 5.12. In the opposite fashion, the pitch to feather blade twists to decrease the angle of attack and starts to shed excess loads, resulting in a reduced rate of increase in the forces and moments.

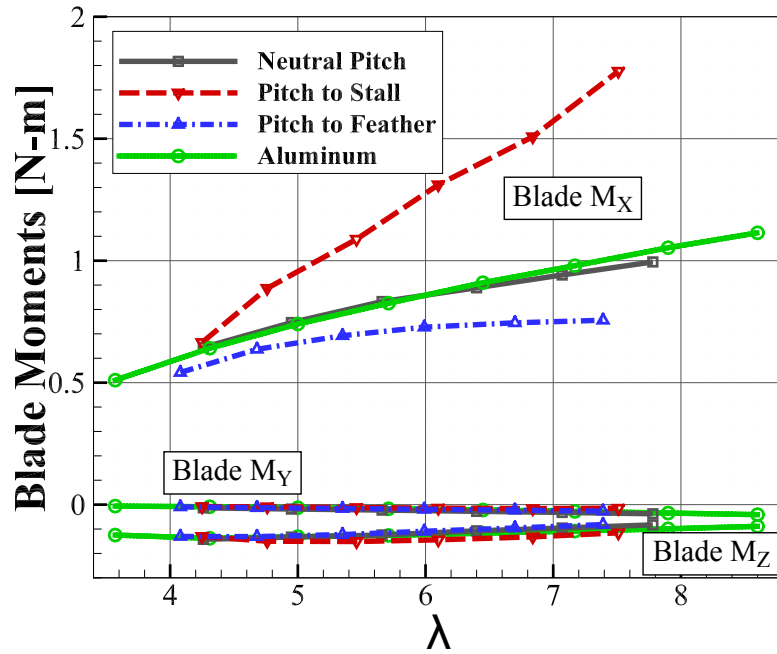
Along with blade loads, rotor force and moment measurements were collected. Turbine performance is commonly characterized in terms of power and thrust coefficients; to that end, the instantaneous axial thrust ( $T$ ), moment ( $\tau$ ), velocity ( $U_{hub}$ ), and angular

velocity ( $\omega = 2\pi f_T$ ) measurements were used to calculate the system thrust coefficient,  $C_T = T / (0.5\rho A_T U_{hub}^2)$ , and power coefficient,  $C_P = (\tau\omega) / (0.5\rho A_T U_{hub}^3)$  for all four blade designs. The resulting performance curves, calculated from the tests conducted at  $U_{hub} = 0.50$  m/s, are shown in Figure 5.13. Error bars are used to indicate the 95% confidence interval of this data. The larger error bars seen on the calculated power coefficients relative to the thrust coefficients are likely due to the slightly higher accuracy of the hub load cell in reading thrust as compared to torque measurements.

The thrust coefficients, in Figure 5.13a, generally reflect the individual blade trends seen previously. The pitch to stall system experiences increased thrust compared to the neutral pitch design as the tip speed ratio increases, while the pitch to feather system sheds load over the same range. The neutral pitch system differs slightly from the aluminum blades, but maintains a similar trend. In Figure 5.13b, the calculated power coefficients are displayed. Though all four designs show comparable performance behavior, there are several features to highlight. From the lower tip speed ratios to the apex of the curve, the pitch to stall blade produced a generally higher  $C_P$  than the other designs. The pitch to feather blade had the lowest calculated value, while the neutral and aluminum blades fell in between. However, at higher tip speed ratios, the performance of all three composite blades falls off much more steeply than the aluminum blades. This is likely due to the fact that the composite blades, especially of the pitch to stall design, showed considerable out-of-plane deformation with increased trust on the system. In this case, increased lift on the foils will not translate as directly to increased torque on the system, and much of the gains in performance expected from the pitch to stall system would be lost



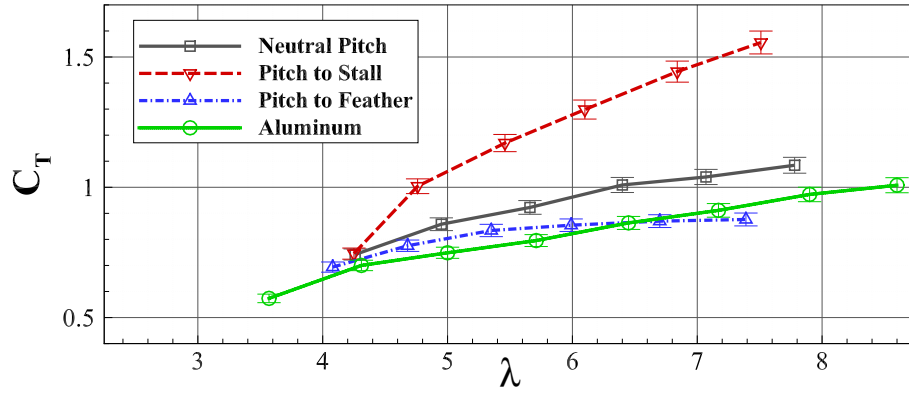
(a) Average forces on the key blade at  $U_{hub} = 0.50$  m/s



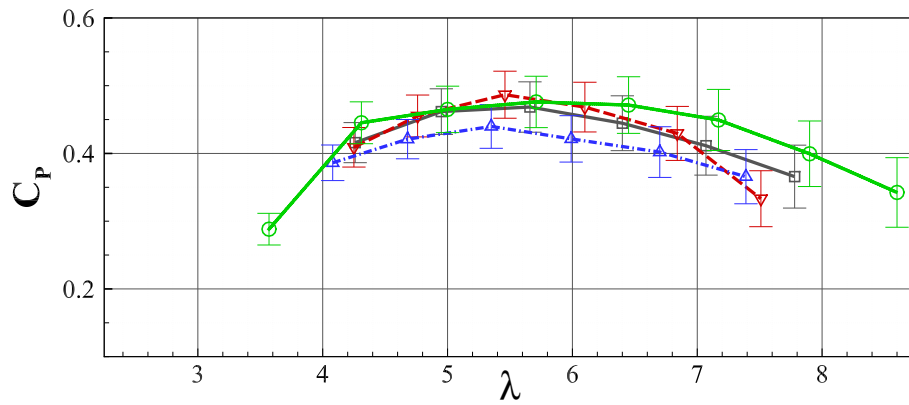
(b) Average moments on the key blade at  $U_{hub} = 0.50$  m/s

Figure 5.12: Blade load cell measurements with increasing  $\lambda$  at  $U_{hub} = 0.50$  m/s





(a) Calculated thrust coefficients at  $U_{hub} = 0.50$  m/s



(b) Calculated power coefficients at  $U_{hub} = 0.50$  m/s

Figure 5.13: System performance characteristics with increasing  $\lambda$  at  $U_{hub} = 0.50$  m/s

# Chapter 6

## Conclusions and Future work

### 6.1 Conclusions

#### 6.1.1 Fundamentals

In this thesis, bend-twist coupled composite laminate beams were characterized experimentally, numerically, and analytically in both static and dynamic load settings. Several sets of beams were manufactured as specimens for experimentation, cured both by autoclave as well as by hot press. Experiments conducted on the beams included static force-deflection, free vibration ring down, small amplitude frequency sweep and large amplitude frequency sweep. Motivation for the suite of experiments involved understanding the relationship between bending and twisting deformations when loaded statically, as well as how bend-twist coupling reduces stiffness and affects the structure's dynamic response. Large amplitude frequency sweeps were conducted in an attempt to illicit frequency stiffening or softening due to geometric nonlinearities.

Two analytical methods of analysis were presented as well. An existing analytical model which relies on solving the coupled equations of motion for a bend-twist coupled composite cantilever was programmed and implemented. Additionally, a beam element for use in the

stiffness matrix method was derived in order to analytically model the beam deformation under static loading. The stiffness matrix model was also extended into the dynamics regime by formulating the common vibration eigenvalue problem.

A numerical model was developed in ABAQUS with steps for static loading and linear perturbation frequency analysis. The addition of the numerical model rounds out the spectrum of analysis and evaluation methods for bend-twist coupled beams presented in this work.

### 6.1.2 Material Testing

In order to appropriately model the structural response of the beams, material properties had to first be established. Composite laminates are notoriously difficult to characterize and often have highly varying material properties. A suite of experiments including tensile testing, three-point bending, cantilever bending, and free vibration were implemented in an attempt to establish fiber-direction elastic modulus,  $E_1$ , for the coupled beams.

Results varied significantly in a number of ways. First, each experiment yielded different average properties. Tension testing yielded higher values than three-point bending, which were higher still than cantilever bending results. Second, the method of manufacture resulted in different elastic moduli with hot-press-cured beams giving higher values than autoclave cured beams. Furthermore, the 16-ply autoclave beams showed lower values than the 8-ply autoclave beams, which suggests some degree of thickness dependence. Lastly, beam modulus varied significantly based on the location from where it was cut in the original laminate. There was no consistent observable trend suggesting a particular location in the laminate yielded higher or lower values, however.

In order to investigate whether composites are truly so difficult to characterize, two tests were performed on a set of structural steel specimens, which has a well-known elastic modulus as it is a homogeneous, isotropic material. Free vibration and cantilever bending tests were

conducted on the steel specimens, with the free vibration experiment yielding an average elastic modulus of  $\approx 0.3$  GPa ( $\approx 0.1\%$ ) higher than established by cantilever bending. This suggests that the steel specimens can be characterized reasonably closely across experimental methods, unlike the composite beams.

Finally, composite laminates are shown to, indeed, be difficult to characterize experimentally with results differing drastically with respect to multiple variables, not limited to experimental method, curing method, boundary conditions, and laminate thickness. Thus, the author chose to move forward with effective material properties corresponding to beams and boundary conditions that most closely matched the experiments which were conducted. Elastic modulus characterized by cantilever bending was chosen as the baseline value to be used in the models for analysis.

### **6.1.3 Comparison of Results**

In general, it was shown by comparing experimental results with analysis methods that the material properties were still not fully accurate. Comparing results for force-deflection, the ABAQUS model is consistently stiffer and more coupled across all beams. The stiffness matrix method captures small deflections well, consistent with both ABAQUS and experimental results, but becomes irrelevant for large deflections due to geometric nonlinearity conditions. The ABAQUS model deviates most significantly from the experimental data when deflections are largest and geometric nonlinearity is most severe.

For linear, small amplitude dynamics, several things are worth noting. First, the natural frequencies for each beam differed based on which experiment was conducted. Free vibration consistently yielded higher natural frequencies than the small amplitude frequency sweep for all beams. The ABAQUS frequency analysis consistently over-approximated the natural frequency compared to both experimental results as well as analytical methods. This is consistent with the results from the static experiment as well, where ABAQUS approximated

slightly stiffer. The two analytical methods were nearly identical in predicting natural frequency, however neither method matched experimental results consistently for every beam. Generally, both ABAQUS and the analytical methods predicted within a few Hertz of the experimentally established values, but the approximation is limited to within a fairly coarse frequency range. This is true for higher order bending modes and torsional modes as well.

Large amplitude vibration did not yield any frequency stiffening or softening effects. An order of magnitude increase in excitation accelerations (from 1G to 10G) doubled the beam deflections, yet did not change the beam natural frequency significantly. Modeling the beam's dynamic response for such large forcing and geometric nonlinearities was deemed to be extraneous and too time consuming to provide meaningful contribution to this work. Thus, only the experimental results for the large amplitude frequency sweep were presented.

Lastly, for the linear domain, the SMM was shown to be a valid, accurate, and easily implemented model for the analysis of bend-twist coupled beams. The SMM is easily programmed, does not rely on solving the governing equations for the particular boundary conditions, and is as or more accurate than a far-more-complicated ABAQUS numerical model for modeling beam response both statically and dynamically.

#### **6.1.4 Applications of Bend-Twist Coupled Composites**

The motivation for this section was to develop experimental scale passive pitch adaptive blades as a proof of concept research initiative. The blades were designed to have a composite spar that dictated the structural response, while a flexible urethane made up the blade surface geometry. A parametric study was conducted in ABAQUS to establish the optimal degree of bend-twist coupling and laminate thickness to achieve target deflection goals for the expected loading conditions. The performance of two sets of adaptive composite blades, one designed to pitch to stall and one to pitch to feather, were compared to that of a neutral pitch blade design and an effectively rigid aluminum set under static and dynamic testing conditions.

During static qualification testing, force-deflection and force-twist response were measured. Additionally, an empirical deflection-twist relationship was calculated. Though both adaptive blades behaved similarly in bending, the pitch to stall blades were found to twist to decrease blade pitch under load (which would increase effective angle of attack), while the pitch to feather design instead twisted to increase blade pitch (decreasing angle of attack). The neutral pitch blades were shown to be slightly stiffer than the adaptive designs in bending, and evidenced a slight bias towards pitching to feather under load. The assumption of rigidity for the aluminum blades was shown to be valid, though these blades also displayed a geometric pitch to feather bias.

Dynamic experiments were also performed in the flume at the Bamfield Marine Sciences Center. During these tests, instantaneous forces and moments were recorded on the turbine system and on one of the three blades during operation at varying rotational speeds and inflow velocities. Combined with the instantaneous fluid velocity measurements, these data were used to quantify blade forces and moments as a function of tip speed ratio, as well as overall system performance curves at several inflow velocities. The results of these tests show that in general, the pitch to stall blades experience increased forces and moments compared to the neutral pitch and aluminum blades. This translates to increased power generation at low dimensional loads, but under higher loading conditions caused excessive out of plane deformation, potential fluid stall, and blade failure. In the opposite fashion, the pitch to feather systems demonstrated lower blade loads and system thrust, with a relatively small decrease in power capture capabilities. This feature could prove a valuable asset to a marine hydrokinetic turbine system.

## **6.2 Future Work**

### **6.2.1 Material Characterization**

Characterizing composite laminates accurately has proven to be a challenge for reasons described above and in Chapter 3.6. A more robust testing schema needs to be implemented for thin laminates to more accurately establish elastic moduli as well as other critical material parameters such as shear modulus and resin modulus. Doing so will provide better ability to model and predict structural response of the coupled laminates. This was not the central objective of this thesis, which is why the material characterization tests were not fully comprehensive.

### **6.2.2 Co-rotational Adaptation of Stiffness Matrix Method Model**

The current stiffness matrix method model is only useful in the geometrically linear response domain. It cannot capture the effects of geometric nonlinearity and large deflections as demonstrated in Section 4.1. The stiffness matrix could, however, be implemented into a co-rotational model to account for large deflections and geometric nonlinearity. This would provide a more comprehensive analytical model that could then be compared more completely with an ABAQUS shell or continuum FEM.

### **6.2.3 Larger Scale Experimentation of Passively Adaptive Marine Turbine Blades**

In terms of application, future work includes scaling the passively adaptive marine turbine blades to a more realistic geometry and design and manufacture methods. Rather than another “flume-scale” experiment, the next iteration would take on a “field-scale” geometry which would likely be at least two times larger in diameter. The blades would need to be

manufactured differently, as designing a flat spar with a urethane profile would require a prohibitively thick spar and a large amount of liquid urethane. Instead, a box section with bend-twist coupling in the flanges and an outer skin may serve as a better design while being much more representative of actual manufacturing and design practices. Such an experiment would also shed light on turbine performance scaling effects and help understand how to best implement bend-twist coupling at a more realistic scale.



# Bibliography

- [1] J.R. Vinson and R.L. Sierakowski. *The Behavior of Structures Composed of Composite Materials*. Martinus Nijhoff, 1987.
- [2] Liviu Librescu and Ohseop Song. On the static aeroelastic tailoring of composite aircraft swept wings modelled as thin-walled beam structures. *Journal of Composites Engineering*, 2(5-7):497–512, 1992.
- [3] James Locke and Ulyses Valencia. Design studies for twist-coupled wind turbine blades. Technical report, Sandia National Laboratories, 06 2004.
- [4] Thomas D. Ahswill. Passive load control for large wind turbines. Technical report, Sandia National Laboratories, 2010.
- [5] Ramona B. Barber, Craig S. Hill, Pavel F. Babuska, Michael R. Motley, and Richard Wiebe. Flume-scale testing of an adaptive pitch marine turbine system. *Journal of Composite Structures*, 168:465–473, 05 2017.
- [6] Michael R. Motley and Ramona B. Barber. Passive control of marine hydrokinetic turbine blades. *Journal of Composite Structures*, 110:133–139, 2014.
- [7] Michael R. Motley and Ramona B. Barber. Passive pitch control of horizontal axis marine hydrokinetic turbine blades. In *Proceedings of the ASME 2014 33rd International Conference on Ocean, Offshore and Arctic Engineering*, 06 2014.

- [8] Sebastien Gauthier Perron. Passive gust load alleviation through bend-twist coupling of composite beams on typical commercial airplane wings. Master's thesis, Massachusetts Institute of Technology, 09 2012.
- [9] Azzam Ahmed. Theoretical and experimental methods on bend-twist coupling and damping properties with the relationship to layup of the composite propeller marine: A review. *International Journal of Engineering Science and Technology*, 4(6):2907–2917, 06 2012.
- [10] Asfaw Beyene and James Peffley. Constructal theory, adaptive motion, and their theoretical application to low-speed turbine design. *Journal of Energy Engineering*, pages 112–118, 12 2009.
- [11] Yin Lu Young, Michael R Motley, Ramona Barber, Eun Jung Chae, and Nitin Garg. Adaptive composite marine propulsors and turbines: Progress and challenges. *Applied Mechanics Reviews*, 68(6), 2016.
- [12] Yin Lu Young, Z Liu, and Michael R Motley. Influence of material anisotropy on the hydroelastic behaviors of composite marine propellers. In *Proceedings of the 27th Symposium on naval hydrodynamics, Seoul, Korea*, 2008.
- [13] Kuen Y. Lin. AA532 mechanics of composites coursework. Lecture Notes, 09 2016.
- [14] SIMULIA by Dassault Systemes. *ABAQUS Version 6.14 Documentation*, 2014.
- [15] Kristin Marlett. Hexcel 8552 IM7 unidirectional prepreg 190 gsm & 35%RC qualification material property data report. Technical report, National Institute for Aviation Research, 04 2011.
- [16] R.C. Hibbeler. *Structural Analysis*. Pearson Prentice Hall, Upper Saddle River, New Jersey 07458, 8th edition, 2012.

- [17] Lars Andersen and Soren R.K. Nielsen. Elastic beams in three dimensions, DCE lecture notes no. 23. Aalborg University Lecture Notes, August 2008.
- [18] Terrence A. Weisshaar and Brian L. Foist. Vibration tailoring of advanced composite lifting surfaces. *Journal of Aircraft*, 22(2):141–147, 02 1985.
- [19] Matthew R. Kramer, Zhanke Liu, and Yin L. Young. Free vibration of cantilevered composite plates in air and in water. *Journal of Composite Structures*, 95:254–263, 2013.
- [20] Ricardo De Frias Lopez. A 3D finite beam element for the modelling of composite wind turbine wings. Masters thesis, Royal Institute of Technology (KTH), 2013.
- [21] J.R. Banerjee. Coupled bending-torsional dynamic stiffness matrix for beam elements. *International Journal for Numerical Methods in Engineering*, 28(6):1283–1298, 1989.
- [22] Elisa Claire Borowski. Viscoelastic effects in carbon fiber reinforced polymer strain energy deployable composite tape springs. Master’s thesis, The University of New Mexico, 05 2017.
- [23] NASA. Dryden flight research center EC90-039-4. Photograph, 1990. Photographed by Larry Sammons.
- [24] Bernhard CF Klein. Photograph no 7697 sukhoi su-47 berkut (golden eagle). <http://1000aircraftphotos.com/Contributions/KleinBernhard/7697.htm>, 04 2008.
- [25] Paul Veers, Donald Lobitz, and Gunjit Bir. Aeroelastic tailoring in wind-turbine blade applications. In *Windpower '98, American Wind Energy Association Meeting and Exhibition*, 1998.
- [26] Vladimir Fedorov. *Bend-Twist Coupling Effects in Wind Turbine Blades*. PhD thesis, Technical University of Denmark, 07 2012.

- [27] R.F. Nicholls-Lee, S.R. Turnock, and S.W. Boyd. Application of bend-twist coupled blades for horizontal axis tidal turbines. *Journal of Renewable Energy*, 50:541–550, 08 2013.
- [28] Jim Thomson, Brian Polagye, Vibhav Durgesh, and Marshall C Richmond. Measurements of turbulence at two tidal energy sites in puget sound, wa. *IEEE Journal of Oceanic Engineering*, 37(3):363–374, 2012.
- [29] Fibre Glast Developments Corp. Free composites learning materials and white papers. [http://www.fibreglast.com/category/Learning\\_Center](http://www.fibreglast.com/category/Learning_Center), 2017. Accessed: 2017-07-20.

# Appendix A

## Supplementary Information

### A.1 Hexcel IM7/8552 Curing Details

#### A.1.1 Cure Profile

The cure profile for all IM7 layups used in this work are shown below in Figure A.1. One adaptation was made, however, where the curing pressure for the duration of the event was reduced to 50 psi or 3.45 bar. First, the autoclave used in the cures presented in this work was limited to a max pressure of 85 psi or 5.86 bar. Second, the unidirectional laminates would suffer from excessive “smushing” under higher cure pressures, thus slightly lower pressures were used to minimize in-cure laminate deformation. Otherwise, the temperature profile followed the figure exactly.

### Curing Cycle for Honeycomb and Monolithic Components

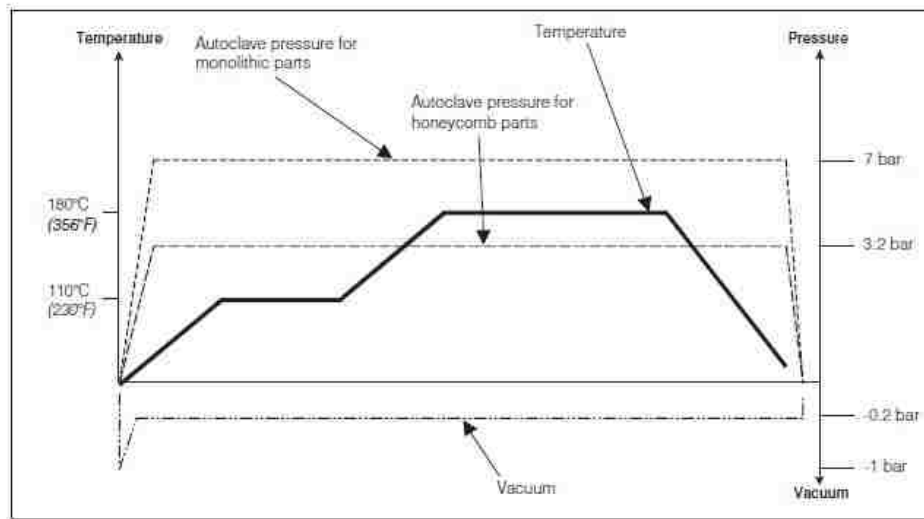


Figure A.1: Cure profile from Hexcel for IM7/8552

## A.1.2 Autoclave Bagging Process

The autoclave bagging process can be depicted by Figure A.2. The graphic was taken directly from the instruction techniques from composites supplier, Fibre Glast Development Corporation [29].

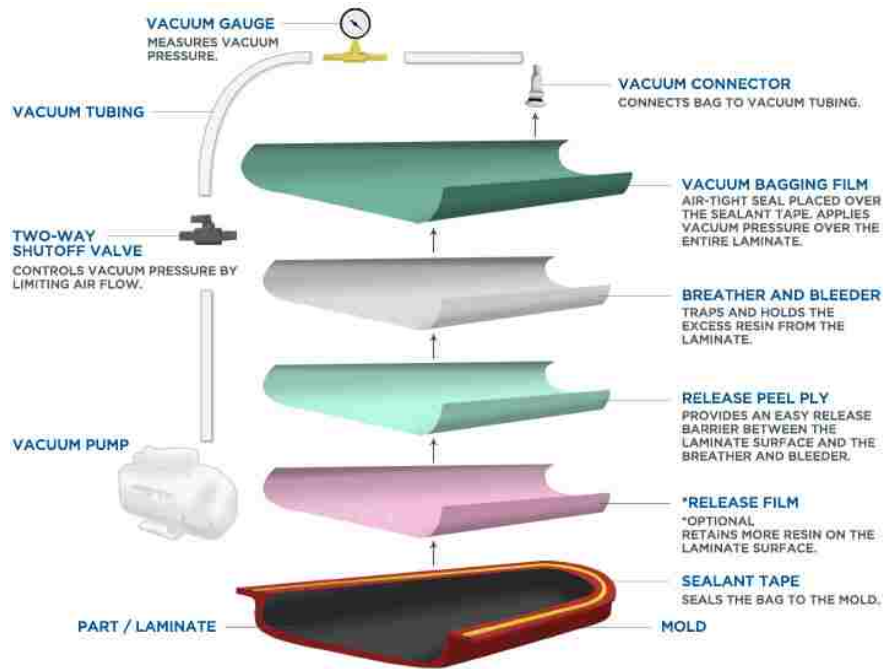


Figure A.2: Vacuum bagging diagram for autoclave-cured composite laminates, schematic sourced from [29]

## A.2 Model Scripts

### A.2.1 ABD Matrix Script

```
1 function [ABD, abd, Ex] = ABD_abd(E11, E22, G12, v12, Nplies, t, layup)
2
3 % Additional Poisson's ratios
4 v21 = v12*(E22/E11);
5
6 % Enter geometric properties
7 h = Nplies*t;           % total thickness of laminate (m)
8
9 % Initializing arrays
10 Qbar = zeros(3,3,Nplies);
11 A = zeros(3,3);
12 B = zeros(3,3);
13 D = zeros(3,3);
14
15 % Qij
16 Q11 = E11/(1-v12*v21);
17 Q22 = E22/(1-v12*v21);
18 Q12 = v12*E22/(1-v12*v21);
19 Q66 = G12;
20
21 % Zbar is the coordinates of the plies in the layup
22 for i = 1:Nplies+1;
23     zbar(i) = - ((h)/2 + t) + i*t;
24 end;
25
26 % Qbarij for each lamina of laminate
27 for k = 1:Nplies
28
29     c = cosd(layup(k));
30     s = sind(layup(k));
31
32     Qbar(1,1,k) = Q11*c^4 + 2*(Q12 + 2*Q66)*s^2*c^2 + Q22*s^4;
33     Qbar(1,2,k) = (Q11 + Q22 - 4*Q66)*s^2*c^2 + Q12*(s^4 + c^4);
34     Qbar(2,1,k) = Qbar(1,2,k);
35     Qbar(2,2,k) = Q11*s^4 + 2*(Q12 + 2*Q66)*s^2*c^2 + Q22*c^4;
```



```

36     Qbar(1,3,k) = (Q11 - Q12 - 2*Q66)*s*c^3 + (Q12 - Q22 + 2*Q66)*s*c^3;
37     Qbar(3,1,k) = Qbar(1,3,k);
38     Qbar(2,3,k) = (Q11 - Q12 - 2*Q66)*s^3*c + (Q12 - Q22 + 2*Q66)*s*c^3;
39     Qbar(3,2,k) = Qbar(2,3,k);
40     Qbar(3,3,k) = (Q11 + Q22 - 2*Q12 - 2*Q66)*s^2*c^2 + Q66*(s^4 + c^4);
41
42 end
43
44 % Establishing A, B, and D matrices
45 for i=1:3
46     for j=1:3
47         for k = 1:Nplies
48             A(i,j) = A(i,j) + Qbar(i,j,k)*(zbar(k+1) - zbar(k));
49             B(i,j) = B(i,j) + (1/2)*(Qbar(i,j,k)*(zbar(k+1)^2 - zbar(k)^2));
50             D(i,j) = D(i,j) + (1/3)*(Qbar(i,j,k)*(zbar(k+1)^3 - zbar(k)^3));
51         end
52     end
53 end
54
55 % Make ABD, abd matrix
56 ABD = [A B;B D];
57 abd = inv(ABD);
58
59 \% Getting Ex Ey Gxy
60 a = inv(A);
61 Ex = 1/(h*a(1,1));
62 Ey = 1/(h*a(2,2));
63 Gxy = 1/(h*a(3,3));
64
65 end

```

## A.2.2 Stiffness Matrix Method Model Scripts

```
1
2 % -----
3 % Element Mass and Stiffness Matrices for Stiffness Method of Analysis of
4 % Bending-Torsion Coupled Laminated Composite Beams
5 % -----
6 % Author: Pavel Babuska
7 % Date:   Spring 2017
8 % -----
9
10 clc; clear; close all;
11 format shortg;
12
13 % ----- ENTER KNOWN MATERIAL INFORMATION -----
14 % Enter known lamina properties
15 E1 = 141e9;      % Pascals
16 E2 = 8.96e9;    % Pascals
17 G12 = 4.69e9;   % Pascals
18 t = 0.131e-3;   % Ply thickness (m)
19
20 % Poisson's Ratios
21 v12 = 0.316;
22 v21 = v12*E2/E1;
23 v23 = v12*(1-v21)/(1-v12);
24
25 % ----- ENTER LAMINATE INFORMATION -----
26 % Types: QuasiIso, SameAngle, General
27 type = 'General';
28
29 % Manually enter layup info here, in the correct respective section for
30 % which type of laminate is being designed/analysed
31 if strcmp(type, 'QuasiIso') == 1
32     layup = [0 45 -45 90 90 -45 45 0]; % Enter layup angles in degrees here
33     Nplies = length(layup);
34     h = Nplies*t; % Total thickness of laminate (m)
35
36 elseif strcmp(type, 'SameAngle') == 1
37     Nplies = 8; % Enter number of plies
38     offset = 0; % in degrees
```

```

39     layup = offset.*ones(1, Nplies);
40     correction = 0.1889;           % thickness correction due to cure flattening
41     t = (1-correction)*t;         % Corrected ply thickness (m)
42     h = Nplies*t;
43
44 elseif strcmp(type, 'General') == 1
45     layup = [0 0 90 90 0 0];      % Enter layup angles in degrees here
46     Nplies = length(layup);
47     correction = 0.00;           % thickness correction due to cure flattening
48     t = (1 - correction)*t;      % Corrected ply thickness (m)
49     h = Nplies*t;
50
51 end
52
53 % Function call to get ABD, abd matrices and effective elastic modulus
54 [ABD, abd, Ex] = ABD_abd(E1, E2, G12, v12, Nplies, t, layup);
55 ABD
56 % ----- ENTER KNOWN BEAM INFORMATION -----
57 b = 0.02464;                    % Beam width (m)
58 L = 0.21;                       % Beam length (m)
59 rho = 1570;                     % Mass density kg/m3
60 n_el = 20;                      % Number of elements to be discretized into
61
62 % Function call to get the global, complete, Mass and Stiffness matrices
63 [K_Global, M_Global, EIy, GJ, KK] = elementKM(ABD, Ex, b, h, L, rho, n_el);
64
65 % Sensitivity Ratio of the laminate designates the level of importance of
66 % including Bending-Torsional coupling in the analysis.
67 sensRatio = (ABD(4,6) - ABD(4,5)*ABD(5,6)/ABD(5,5))^2/...
68     ((ABD(6,6) - ABD(5,6)^2/ABD(5,5))*(ABD(4,4) - ABD(4,5)^2/ABD(5,5)));
69
70 % sensRatio = (ABD(4,6))^2/(ABD(4,4)*ABD(6,6));
71
72 % SR of >0.1 is considered 'high' and would suggest the
73 % inclusion of BT coupling in the stiffness matrix.
74 sensRatio
75
76
77 %%

```

```

78 % -----
79 % Now that we've made strides in setting up element stiffness matrix, let's
80 % establish a load and displacement vector to get this working from a
81 % stiffness method approach to analysis.
82 % -----
83
84
85 % ----- ENTER KNOWN LOADING AND BOUNDARY CONDITIONS -----
86 % Load and displacement degree of freedom convention
87 % Load = [Nx1 Fy1 Fz1 Mx1 My1 Mz1 Nx2 Fy2 Fz2 Mx2 My2 Mz2];
88 % U = [wx1 wy1 wz1 thx1 thy1 thz1 wx2 wy2 wz2 thx2 thy2 thz2];
89 P = zeros(1, 6*(n_el + 1));
90 U = zeros(1, 6*(n_el + 1));
91 % U(7) = 1; % meters
92 P(end - 3) = 0.5; % Newtons
93
94 % Boundary conditions
95 DoF = 1:length(K_Global);
96 fixed = [1:6];
97 free = DoF(ismember(DoF, fixed) ~= 1);
98
99 % Partitioning
100 Kff = K_Global(free, free);
101 Kfr = K_Global(free, fixed);
102 Krf = K_Global(fixed, free);
103 Krr = K_Global(fixed, fixed);
104
105 Mff = M_Global(free, free);
106 Mfr = M_Global(free, fixed);
107 Mrf = M_Global(fixed, free);
108 Mrr = K_Global(fixed, fixed);
109
110 Pf = P(free);
111 Pr = P(fixed);
112
113 %% For unit displacements case
114 % Ur = U(fixed);
115 % Uf = double(vpa(Kff\(-Kfr*Ur')));
116 % U(fixed) = Ur;

```

```

117 % U(free) = Uf;
118 % U';
119
120 % For applied load
121 Ur = U(fixed);
122 Uf = double(vpa(Kff\Pf'));
123
124 status = 'Off';
125 if strcmp(status, 'On') == 1
126     % For cantilever displacements between the nodes
127     clear x
128     x = 0.12;      % Measurement sensing distance
129     y = (P(end - 3)*x^2)*(3*L - x)/(6*(EIy - KK^2/GJ))
130     theta_x = Uf(end - 2)*180/pi
131     theta_y = Uf(end - 1)*180/pi;
132 else
133 end
134
135
136 %%
137 % -----
138 % Applications of the element stiffness matrix include the ability to
139 % calculate the beam natural frequencies from solving the eigenvalue
140 % problem as long as the mass and stiffness matrices are formulated
141 % -----
142
143 % ----- Natural Frequency -----
144 % For a SameAngle laminate type with no coupling such as in a [0] or cross
145 % ply [0 90 ...], D16 is 0 resulting in no coupling, and thus the
146 % well-known analytical solution for cantileverl natural frequency can be
147 % implemented. Note this first conditional is for uncoupled CANTILEVER ONLY.
148 % nf(1) = (1.875^2*sqrt(EIy/(rho*b*h*L^4)))/(2*pi);
149 % nf(2) = (4.694^2*sqrt(EIy/(rho*b*h*L^4)))/(2*pi);
150 % nf(3) = (7.855^2*sqrt(EIy/(rho*b*h*L^4)))/(2*pi);
151
152 status = 'Off';
153 if strcmp(status, 'On') == 1
154     % Generally, though, this is best.
155     [nf, modeShape] = eigenvalueBT(Mff, Kff);

```

```
156     nf(1:6)
157     modeShape(1:6,1:6)
158
159     % Nondimensionalization as in Kramer's paper
160     D0 = E1*h^3/(12*(1-v12*v21));
161     omega = nf.*(L^2)*sqrt(rho*h/D0);
162 else
163 end
```

## Element mass and stiffness matrix scripts for Stiffness Matrix Method code

```

1
2 % -----
3 % Element Mass and Stiffness Matrices for Stiffness Method of Analysis of
4 % Bending-Torsion Coupled Laminated Composite Beams
5 % -----
6 % Author: Pavel Babuska
7 % Date:   Spring 2017
8 % -----
9 function [K_Global, M_Global, EIy, GJ, KK] = elementKM(ABD, Ex, b, h, L, rho, n_el)
10
11 % Rigidities. These terms include thru-width flexibility, which
12 % appropriately results in reduced rigidities, hence the minus (BLAH)
13 % parts.
14 EA = Ex*b*h;
15 GJ = 4*b*(ABD(6,6) - ABD(5,6)^2/ABD(5,5));
16 KK = 2*b*(ABD(4,6) - ABD(4,5)*ABD(5,6)/ABD(5,5));
17 EIy = b*(ABD(4,4) - ABD(4,5)^2/ABD(5,5));
18 EIZ = Ex*(h*b^3)/12;
19
20 %% Rigidities. These terms assume thru-width (e.g. chord-wise) rigidity
21 %% in the beam. This gives a stiffer approximation and should not be used
22 %% the majority of the time.
23 % EA = Ex*b*h;
24 % GJ = 4*b*(ABD(6,6));
25 % KK = 2*b*(ABD(4,6));
26 % EIy = b*(ABD(4,4));
27 % EIZ = Ex*(h*b^3)/12;
28
29 % -----
30 % Shape Functions
31 % -----
32 syms x
33
34 % Element length
35 l_el = L/n_el;
36
37 % Extension
38 Na1 = 1 - x/l_el;

```

```

39 Na2 = x/l_el;
40
41 % Torsion
42 Nt1 = 1 - x/l_el;
43 Nt2 = x/l_el;
44
45 % Traditional Beam Bending
46 Nb1 = 1 - 3*(x/l_el)^2 + 2*(x/l_el)^3;
47 Nb2 = 3*(x/l_el)^2 - 2*(x/l_el)^3;
48 Nr1 = l_el*((x/l_el) - 2*(x/l_el)^2 + (x/l_el)^3);
49 Nr2 = l_el*((x/l_el)^3 - (x/l_el)^2);
50
51 % Approximated and/or new functions
52 Ntxz1 = (6*KK/(GJ*l_el^3))*(x^2 - l_el*x);
53 Ntxty1 = (3*KK/(GJ*l_el^2))*(l_el*x - x^2);
54 Ntxz2 = (6*KK/(GJ*l_el^3))*(l_el*x - x^2);
55 Ntxty2 = (3*KK/(GJ*l_el^2))*(l_el*x - x^2);
56 Ntyty1 = 1 - 4*(x/l_el) + 3*(x^2/l_el^2);
57 Ntyz1 = 6*(x/l_el^2) - 6*(x^2/l_el^3);
58 Ntyty2 = 3*(x^2/l_el^2) - 2*(x/l_el);
59 Ntyz2 = -6*(x/l_el^2) + 6*(x^2/l_el^3);
60 Ntztz1 = 1 - 4*(x/l_el) + 3*(x^2/l_el^2);
61 Ntzy1 = -6*(x/l_el^2) + 6*(x^2/l_el^3);
62 Ntztz2 = 3*(x^2/l_el^2) - 2*(x/l_el);
63 Ntzy2 = 6*(x/l_el^2) - 6*(x^2/l_el^3);
64
65 % -----
66 % Strain-Displacement and Constitutive Matrix relations
67 % -----
68
69 % For an uncoupled laminate such as [0] or crossply [0 90 ...], D16 = 0 and
70 % this first conditional results in classical stiffness matrix assembly and
71 % analysis. Otherwise, any other laminate should default to the most
72 % complete assembly and approximation in the next conditional
73 if ABD(4,6) == 0
74
75     C = [
76         EA 0 0 0;
77         0 GJ 0 0;

```



```

78     0 0 EIy 0;
79     0 0 0 EIz;
80     ];
81
82     B = [
83         diff(Na1) 0 0 0 0 0 diff(Na2) 0 0 0 0 0;
84         0 0 0 diff(Nt1) 0 0 0 0 0 diff(Nt2) 0 0;
85         0 0 diff(Ntyz1) 0 diff(Ntyty1) 0 0 0 diff(Ntyz2) 0 diff(Ntyty2) 0;
86         0 diff(Ntzy1) 0 0 0 diff(Ntztz1) 0 diff(Ntzy2) 0 0 0 diff(Ntztz2);
87     ];
88
89     N = [
90         Na1 0 0 0 0 0 Na2 0 0 0 0 0;
91         0 Nb1 0 0 0 Nr1 0 Nb2 0 0 0 Nr2;
92         0 0 Nb1 0 Nr1 0 0 0 Nb2 0 Nr2 0;
93         0 0 0 Nt1 0 0 0 0 0 Nt2 0 0;
94     ];
95
96     % Integrands
97     K = B'*C*B;
98     M = (rho*b*h).*N((1:3),:)'*N((1:3),:);
99     M = M + (rho*(b*h^3/12 + h*b^3/12)).*N(4,:)'*N(4,:);
100
101 else
102
103     C = [
104         EA 0 0 0;
105         0 GJ KK 0;
106         0 KK EIy 0;
107         0 0 0 EIz;
108     ];
109
110     B = [
111         diff(Na1) 0 0 0 0 0 diff(Na2) 0 0 0 0 0;
112         0 0 diff(Ntxz1) diff(Nt1) diff(Ntxty1) 0 0 0 diff(Ntxz2) diff(Nt2) diff(Ntxty2) 0;
113         0 0 diff(Ntyz1) 0 diff(Ntyty1) 0 0 0 diff(Ntyz2) 0 diff(Ntyty2) 0;
114         0 diff(Ntzy1) 0 0 0 diff(Ntztz1) 0 diff(Ntzy2) 0 0 0 diff(Ntztz2);
115     ];
116

```

```

117     N = [
118         Na1 0 0 0 0 0 Na2 0 0 0 0 0;
119         0 Nb1 0 0 0 Nr1 0 Nb2 0 0 0 Nr2;
120         0 0 Nb1 0 Nr1 0 0 0 Nb2 0 Nr2 0;
121         0 0 Ntxz1 Nt1 Ntxty1 0 0 0 Ntxz2 Nt2 Ntxty2 0;
122     ];
123
124     % Integrands
125     K = B'*C*B;
126     M = (rho*b*h).*N((1:3),:)'*N((1:3),:);
127     M = M + (rho*(b*h^3/12 + h*b^3/12)).*N(4,:)'*N(4,:);
128
129 end
130
131
132 % Pre-allocate global stiffness matrix
133 K_Global = zeros(6*(n_el + 1), 6*(n_el + 1));
134 M_Global = zeros(6*(n_el + 1), 6*(n_el + 1));
135
136 % Integrate over the length to create Element and Mass Stiffness Matrices
137 for i = 1:length(K)
138     for j = 1:length(K)
139         Kel(i,j) = int(K(i,j), 0, L/n_el);
140         Mel(i,j) = int(M(i,j), 0, L/n_el);
141     end
142 end
143
144 %% To use lumped mass matrix, uncomment out this section and redefine Mel as
145 %% the following
146 % Iz = b*h^3/12 + h*b^3/12;
147 % Mel = (rho*b*h*(L/n_el)/2).*[1 0 0 0 0 0 0 0 0 0 0 0;
148 %                               0 1 0 0 0 0 0 0 0 0 0 0;
149 %                               0 0 1 0 0 0 0 0 0 0 0 0;
150 %                               0 0 0 Iz/(b*h) 0 0 0 0 0 0 0 0;
151 %                               0 0 0 0 0 0 0 0 0 0 0 0;
152 %                               0 0 0 0 0 0 0 0 0 0 0 0;
153 %                               0 0 0 0 0 0 1 0 0 0 0 0;
154 %                               0 0 0 0 0 0 0 1 0 0 0 0;
155 %                               0 0 0 0 0 0 0 0 1 0 0 0;

```

```

156 %           0 0 0 0 0 0 0 0 0 Iz/(b*h) 0 0;
157 %           0 0 0 0 0 0 0 0 0 0 0 0;
158 %           0 0 0 0 0 0 0 0 0 0 0 0];
159
160 % Assemble global stiffness and mass matrices
161 for i = 1:n_el
162     if i == 1
163         K_Global([1:12],[1:12]) = K_Global([1:12],[1:12]) + Kel;
164         M_Global([1:12],[1:12]) = M_Global([1:12],[1:12]) + Mel;
165     else
166         K_Global([1+6*(i-1):12+6*(i-1)],[1+6*(i-1):12+6*(i-1)]) ...
167             = K_Global([1+6*(i-1):12+6*(i-1)],[1+6*(i-1):12+6*(i-1)]) + Kel;
168
169         M_Global([1+6*(i-1):12+6*(i-1)],[1+6*(i-1):12+6*(i-1)]) ...
170             = M_Global([1+6*(i-1):12+6*(i-1)],[1+6*(i-1):12+6*(i-1)]) + Mel;
171     end
172 end
173
174 % double(vpa(K_Global));
175 % double(vpa(M_Global));
176
177 end

```

## Eigenvalue problem formulation and solution for Stiffness Matrix Method code

```
1
2 % -----
3 % Eigensolution with Stiffness Method for Natural Frequency Calculation of
4 % Bending-Torsion Coupled Laminated Composite Beams
5 % -----
6 % Author: Pavel Babuska
7 % Date: Spring 2017
8 % -----
9
10 function [nf, modeShape] = eigenvalueBT(Mff, Kff)
11
12 % ----- Natural Frequency -----
13 % Form the system matrix and get the eigensolutions
14 % [V,D] = eig(Kff,Mff);
15 [V,D] = eig(Mff\Kff);
16
17 % V matrix gives eigenvectors and diagonal D matrix gives eigenvalues
18 % Sort the eigenvalues and eigenvectors
19 [D_sorted, ind] = sort(diag(D), 'ascend');
20 V_sorted = V(:, ind);
21
22 % Obtain natural frequencies and mode shapes
23 for i = 1:length(D)
24     nf(i) = sqrt(D_sorted(i))/(2*pi);
25     modeShape(:, i) = V_sorted(:, i);
26 end
27
28 end
```